CHEMICAL REVIEWS

Review

Calcium Orthophosphates: Crystallization and Dissolution

Lijun Wang, and George H. Nancollas

More About This Article

Additional resources and features associated with this article are available within the HTML version:

- Supporting Information
- Access to high resolution figures
- Links to articles and content related to this article
- Copyright permission to reproduce figures and/or text from this article

View the Full Text HTML

ACS Publications
High quality. High impact.

Calcium Orthophosphates: Crystallization and Dissolution

Lijun Wang and George H. Nancollas*

Department of Chemistry, University at Buffalo, The State University of New York, Amherst, New York 14260

Contents

1. Introduction

Calcium orthophosphates are the main mineral constituents of bones and teeth, and there is great interest in understanding the physical mechanisms that underlie their growth, dissolution, and phase stability. By definition, all calcium orthophosphates consist of three major chemical elements: calcium (oxidation state $+2$), phosphorus (oxidation state $+5$), and oxygen (oxidation state -2).[1] The orthophosphate group (PO_4^{3-}) is structurally different from meta (PO_3^-), pyro

($P_2O_7^{4-}$), and poly ($PO_3)_n^{n-}$. In this review, only calcium orthophosphates will be discussed. The chemical composition of many calcium orthophosphates includes hydrogen, either as an acidic orthophosphate anion such as HPO_4^{2-} or $H_2PO_4^-$, and/or incorporated water as in dicalcium phosphate dihydrate ($CaHPO_4 \cdot 2H_2O$).[1] Most calcium orthophosphates are sparingly soluble in water, but all dissolve in acids; the calcium to phosphate molar ratios (Ca/P) and the solubilities are important parameters to distinguish between the phases (Table 1) with crystallographic data summarized in Table 2. In general, the lower the Ca/P ratio, the more acidic and soluble the calcium phosphate phase.[2] It is now generally recognized that the crystallization of many calcium phosphates involves the formation of metastable precursor phases that subsequently dissolve as the precipitation reactions proceed. Thus, complex intermediate phases can participate in the crystallization process. Moreover, the *in vivo* presence of small peptides, proteins, and inorganic additives other than calcium and phosphate has a considerable influence on crystallization, making it difficult to predict the possible phases that may form.[3] Studies of apatite mineral formation are complicated by the possibility of forming several calcium phosphate phases. The least soluble, hydroxyapatite (HAP), is preferentially formed under neutral or basic conditions. In more acidic solutions, phases such as brushite (DCPD) and octacalcium phosphate (OCP) are often encountered. Even under ideal HAP precipitation conditions, the precipitates are generally nonstoichiometric, suggesting the formation of calcium-deficient apatites. Both DCPD and OCP have been implicated as possible precursors to the formation of apatite. This may occur by the initial precipitation of DCPD and/or OCP followed by transformation to a more apatitic phase. Although DCPD and OCP are often detected during *in vitro* crystallization, *in vivo* studies of bone formation rarely show the presence of these acidic calcium phosphate phases. In the latter case, the situation is more complicated, since a large number of ions and molecules are present that can be incorporated into the crystal lattice or adsorbed at the crystallite surfaces. In biological apatite, DCPD and OCP are usually detected only during pathological calcification, where the pH is often relatively low. In normal *in vivo* calcifications, these phases have not been found, suggesting the involvement of other precursors or the formation of an initial amorphous calcium phosphate phase (ACP) followed by transformation to apatite.

In this review, we will discuss some important parameters related to crystal nucleation and growth/dissolution including the supersaturation/undersaturation, pH, ionic strength and the ratio of calcium to phosphate activities (Table 3). We then focus on the dynamics of crystallization/dissolution in the presence of additive molecules pertinent to biogenic calcium phosphate minerals.

* To whom correspondence should be addressed. Phone: 716-645-6800 ext. 2210. Fax: 716-645-6947. E-mail: ghn@buffalo.edu.

Lijun Wang received his B.S. from China Agricultural University (Beijing) in Soil Chemistry (1990). After working as an assistant scientist at the Tibet Institute of Plateau Ecology, he went to the Condensed Matter Physics and Photochemistry Laboratory, Chemistry Department of Jilin University (Changchun, China), and focused on studies of amphiphilic oligomer template-mediated inorganic nanoparticle assembly and biomimetic crystallization using a Langmuir−Blodgett technique under the mentorship of Prof. Tiejin Li (1994−1997). In 2002, he received his Ph.D. in Plant Biomineralization (cell wall template-mediated biosilicification) from Huazhong Agricultural University under Profs. Yunhua Wang and Tiejin Li. He collaborated with Profs. Fusuo Zhang and Min Li at China Agricultural University (2002−2003) as a research scientist and with Prof. George Nancollas as a postdoctoral associate at the State University of New York (SUNY) at Buffalo (2003−2006). He is currently a Research Assistant Professor at SUNY Buffalo. His primary research interests include biomolecule control of templated nucleation and growth of inorganic crystals, and dynamics of biomineralization and biodemineralization, as well as mineralized structure−function relationships.

2. Biologically Related Calcium Phosphate Phases

2.1. Structure, Composition, and Phase Stability

2.1.1. Amorphous Calcium Phosphate (ACP)

During the synthesis of HAP crystals through the interaction of calcium and phosphate ions in neutral to basic solution, a precursor amorphous phase is formed that is structurally and chemically distinct from HAP.[7] However, calculations have shown that the phase consisted of individual or groups of HAP unit cells.[8] Chemical analysis of the precursor phase indicated this noncrystalline phase to be a hydrated calcium phosphate ($Ca_3(PO_4)_2 \cdot xH_2O$) with a Ca/P ratio 1.50,[8] consisting of roughly spherical $Ca_9(PO_4)_6$ "Posner's clusters" (PC) close-packed to form larger spherical particles with water in the interstices.[9] PCs appeared to be energetically favored in comparison to alternative candidates including $Ca_3(PO_4)_2$ and $Ca_6(PO_4)_4$ clusters.[10] The structure of PCs in isolated form is notably different from that in a HAP environment.[11] In particular, the chirality feature of PCs found in the HAP environment is suggested to disappear in an isolated form and in aqueous solution. The reconsideration of PCs as possible components in the actual structural model of ACP resulted from the cluster growth model of the HAP crystal.[12] Ab initio calculations confirmed that stable isomers exist on the $[Ca_3(PO_4)_2]_3$ potential energy surface (PES).[12,13] These isomers correspond to compact arrangements, i.e., arrangements in which the Ca and PO$_4$ are disposed closely together. Their geometries are compatible with the terms "roughly spherical" used in Posner's hypothesis. The calculations performed on the monomer and dimer PES revealed that the relative energies of the different isomers are governed by a specific bonding pattern in which

George Nancollas received his B.Sc. (Hons) and Ph.D. in Physical Chemistry at the University of Wales. As a Fellow of the University of Wales, he was a Research Associate at Manchester University, U.K. He obtained a Faculty position at the University of Glasgow, Scotland, and after 13 years was invited to a Professorship in Physical Chemistry at the University of Buffalo, the State University of New York, where he also held positions as Professor and Chairman of Biomaterials, Professor of Urology, and Professor of Chemistry in the School of Dentistry. He was made a SUNY Distinguished Professor in 1989 and was elected to the Larkin Chair of Chemistry in 1997. He has served as Provost of the Faculty of Natural Sciences and Mathematics. He was a Visiting Scientist at Brookhaven National Laboratory and at the U.K. Atomic Energy Research Establishment. He is a member of the ROCK Society and a Fellow of the Royal Society of Chemistry and the AAAS. His activities in IUPAC included President of the Analytical Division and Chairman of the Equilibrium Commission. He was recipient of the Schoellkopf Award of the ACS and the Basic Research Award from the International Association for Dental Research. One of his NIH grants, now in its 36th year, is concerned with biomineralization mechanisms.

a calcium atom interacts with two PO_4^{3-} groups, forming four CaO bonds.[12,13] The compact isomers on the trimer PES are energetically favored in comparison to monomer or dimer isomers. This is rationalized by the appearance of a specific bonding pattern for the trimer case in which a calcium forms six CaO bonds with six different PO$_4$ groups. This type of bonding in encountered in HAP.[13]

It is now generally agreed that, both *in vitro* and *in vivo*, precipitation reactions at sufficiently high supersaturation and pH result in the initial formation of an amorphous calcium phosphate with a molar calcium/phosphate ratio of about 1.18−2.50. The chemical composition of ACP is strongly dependent on the solution pH: ACP phases with Ca/P ratios in the range of 1.18:1 precipitated at pH 6.6 to 1.53:1 at pH 11.7 and even as high as 2.5:1.[4] Two amorphous calcium phosphates, ACP1 and ACP2, have been reported with the same composition, but differing in morphology and solubility.[14,15] The formation of ACP precipitate with little long-range order tends to consist of aggregates of primary nuclei (roughly spherical clusters) with composition $Ca_9(PO_4)_6$[5] dependent on the conditions of formation. It hydrolyzes almost instantaneously to more stable phases. These amorphous clusters served as seeds during HAP crystallization via a stepwise assembly process[12] and were presumed to pack randomly with respect to each other,[16] forming large 300−800 Å spheres. Recent experimental studies found that ACP has definite local atomic microcrystalline order rather than a random network structure. NMR of thoroughly dried ACP suggests that the tightly held water resides in the interstices between clusters,[17] but these are probably not of intrinsic importance in the structure of ACP. It is well-known that ACP contains 10−20% by weight of tightly bound water, which is removed by vacuum drying at elevated temperature.[9]

Table 1. Ca/P Molar Ratios, Chemical Formulas, and Solubilities^a of Some Calcium Orthophosphate Minerals[1,3,4]

Ca/P molar ratio	compound	formula	solubility 25 °C, -log(K_{sp})	solubility 37 °C, -log(K_{sp})	solubility product 37 °C
1.00	brushite (DCPD)	$CaHPO_4 \cdot 2H_2O$	6.59	6.73	1.87×10^{-7} M^2
1.00	monetite (DCPA)	$CaHPO_4$	6.90	6.04	9.2×10^{-7} M^2
1.33	octacalcium phosphate (OCP)	$Ca_8(HPO_4)_2(PO_4)_4 \cdot 5H_2O$	96.6	98.6	2.5×10^{-99} M^{16}
1.20−2.20	amorphous calcium phosphate (ACP)	$Ca_xH_y(PO_4)_z \cdot nH_2O$, $n =$ 3−4.5; 15−20% H_2O	∼	∼	
1.50	α-tricalcium phosphate (α-TCP)	α-$Ca_3(PO_4)_2$	25.5	28.5	2.8×10^{-29} M^5
1.50	β-tricalcium phosphate (β-TCP)	β-$Ca_3(PO_4)_2$	28.9	29.6	2.5×10^{-30} M^5
1.67	hydroxyapatite (HAP)	$Ca_{10}(PO_4)_6(OH)_2$	116.8	117.2	5.5×10^{-118} M^{18}
1.67	fluorapatite (FAP)	$Ca_{10}(PO_4)_6F_2$	120.0	122.3	5.0×10^{-123} M^{18}

^{a} The solubility is given as the logarithm of the ion product of the given formulas (excluding hydrate water) with concentrations in mol/L (M). (∼ Cannot be measured precisely.)

Table 2. Crystallographic Data of Calcium Orthophosphates[1,4,5]

compound	space group	unit cell parameters
DCPD	monoclinic Ia	$a = 5.812(2)$, $b = 15.180(3)$, $c = 6.239(2)$ Å, $\beta = 116.42(3)°$
DCPA	triclinic $P\bar{1}$	$a = 6.910(1)$, $b = 6.627(2)$, $c = 6.998(2)$ Å, $\alpha = 96.34(2)°$, $\beta = 103.82(2)°$, $\gamma = 88.33(2)°$
OCP	triclinic $P\bar{1}$	$a = 19.692(4)$, $b = 9.523(2)$, $c = 6.835(2)$ Å, $\alpha = 90.15(2)°$, $\beta = 92.54(2)°$, $\gamma = 108.65(1)°$
α-TCP	monoclinic $P2_1/a$	$a = 12.887(2)$, $b = 27.280(4)$, $c = 15.219(2)$ Å, $\beta = 126.20(1)°$
β-TCP	rhombohedral $R3Ch$	$a = b = 10.4183(5)$, $c = 37.3464(23)$ Å, $\gamma = 120°$
HAP	monoclinic $P2_1/b$ or hexagonal $P6_3/m$	$a = 9.84214(8)$, $b = 2a$, $c = 6.8814(7)$ Å, $\gamma = 120°$, $a = b = 9.4302(5)$, $c = 6.8911(2)$ Å, $\gamma = 120°$
FAP	hexagonal $P6_3/m$	$a = b = 9.367$, $c = 6.884$ Å, $\gamma = 120°$

Table 3. Crystal Growth Controls and Their Effect on the Bulk Solution and the Crystal Surfaces[6]

parameter	effect on bulk solution	effect on crystal surfaces
supersaturation (S)	stability of solid phases	net flux to surface; determines mode of growth (island nucleation versus incorporation at existing steps)
pH	solution speciation and subsequent supersaturation	net surface charge influencing degree of protonation
ionic strength (I)	screening length within the solution-activity coefficients	Debye length of the double layer
temperature (T)	solution speciation through temperature dependence of association constants	kinetics of adsorption, desorption, diffusion
Ca/P ratio	solution speciation	kinetics of incorporation: activation barriers differ for calcium and phosphate ions
additive concentration ([X])	may change solution speciation and subsequent supersaturation	step-pinning, blocking layers, incorporation, etc.

However, drying does not alter the calcium and phosphorus atomic arrangement. The side band intensities of dried ACP suggest that its chemical shift anisotropy is similar to or identical with that of normal ACP.[17] ACP has an apatitic short-range structure, but with a crystal size so small that it appears to be amorphous by X-ray analysis. This is supported by extended X-ray absorption fine structure (EXAFS) on biogenic and synthetic ACP samples.[18−20]

The CaP amorphous phase transforms to HAP microcrystalline in the presence of water. The lifetime of the metastable amorphous precursor in aqueous solution was reported to be a function of the presence of additive molecules and ions, pH, ionic strength, and temperature.[21] The transformation kinetics from ACP to HAP, which can be described by a "first-order" rate law, is a function only of the pH of the mediating solution at constant temperature. The solution-mediated transformation depends upon the conditions which regulate both the dissolution of ACP and the formation of the early HAP nuclei.[22] Tropp et al. used ^{31}P NMR to demonstrate that the strength of ACP side bands is due to a characteristic structural distortion of unprotonated

phosphate and not to a mixture of protonated and unprotonated phosphates,[17] suggesting that ACP could contain substantial amounts of protonated phosphate not in the form of any known phase of calcium phosphate crystals. Yin and Stott suggested that, in the transformation from ACP to HAP, ACP need only dissociate into clusters rather than undergo complete ionic solvation. The cluster with C_1 symmetry is the most stable isomer in vacuum. The interaction of Posner's cluster with sodium ions and especially with protons leads to a considerable stability increase, and surprisingly, the cluster with six protons and six OH^- recovers the C_3 symmetry and similar atomic arrangement that it has as a structural unit in the HAP crystal. This may be a key factor in the transformation from ACP to HAP crystal.[23]

In general, ACP is a highly unstable phase that hydrolyzes almost instantaneously to more stable phases. In the presence of other ions and macromolecules or under *in vivo* conditions, ACP may persist for appreciable periods[3] and retain the amorphous state under some specific experimental conditions.[24]

2.1.2. Dicalcium Phosphate Dihydrate (DCPD)

The DCPD crystal consists of chains of $CaPO_4$ arranged parallel to each other.[25] Lattice water molecules are interlayered between the calcium phosphate chains. Anhydrous calcium hydrate phosphate or monetite (DCPA) is less soluble than DCPD due to the absence of water inclusions. This phase is rarely seen *in vivo*, although Young and Brown suggest that the apparent absence of this phase may be due to difficulties of detection as a consequence of its weak X-ray diffraction pattern.[3,25] DCPD has been proposed as an intermediate in both bone mineralization and enamel dissolution.[26]

Using surface X-ray diffraction, Arsic et al. have determined the atomic structure of the {010} interface of DCPD with water.[27] Since this biomineral contains water layers as part of its crystal structure, special ordering properties at the interface are expected. This interface consists of two water bilayers with different ordering properties.[27] The first is highly ordered and can be considered as part of the brushite crystal structure. Surprisingly, the second water bilayer exhibits no in-plane order but shows only layering in the perpendicular direction. It has been proposed that the low level of water ordering at the interface is correlated with the low solubility of DCPD in water.[27] Below pH 6.5, DCPD is the predominant phase, whereas above this pH the formation of ACP and octacalcium phosphate (OCP) is more pronounced.[28] On the other hand, although DCPD and OCP form readily from solution, they are thermodynamically metastable with respect to HAP and serve as precursor phases. The order of the precipitation from a supersaturated solution is governed not only by the thermodynamic solubility product but also by kinetic factors. Thus, the solid-phase first precipitated undergoes changes in solution toward phases of higher stability.[29]

2.1.3. Tricalcium Phosphate (TCP)

Several phases having a tricalcium phosphate formula unit [TCP, $Ca_3(PO_4)_2$] are known.[30] β-TCP crystallizes in the rhombohedral space group $R3c$, and its unit cell contains 21 [$Ca_3(PO_4)_2$] formula units.[31] There are three types of crystallographically nonequivalent PO_4^{3-} groups located at general points of the crystal, each type with different intratetrahedral bond lengths and angles.[31] The existence of positional disorder of one of the PO_4^{3-} groups is related to the partial occupancy of certain cation sites, as Ca^{2+} significantly alters the tilts of the neighboring PO_4^{3-} ion.[31] The Raman spectrum of the vibrational properties of β-TCP suggests that the crystal structure disorder is related to the partial occupancy of certain cation sites, as reflected in the broad, featureless low-frequency band due to external lattice modes.[32] Both HAP and β-TCP exhibit similar Raman spectra, which are dominated by the internal modes of the PO_4^{3-} tetrahedra. However, besides the presence of peaks associated with vibrations of the OH^- group in the Raman spectrum of HAP, which are highly sensitive to sample crystallinity, other characteristic features, such as the width of the PO_4^{3-} internal bands, can be used to distinguish between HAP and β-TCP.[33] The presence of sodium in the synthesis reaction medium results in the incorporation of this ion in the β-TCP network that results in improved mechanical properties, by substitution of some calcium sites.[34] A decrease of the unit cell volume of β-TCP with increasing

sodium substitution was probed using ^{31}P and ^{23}Na MAS NMR and $^{31}P\{^{23}Na\}$ REDOR experiments.[34]

β-TCP has been identified during pathological calcification, such as dental calculus formation and in renal stones, but it has not been observed in enamel, dentin, or bone.[35] The ideal β-TCP structure contains calcium ion vacancies that are too small to accommodate a calcium ion but allow for the inclusion of magnesium ions, which thereby stabilize the structures.[31] The most common, whitlockite, formed under physiological conditions, is stabilized by magnesium ions, and is not detected physiologically unless magnesium ions are present.[3]

2.1.4. Octacalcium Phosphate (OCP)

Octacalcium phosphate (OCP) has a significant biological relevance due to its role as a possible precursor during the formation of carbonated apatite in the hard tissues of vertebrates. OCP has a remarkable structural similarity to HAP due to its layered structure involving apatitic and hydrated layers.[36−39] The triclinic structure of OCP displays remarkable similarities to the hexagonal structure of HAP because the unit cell of OCP consists of apatitic layers, and apatitic layers alternate with hydrated layers parallel to the (100) face, while the hydrated layer contains lattice water and less densely packed calcium and phosphate ions. Morphologically, OCP crystallizes as {100} blades of triclinic pinacoidal symmetry, elongated along the *a*-axis and bordered by the forms {010}, {001}, and {011}.[40,41] It is generally assumed that, in solutions, the hydrated layer of the (100) face is the layer most likely exposed to solution. The water content of OCP crystals is about 1/5 that of DCPD, and this is partly responsible for its lower solubility. The similarity in crystal structure between OCP and HAP is one reason that the epitaxial growth of these phases is often observed.[25] The hydrated layer of the OCP unit cell may form an interphase between HAP and the surrounding solution.[25] If this occurs, the epitaxial intergrowth of OCP and HAP is favored.[25] A "central OCP inclusion" (also known as a "central dark line") is seen by TEM in many biological apatites[42,43] and was explained recently by the inherent lattice mismatch between OCP and HAP.[44] A solid-state ^{31}P homonuclear double-quantum (DQ) NMR study showed that the bladelike OCP crystals will transform into hexagonal rod-shaped HAP crystals as the pH of the reaction mixture increases slowly from 4.35 to 6.69.[44] A trace amount of monetite is involved in this transformation process as an intermediate phase at pH values of about 5. Together with computer-assisted lattice matching, the DQ NMR data reveal that OCP crystals transform to HAP topotaxially, where the $[000\bar{1}]_{HAP}$ and $[2\bar{1}\bar{1}0]_{HAP}$ axes are in the same directions as the $[001]_{OCP}$ and $[010]_{OCP}$ axes, respectively.[44] Furthermore, water molecules enter the hydration layers of OCP crystals via the hydrolysis reaction $HPO_4^{2-} + OH^- = PO_4^{3-} + H_2O$, which also accounts for the deprotonation of the HPO_4^{2-} ions during the transformation.[44]

OCP is unstable relative to HAP and tends to hydrolyze according to the reaction:

$$Ca_8H_2(PO_4)_6 \cdot 5H_2O + 2Ca^{2+} \rightarrow Ca_{10}(PO_4)_6(OH)_2 + 4H^+$$

(2.1)
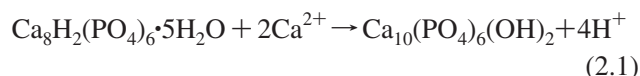
This structural relationship between OCP and HAP and its transformation from OCP to HAP provide a rational basis for understanding physiologically important phenomena such

as (i) a possible mechanism for incorporation of impurities and defects into dental enamel and (ii) a rationale as to why teeth may vary in their caries susceptibility.[45] In dental apatites, part of the lattice ions of HAP are substituted by ions such as CO_3^{2-}, F^-, Na^+, and K^+. In particular, the incorporation of carbonate has a considerable influence on the physical and physicochemical properties of the solid. K^+- and CO_3^{2-}-containing HAP formed by the hydrolysis of OCP is to be considered as interlayered mixtures of OCP and carbonated apatite. The stoichiometry of the apatite layers in the K^+- and CO_3^{2-}-containing HAP conforms to that of HAP in which the lattice ions are substituted by K^+ and CO_3^{2-}.[46] Specific infrared spectrum assignments were made for bands of the two crystallographically independent HPO_4 groups in OCP, which can be preferentially replaced by foreign anions.[47]

If OCP does act as a precursor, then interlayering would be a natural consequence and would affect the properties of enamel in many ways. For example, ingested fluoride could reduce dental caries by accelerating the hydrolysis of OCP to the less soluble HAP or FAP. The ribbonlike morphology of the initial enamel crystallites is more consistent with the morphology of OCP crystallites than it is with the hexagonal symmetry of HAP.

2.1.5. Hydroxyapatite (HAP)

Crystals of HAP may have either monoclinic or hexagonal unit cells. In the more stable, monoclinic form, rows of phosphate ions are located along the *a* axis, with calcium and hydroxide ions localized between the phosphate groups.[48] Calcium ions are placed in two triangles surrounding two hydroxide ions and in larger hexagons surrounding these calcium positions. The hydroxide ions are situated either above or below the calcium ion planes. The rows of hydroxide ions are directed, alternately, upward or downward. The hexagonal form of HAP, generally found in biological apatites, has a structure similar to the monoclinic form, but with columns of calcium and hydroxide groups located in parallel channels.[49] Ion substitution can readily occur in these channels, and this may account for the high degree of substitution found in natural apatites. In hexagonal HAP, the hydroxide ions are more disordered within each row, when compared with the monoclinic form, pointing either upward or downward in the structure. This induces strains that are compensated for by substitution or ion vacancy;[49] hexagonal HAP is therefore seldom a stoichiometric phase. As expected from the hexagonal prismatic morphology, atomic force microscopy (AFM) showed that the crystal faces appearing at the atomic level are prism (*a*-face) or basal (*c*-face).[50] A series of steps and step terraces are evident which are thought to have a dislocation origin. Their height (0.8 nm) corresponds to the minimum separation between *a*-planes.[50] The lattice constant of an apatite crystal in the *c*-axis direction is thus estimated to be 0.68 nm, and this value closely matches the lattice constant obtained by back-calculation from the CO_3 content.[50] Aging of the precipitates can lead to the incorporation of minor quantities of carbonate. Atmospheric N_2 or CO_2 can induce the incorporation of impurity ions into the apatitic structure.[51]

HAP surface layers are compositionally different from the bulk compositions. Surface layer formation is a consequence of HAP being a compound of variable composition: $Ca_{10}(PO_4)_6(OH)_2$ to $\sim Ca_9HPO_4(PO_4)_5OH$, existing over Ca/P ratios from 1.67 for stoichiometric to $\sim$1.5 for fully calcium-
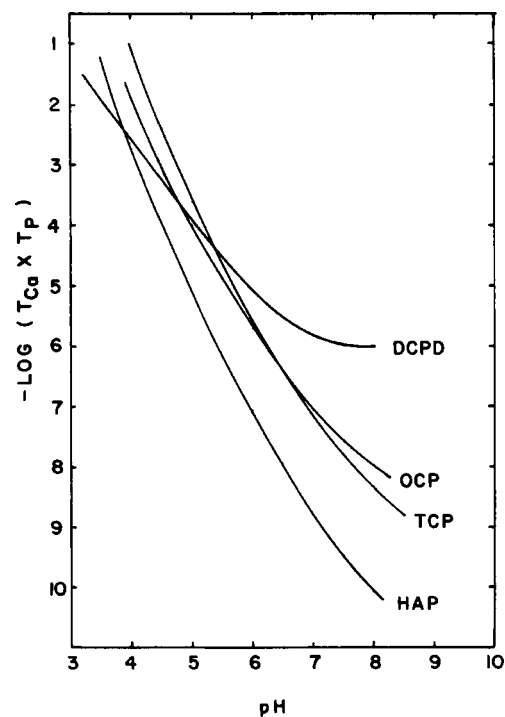

Figure 1. Solubility isotherms of calcium phosphate phases at 37 °C and $I = 0.1$ M. Reprinted with permission from ref 3. Copyright 1992 International & American Association for Dental Research.

deficient HAP. A Ca/P ratio of 1.52 was estimated from the NMR data, suggesting that the surface of nanocrystalline HAP with 1 nm surface thickness has nothing in common with the bulk composition.[52] One consequence of this compositional variability is that only one HAP composition (Ca/P ratio) dissolves congruently (the solution and solid have the same Ca/P ratio).[3] HAP compositions having Ca/P ratios different from the congruently dissolving composition will form surface layers.[3] Equilibration of stoichiometric HAP with water will result in the formation of a surface layer having a Ca/P ratio of less than 1.67. In general, for solid HAP compositions having Ca/P ratios greater than that of the congruently dissolving composition, a nonstoichiometric surface layer will form and the Ca/P ratio in solution will exceed that of the surface layer. For solid compositions having lower Ca/P ratios than the congruently dissolving composition, the opposite will be true.[53]

2.1.6. Calcium Phosphate Phase Stability

The stability of calcium phosphate (CaP) phases in contact with aqueous solutions can be understood in terms of a typical solubility phase diagram in which solubility isotherms are expressed as plots of (log $T_{ca}T_p$) as a function of pH (Figure 1). Here, T_{ca} and T_p are the total molar concentrations of calcium and phosphate, respectively. Figure 1 has been constructed on the assumption that the solution contains equal total molar concentrations of calcium and phosphate ions at an ionic strength of 0.1 M. The position of the curves and the singular points in Figure 1 will change if the ionic strength of the background electrolyte is varied. It can be seen that, at pH above 4.0, HAP is the most stable phase, followed by TCP and OCP. At pH values lower than 4.0, DCPD is more stable than HAP. The variations in solubility with pH imply that a phase exposed to acidic conditions may be covered by a surface coating consisting of a more acidic calcium phosphate phase.[3] The apparent solubility behavior
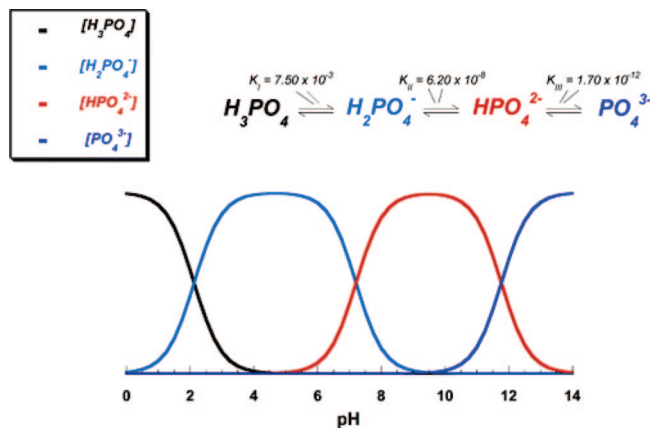
Figure 2. pH variation of ionic concentrations in triprotic equilibrium for phosphoric acid solutions. Different pH alters the relative concentrations of the four protonated forms of phosphoric acid and thus both the chemical composition and the amount of calcium phosphate crystals. Reprinted from ref 54. Copyright 2005 American Chemical Society.

will therefore be quite different from that of the original phase, and the measurement of solution concentrations might lead to unusually large estimated solubilities.[3] Moreover, in determining the likelihood of the formation of preferred crystal phases in solutions supersaturated with respect to several different phases, kinetic factors are also important. The formation of HAP is much slower than that of either OCP or DCPD, and during simultaneous phase formation, a larger portion of the kinetically favored phase may be observed, even though it has a much smaller thermodynamic driving force.[3] The balance between kinetic and thermodynamic factors is, therefore, very important in discussing the likelihood of precursor formation during calcium phosphate precipitation.[3]

The influence of pH on the formation of calcium phosphates is integrally linked to the properties of phosphate-containing solutions.[54] Due to the triprotic equilibria in these systems, variations in pH alter the relative concentrations of the four protonated forms of phosphoric acid (Figure 2) and thus both the chemical composition and the amount of the CaP that forms by direct precipitation.[54] This complex equilibrium makes the control and prediction of CaP precipitation much more difficult. During the formation of CaP/bioorganic complexes, pH plays a role in determining the properties of both the inorganic and organic phases. While its influence on the inorganic phase is largely compositional (chemical composition and mass fraction),[54] pH can affect the solubility of bioorganic species during synthesis, a property particularly important for distinguishing between systems in which calcium phosphates and bioorganics are coprecipitated[54,55] and those in which the CaP species is merely precipitated onto an insoluble bioorganic substrate.[54]

2.1.7. Phase Transformations of Calcium Phosphates

The large number of calcium phosphate phases that may form and their regions of stability, depending upon lattice ion concentrations and pH, make it possible that apatite formation *in vivo* involves more acidic calcium phosphate phases that later transform to HAP. In an attempt to understand these events *in vivo*, numerous spontaneous precipitation studies have been made *in vitro*. The stoichiometric molar ratio of calcium to phosphate calculated from

changes in concentration during precipitation from solution is frequently in the range of 1.45 ± 0.05, which is considerably lower than the value 1.67 required for the thermodynamically favored HAP. In order to reach the approximate HAP composition, extended solid/solution equilibration is required. At relatively high supersaturations, as stated above, and at pH values greater than 7, an amorphous calcium phosphate phase is formed.[56,57] It has been proposed that subsequent conversion to more stable calcium phosphate phases takes place by an autocatalytic solution-mediated crystallization process.[7,58-61] Formation of HAP without the initial precipitation of more acidic phases is achieved in solutions supersaturated only with respect to HAP (Figure 1). The transformation of the low-temperature (monoclinic, $P2_1/b$) to the high-temperature (hexagonal, $P6_3/m$) modification was investigated by means of molecular dynamics simulations. In the monoclinic phase, the orientation of the hydroxide ions is strictly ordered.[62] Above the critical temperature of about 200 °C, orientational changes of the hydroxide ions were observed.[62] In the course of each reorientation event, a hydroxide ion passes through the surrounding calcium triangle. From an Arrhenius fit, the related activation energy was calculated. In the high-temperature phase, the hydroxide ions are statistically disordered. Of the two possible concepts for the formation and structure of hexagonal HAP, the simulations clearly identified the disordering of hydroxide ion orientation that occurs in a nonconcerted manner as the more important; that is, collective reorientation of OH$^-$ ion rows was not observed.[62]

2.1.7.1. General Considerations. In spontaneous precipitation studies at high supersaturation and pH, the initial highly hydrated cryptocrystalline ACP was detected by a gradual development of opalescence in the solution following induction periods[63] that were dependent upon concentration, ionic strength, and pH.[64,65] It was shown that the induction periods for the formation of ACP and the lifetimes of this phase were increased at lower supersaturations.[21] As described in section 2.1.1, ACP2 has a more crystalline structure than ACP1.[14,65] In neutral solution, hydrolysis of ACP2 to OCP or poorly crystalline apatite was observed. In more acidic solutions, a precipitate of DCPD was formed, but without involving ACP as an initial phase. Based on the analysis of the measured precipitate induction times and the structure of the developing solid phase, OCP was also proposed by Feenstra and de Bruyn[66] as an intermediate in the conversion of ACP to apatitic calcium phosphate. Since OCP or apatite crystals were generally found in association with the ACP spherules, it is possible that ACP acts as a template for the growth of these crystal phases. Their formation, however, appears to take place by consuming ions largely supplied from the surrounding solution rather than from direct hydrolysis of the solid amorphous material. A study of ACP transformation under more alkaline conditions (pH = 10) was made by Harries et al.[19] using extended X-ray absorption fine structure (EXAFS). This method is concerned with the variation in absorption coefficient of an element on the high-energy side of the X-ray absorption edge. This is the result of the interference between a primary photoelectron wave emitted by an atom on absorption of an X-ray photon and secondary waves backscattered from neighboring atoms. This interference is dependent on the precise geometry of the atomic environment around the emitting atom, thus providing information on the coordination distances of atoms

from the excited atoms.[19] EXAFS has the advantage of defining radial distribution functions with a specific atom type defined as the origin, in terms of coordination numbers, atom types, shell radii, and Debye−Waller factors, provided that spectra of related model compounds of known crystal structure are available. Transformation experiments of ACP at pH 10 showed that the formation of poorly crystalline HAP proceeds without change in the local calcium environment, but with the development of longer range order.[19] For poorly crystalline HAP, it was necessary to invoke a regular structure out to 0.57 nm from the calcium atom, while spectra from ACP could be explained by order extending out to only about 0.31 nm. This corresponds with the first three shells, which have similar radii in ACP to those of poorly and fully crystalline HAP.[19] The lack of order beyond these three shells in ACP may be ascribed to its structure, which is characteristic of an amorphous solid, exhibiting paracrystalline disorder of the second kind.[67] The EXAFS results provide an alternative model to the suggestion, based on an analysis of X-ray (XRD) autocorrelation functions, that ACP consists of stereochemical clusters of TCP. [7,19] In the latter study, it was shown that the first two peaks in the reduced radial distribution function of ACP are similar in size and position to the corresponding peaks for HAP arising from spacings up to about 0.3 nm. This corresponds to the three shells that give rise to the features of the EXAFS spectrum, which shows no evidence for order beyond this distance from a calcium atom origin. The striking agreement between the results of these studies indicates that transformation of ACP to poorly crystalline apatite may proceed without changes in the local environment of the calcium ions and involves simply an increase in the long-range order in the structure. The influence of magnesium in the conversion of ACP to HAP and on the crystal structure and habit of HAP was interpreted in terms of its incorporation and surface adsorption.[68]

The participation of ACP as a precursor phase during apatite formation *in vivo* has been suggested.[69,70] In a comparison of XRD data for synthetic HAP and biological apatite, it was found that the peak intensity of the latter was, in general, lower, suggesting that another phase lacking X-ray fine structure was present. The conclusion that this phase must be ACP was questioned by Glimcher et al.,[71] who compared XRD spectra of stoichiometric HAP with those of nonstoichiometric and carbonate-containing samples. It was suggested that the lower peak intensities of the latter explained to some extent the missing fractions, which were attributed to ACP-like inclusions. Moreover, the small size of the apatite crystals, the presence of adsorbed impurities, and intergrown surface layers were also invoked as reasons to explain the differences between the XRD peak intensities of biological and synthetic apatites.[71] In spite of these interpretations of the spectroscopic data without invoking ACP, the similarities in short-range order around the calcium ions indicate that the possibility of ACP, as a precursor of *in vivo* formed apatite, cannot be ruled out. The rapid transformation of ACP to more crystalline calcium phosphate phases makes it unlikely that large amounts would be maintained, even in the presence of the inhibitors found in serum. However, it is important to bear in mind that the rate of this transformation of ACP is normally very rapid *in vitro*, so that this phase may be transformed before it can be detected experimentally. Consequently, the lack of observed ACP in tissue cannot be used as evidence for ruling it out

as an *in vivo* precursor. The similarities in the calcium ion environment, as revealed by EXAFS, indicate that local aggregates of ions from hydrolyzing ACP can be readily incorporated into a growing apatite lattice.[71] Kazanci et al. employed Raman analysis of the chemical conversion of ACP to HAP. The precipitation began with ACP ($\nu_1 PO_4$ around 950 cm^{-1}), and at the transition point (about 90 min at the nucleation stage), OCP at $\nu_1 PO_4$ 955 cm^{-1} was observed. After 90 min, the structure completed its maturation and the band position shifted to $\nu_1 PO_4$ 960 cm^{-1} (crystalline stage).[72] When the structure evolved from ACP to OCP, the XRD lines became visible. Prior to this region, the precursor was completely amorphous.[72] The formation of HAP from ACP was observed in situ in calcium-rich aqueous solutions with the Ca/P molar ratios 1.67, 1.83, and 2.0 by freeze-drying the precipitates withdrawn at selected time intervals during the reaction. As the amount of excess calcium ions increased in the solution, the HAP crystallization from ACP occurred more rapidly and the Ca/P molar ratio of the final precipitates increased to reach the stoichiometric value of 1.67. Acicular HAP nanocrystals grew from the interparticle phase between the spherical particles within the ACP aggregates in an initial stage of the phase transformation. This observation favors the view that an internal rearrangement process is responsible for the ACP−HAP transformation rather than a dissolution−reprecipitation process.[73]

The microstructural changes in the initial stage of conversion of α-TCP to HAP using the hydrolysis method were also investigated by TEM.[74] At first, the surface of the α-TCP was covered by an ACP layer, resulting from hydration or dissolution of α-TCP. Subsequently, the nucleation of HAP occurred on the amorphous layer, after which dendritic structures appeared on the layer. Thereafter, the dendritic structures developed into needlelike fine HAP crystals. Under physiological conditions, the picture appears to be quite different; the transformation of ACP to HAP in aqueous medium has been described as an autocatalytic conversion process,[58] and the results of a number of studies investigating the importance of solution environment[75,76] were usually interpreted as a single event, without involving discrete intermediate phases. However, Tung and Brown[57] used a titration method to study the conversion of ACP at high slurry concentrations, calculating the thermodynamic driving forces for each calcium phosphate phase to determine if the solution phase was in quasi-equilibrium with precipitated solids. A typical conversion kinetics experiment clearly indicated two processes: the first, consuming acid, and the second, consuming base, in order to maintain a constant pH of 7.4 (25 °C). In the first process, the calcium concentration increased by about 10%, reaching a maximum when the consumption of acid also reached its maximum. This implied that calcium and hydroxide ions were released simultaneously from the ACP, in accordance with the conversion of ACP to an OCP-like intermediate by reaction 2.2,[3]

$$\underset{(ACP)}{Ca_9(PO_4)_6} + 7H_2O \rightarrow \underset{(OCP)}{Ca_8H_2(PO_4)_6 \cdot 5H_2O} + Ca^{2+} + 2OH^-$$

(2.2)

Moreover, in the first acid-consuming step, the phosphate concentration decreased, ruling out the possibility that the increase in calcium and hydroxide ions was due to the simple dissolution of ACP. In the second step, requiring a consumption of base, the calcium concentration decreased and the

phosphate concentration began to increase after about 100 min, indicating that the OCP-like intermediate, as well as ACP, converted to an apatite. Following 24 h of reaction, the final product was nonstoichiometric, with Ca/P = 1.56, and showed an apatitic X-ray diffraction spectrum. Clear evidence for the formation of OCP as an intermediate in the precipitation of HAP was obtained from studies of the transition stage in the spontaneous precipitation of calcium phosphate made under pH-stat conditions by titration with base.[77] Typical plots of ΔG_{OCP} show the existence of a secondary inflection during the amorphous to crystalline transformation. Moreover, the ionic activity product of the solution phase in contact with the first-formed crystalline material was invariant and close to the solubility value for OCP, indicating the formation of this phase. The hydrolysis of the OCP to more apatitic phases may occur either by the dissolution of OCP, followed by precipitation of HAP, or by a direct solid-state transformation[25] by the hydrolysis of an OCP unit cell to a two-unit cell thick layer of HAP.[78] Either the transformation of OCP or simultaneous growth of both phases would yield an eventual apatitic phase having calcium ion deficiencies. The transformation is probably never complete, leaving unhydrolyzed regions of OCP associated with the precipitated apatite. Moreover, other ions, adsorbed at surfaces having a relatively high specific surface area, may also change the experimental Ca/P ratio. Thus, if a half-unit cell of OCP covered a stoichiometric HAP crystal, the Ca/P ratio would be about 1.64.[25] From a more detailed analysis of the experimental data,[38] a typical biological apatite is formed by the initial precipitation of OCP, which hydrolyzes to an intermediate phase termed octacalcium phosphate hydrolyzate (OCPH). This phase was thought to be made up of layers of both OCP- and HAP-like structures and included impurity ions and ion vacancies. In support of this model, TEM studies of hydrolyzed OCP crystals indicate the intergrowth of both HAP and OCP crystallites, together with a mixture of both phases,[78] which could very well be described in terms of an OCPH phase. Furthermore, crystal defects and impurity ions would be maintained in the apatitic structure, since the hydrolysis to the thermodynamically most stable phase is irreversible.[79] Daculsi et al.[80,81] compared the dissolution behavior of biological and synthetic apatites containing the central defects in the core. In all cases, dissolution occurred both at the crystal core and at the surface, with the biological apatite showing preferential core dissolution. Although this may be due to the presence of OCP in the crystal core, it could also be attributed to impurities such as carbonate in the biological apatite, with preferential dissolution of carbonated apatite.

Although many studies have favored the hypothesis that OCP is involved as an *in vivo* precursor during apatite formation, there appears to be no real evidence for the presence of this phase in nonpathological mineralization. At one stage, it was suggested that DCPD was formed in the early stages of development of embryonic bones in chicken,[82] but this finding has since been disputed.[3] There is little doubt, however, that OCP occurs as an initial phase in pathological deposits, such as calculus and kidney stones. At lower pH, DCPD may also be involved as a precursor phase, either in place of or together with OCP. Moreover, certain calcium positions in DCPD and HAP are closely aligned, opening the possibility of epitaxial intergrowth and transformation of DCPD to HAP, which has also been demonstrated using constant composition kinetics methods.[83] The results of a typical experiment demonstrated the nucleation and growth of HAP at DCPD surfaces in these solutions that were supersaturated in HAP and saturated with respect to DCPD. In situ AFM studies of dissolution kinetics of the (010) face of DCPD and the transformation of DCPD to HAP showed that the precipitation of HAP occurred after the dissolution of DCPD, and no evidence of direct structural transformation from DCPD to HAP was observed. This indicates that DCPD acts as a heterogeneous growth center for HAP without requiring any structural modification.[84]

The Ca/P ratio of precipitated calcium-deficient apatite gradually increases with the age of the precipitate, probably due to in situ transformation.[82] In general, the sequence of calcium phosphate precipitation has been observed by the relative solubility of the different solid phases at constant pH and temperature. Thus, van Kenemade and de Bruyn[85] showed that the Ostwald rule[86] was obeyed, regardless of solution conditions under which the relaxation experiments were made. Homogenous formation of HAP at low supersaturation was never observed but was always preceded by the growth of precursors. At pH 6.7, OCP was observed to form at intermediate supersaturation, largely due to the exclusion of other phases. The growth curves and relaxation times obtained under these conditions were analyzed in terms of classic nucleation and growth theories. The kinetics of formation of OCP was best described by a flashlike nucleation step in combination with surface nucleation and growth based on a mononuclear growth model. At intermediate supersaturations, the surfaces of the grown crystalline particles could be regarded as being relatively smooth, with growth proceeding by a layer mechanism, requiring the formation of a surface nucleus.[85]

In attempting to explain the preferential precipitation of one crystalline phase when compared with another, it can be argued that a lower interfacial tension or edge free energy is to be expected for a more soluble phase.[87] This could result in a lower free energy for two-dimensional nucleation, in spite of the lower supersaturation. It is quite clear that the Ostwald rule of stages, which states that the least stable, most soluble phase forms preferentially in a sequential precipitation, is likely to be obeyed for the calcium phosphates. However, in these cases, the sequence is also influenced by another important parameter, pH. It would appear, therefore, that where the driving force for HAP is relatively high, at about pH 10, the participation of more acidic phases, such as DCPD and OCP, can be ruled out. It is interesting to note that a recent constant composition study of defect apatite crystal growth also pointed to stoichiometries approaching the HAP value at high pH.[88]

2.1.7.2. Stability and Transformation of ACP in the Presence of Macromolecules. The $Ca_9(PO_4)_6$ cluster is an interesting HAP growth unit, and whether its structure is S_6 or C_3, it can be regarded as being essentially identical to the structure known as Posner's cluster.[9,11] These represent the minimum structural unit of ACP based on the results of small-angle X-ray scattering measurements. If the same structure is a constituent of HAP, it will provide important clues about the ACP−HAP phase transition mechanism by so-called solution-mediated transitions: one phase dissolves and then acts as a seed for the formation of a different phase, directing subsequent structural transformations by rearranging its internal structure. As yet, no conclusive evidence has been presented about the ACP−HAP phase transition. However, when the common aspects of growth units are considered,
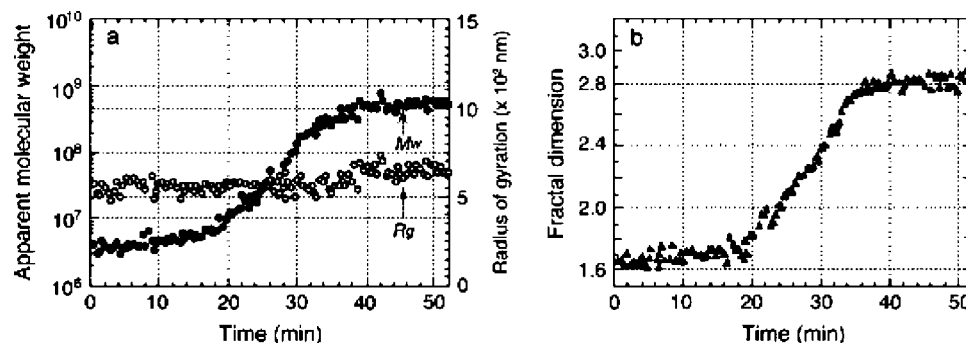
Figure 3. Time-resolved SLS measurements for the transition from ACP to HAP. (a) Change in apparent molecular weight and gyration radius of aggregates. (b) Change in fractal dimension of aggregates. The molecular weight and the fractal dimension of the aggregates increased and reached a plateau with time. However, the change in the gyration radius remained almost constant. See text for details. Reprinted with permission from ref 89. Copyright 2006 from Elsevier.

the phase transition mechanism is highly likely to involve a direct structural transformation.[89] To analyze the phase transition process, it is necessary to track with high time resolution how the molecular weight, size, and internal structure of aggregates (formed by clusters) change. The most suitable method is static light scattering (SLS).[89] By investigating how the intensity of light scattered from aggregates in a solution varies with the scattering angle (scattering vector), the mean molecular weight, M_w, and inertial radius, R_g, can be derived using eq 2.3[89]

$$Kc/\Delta R(q) = (1/M_w)(1 + R_g^2 q^2/3) + 2A_2 c \quad (2.3)$$

where $\Delta R(q)$ is the solution Rayleigh ratio, c is the concentration of the material being measured, and A_2 is the second virial material coefficient.

When the $Ca_9(PO_4)_6$ cluster size exceeds a certain threshold value, it becomes possible to define a fractal dimension, d, that represents the degree of coarseness of the internal structure of the aggregate, enabling semiquantitative verification of whether it is random or regular.[89] By combining a high-speed CCD camera with an ellipsoidal mirror that encompasses a wide range of scattering angles, Onuma et al. have developed an SLS device to simultaneously measure the scattered light over scattering angles of $10°-170°$ with a time resolution of 0.1 s.[90] Figure 3 shows the results of using this new SLS device to determine how the molecular weight and gyration radius of the aggregates change over time in a simple $CaCl_2-H_3PO_4-H_2O$ system under near-physiological pH, temperature, and concentration. XRD showed that ACP aggregates were present in the initial solution and the final product was low-crystalline HAP.[90]

The molecular weight of the aggregates abruptly increased about 20 min following the start of the measurement and reached a plateau at about 40 min. Immediately thereafter, the formation of HAP deposits became visible.[89] The change in the gyration radius of the aggregates exhibited a completely different pattern. The radius remained almost constant, increasing only slightly following the time when HAP had started to form and accumulate.[89] As shown in Figure 3b, the fractal dimension changed in concert with the molecular weight—a sharp increase at about 20 min following the start of the measurement. As mentioned above, the fractal dimension represents the degree of coarseness and regularity of the internal structure of aggregates. Considering that the initial aggregates in the solution were ACP and that the finally deposited product was HAP, since the initial aggregates of ACP had a very loose structure, they grew by assimilating growth units (calcium phosphate "Posner's"

clusters $Ca_9(PO_4)_6$,) as time progressed.[89] The internal density of the aggregates increased during this process, and the molecular weight increased while the gyration radius stayed almost the same. When the density reached a critical value, the random arrangement of growth units became disadvantageous in terms of total free energy, resulting in a sudden ordering of the structure, which was then deposited as HAP with a rapid increase in the fractal dimension, and the phase transition proceeded by a process of direct structural transformation.[89] With the increase in the number of particles in the aggregate, the internal structure changed to close packed to reduce the total free energy of the aggregate. Thus, (1) ACP directly transforms to HAP by rearrangement of each molecule, and (2) the internal bonds of ACP are partially broken (partial fusion) with the immediate formation of HAP.[88] Both cases indicate that ACP has a structural resemblance to HAP and strongly support previous conclusions that the growth unit of HAP is Posner's cluster, $Ca_9(PO_4)_6$, since this cluster is also thought to be a component of ACP.[10] This phenomenon occurred because the ACP growth units and HAP growth units were "identical". If the growth units of both materials were different, the aggregates would have dissociated and re-formed by overcoming a very large energy barrier during the phase transition process.[89]

In nucleation studies on foreign substrates, the phase transition process was influenced by the additive molecules that were present. AFM observations showed that the nucleation of HAP on collagen was greatly enhanced when phosvitin was bound to the collagen surface.[91] The nucleated crystals were rapidly and uniformly distributed on the collagen surface in the presence of phosvitin, while, in the absence of phosvitin, the crystals nucleated slowly and were observed only on specific areas.[91] Time-resolved static light scattering measurements revealed that the transformation from ACP to HAP was inhibited when phosvitin was present in the calcium phosphate solutions.[91] Soluble matrix proteins isolated from *Lingula* shells specifically promote FAP crystallization by the destabilization of ACP precursor.[92] Interestingly, the ability of *Lingula* shell macromolecules to promote FAP crystallization showed a nonlinear bell-shaped dependence on protein concentration with a maximum effect at about 0.5 μg mL^{-1}.[92] The main factor influencing this behavior was a reduction in the time associated with the ACP to FAP transformation, which also showed a nonlinear dependence on protein concentration.[92] The above results indicate that soluble macromolecules associated with the phosphatic shell of *L. anatina* can specifically promote the

in vitro crystallization of FAP. This behavior is unusual and contrary to numerous previous studies in which a wide range of low- and high-molecular-weight additives have been shown to inhibit calcium-phosphate crystallization by stabilization of a hydrated ACP precursor.[93-96] A possible mechanism for *in vitro* promotion was postulated.[92] In general, transformation of ACP involves the formation of crystalline nuclei on the surface of the precursor in association with a solution-mediated process and dissolution of the amorphous phase.[97] Protons are released in the nucleation step but consumed during ACP dissolution, and this process gives rise to a transient steady state. Strong adsorption of additives such as polyaspartate onto the surface of primary ACP nanoparticles reduces their surface charge readily in a reduction of the rate of dissolution of the amorphous phase due to colloidal aggregation.[92] Moreover, the adsorbed macromolecules block the surface nucleation sites for FAP crystallization. In contrast, addition of the *Lingula* shell proteins at low concentration appears to destabilize the ACP particles. One possibility is that the surface charge on the primary nanoparticles is increased at low levels of protein adsorption such that the extent of secondary aggregation is reduced and the rate of dissolution increased. Surface attachment of the *Lingula* proteins might also induce local ordering of FAP nuclei on the amorphous surface by facilitating structural relaxation through changes in surface dehydration and deprotonation.[92] Finally, the adsorbed macromolecules could act as templates for FAP nucleation by inducing the clustering of aqueous ions at the ACP surface. This would occur for example if the proteins were anchored at low surface coverage such that appropriate functional groups remained exposed at the solution interface rather than being buried by strong surface–macromolecule interactions associated with higher binding capacities. Indeed, it seems feasible that such conformational changes are responsible for the observed nonlinear dependence of FAP promotion on protein concentration.[92]

Both full-length recombinant DMP1 and post-translationally modified native DMP1 were able to nucleate HAP in the presence of type I collagen. However, the N-terminal domain of DMP1 (amino acid residues 1−334) inhibited HAP formation and stabilized the ACP phase that was formed. During the nucleation and growth process, the initially formed metastable ACP phase transformed into thermodynamically stable crystalline HAP in a precisely controlled manner.[98] Experiments were performed in the presence and absence of albumin (BSA) and fibrinogen (Fib) in solution as well as studying the effect of surface immobilized proteins on the biomineralization process; the results suggested that the major influence of these proteins on the CaP growth rate was their adsorption to the initially formed ACP, inhibiting the dissolution/reprecipitation of calcium phosphate. Hence, it was possible to distinguish between an amorphous layer and partly crystalline regions of different composition, possibly OCP and carbonated HAP.[99]

To facilitate understanding of the underlying mechanisms of calcium phosphate crystallization, Füredi-Milhofer et al. discussed the influence of polyelectrolytes (PEs) including polystyrene sulfonate (PSS), poly-L-lysine (PLL), and poly-L-glutamic acid (PGA) on the formation and properties of ACP and on the nucleation and growth morphology of the crystalline phase. pH vs time curves revealed three distinct precipitation events: (1) precipitation of ACP, (2) secondary precipitation of a crystalline phase upon the amorphous precursor, and (3) solution-mediated phase transformation and crystal growth. Finally, crystalline mixtures with low Ca/P molar ratios (1.39), consisting of octacalcium phosphate crystals and small amounts of apatite, were obtained.[100] The dual role of the PEs in inducing and/or inhibiting crystal nucleation in the ACP−apatite transformation system was established as follows: at low concentrations, the PE molecules adsorb reversibly on the surfaces of ACP particles in a random conformation. As a consequence, a large number of small, highly charged particles are created, which concentrate oppositely charged Ca^{2+} or HPO_4^{2-} ions and thus provide effective sites for secondary nucleation; at high concentrations, the flexible PE chains spread out into a flat position at the surface of ACP particles. This type of adsorption process is most probably irreversible and inhibits the transport of ions to the template surface, thus inhibiting secondary nucleation.[100] Moreover, Peytcheva et al. used SAXS/WAXS to study calcium phosphate crystallization in the presence of polyaspartate and found that high supersaturation leads to the immediate formation of a polymer-stabilized ACP phase with globular shape and a radius of about 100 nm.[101] Following this stage, a very slow recrystallization takes place and most of the new nuclei are bound to the previous polymer−ACP mixtures. Finally, a "hollow snowball" structure is formed, composed of single crystal platelets.[101]

Recently, Onuma et al. have studied the growth and phase transition mechanisms of HAP and its interaction with a growth factor protein in a simulated physiological environment.[89] Using AFM and real-time phase shift interferometry, they performed *in situ* observations of growth in simulated human body fluid solutions seeded with millimeter-sized HAP single crystals produced by hydrothermal synthesis, and the normal growth rate was measured.[89] The step kinetic coefficient (derived from the velocity of growth steps) and the edge free energy (calculated from the variation in the normal growth rate with the degree of supersaturation) both deviated greatly from the standard values for typical inorganic salt crystals and were found to be close to those of protein crystals.[89] This suggests that the growth units of HAP crystals are clusters rather than simple ions and that growth proceeds through the accumulation of these clusters.[89] Observations using dynamic light scattering confirmed the presence of clusters with a diameter of about 0.8−1.0 nm in simulated body fluids. *Ab initio* analysis of the cluster energy stability indicated that calcium phosphate clusters based on $Ca_3(PO_4)_2$ units achieve an energy minimum for clusters of the form $[Ca_3(PO_4)_2]_3$. These clusters have S_6 symmetry, and, when they are used to build a HAP crystal, their structure is likely to become slightly modified, resulting in the formation of C_3 structures.[89] Since these clusters would also be the building blocks of ACP, they provide vital clues to the phase transition from ACP to HAP. Using time-resolved static light scattering, the ACP−HAP phase transition process was tracked and the degree of coarseness inside a cluster aggregate changed abruptly within a specific time interval, and HAP was formed and deposited in the final stages. This suggests that an ACP aggregate transforms into HAP as its internal structure becomes regularized.[89]

2.1.8. Crystal Lattice Substitutions

The participation of acidic phases, such as DCPD and OCP, during the precipitation of apatites is often inferred

by estimations based upon molar calcium/phosphate ratios of the solid phases. However, these ratios also reflect the substitution of foreign ions in the crystal lattice, an event that has been shown to be quite common for calcium phosphates. The high degree of substitution in apatites may be due to the diffusion of ions in or out of OH^--channels within the structure, facilitating the exchange of OH^- ions for water or for other ions.[25] These channels at the crystal surfaces form parallel grooves containing adsorbed water, phosphate, OH^-, and foreign ions. Ion vacancies in Ca^{2+} or OH^- positions compensate for excess or depleted charges due to substitution. Typical ion substitutions in biological apatites are F^- for Cl^- or OH^-, carbonate for phosphate or OH^-, and Sr^{2+}, Mg^{2+}, or Na^+ for Ca^{2+}.[3,5]

The HAP surface has a remarkable avidity for fluoride, taking up this ion from aqueous solutions containing fluoride at the parts per million (50 μM) level. XPS studies have shown that the fluoride is located on the HAP surface.[102] Possible modes of incorporation of fluoride include ion-exchange, adsorption, and crystal growth of calcium fluoride, fluoroapatite ($Ca_5F(PO_4)_3$), or fluorohydroxyapatite solid solutions ($Ca_5F_x(OH)_{1-x}(PO_4)_3$). Despite extensive efforts to distinguish these possible modes of fluoride incorporation by chemical,[103] spectroscopic,[104] diffractometric,[105] and NMR techniques,[106] the hydroxyl groups or fluoride ions in the apatite structure are all stacked above each other in hexagonal channels in the c direction, where OH^- or F^- is bonded to three surrounding Ca ions which lie in the same a/b plane. Alternate rotation of the Ca positions in the a/b planes gives rise to the hexagonally shaped channels. The OH groups are stacked in a regular column within the channels, although the direction of the OH groups in the columns may differ randomly between neighboring channels.[107] The ordered array of OH^- ions in the OH^- channels needed to form the crystal structure increases the possibility of ion vacancies or incorporation of the smaller F^- ion. Moreover, vacancies of calcium and phosphate ions neighboring the OH^- channels facilitate the exchange of other ions, such as OH^- for F^-, with less lattice strain. Such substitution is facilitated by the hydrogen-bonding properties of F^-, leading to increased crystallinity.[107] Molecular dynamics simulations of the incorporation of fluoride into HAP show that they are readily incorporated from solution into the HAP surface, but although the formation of a FAP film prevents the onset of apatite dissolution, the fluoride ion does not penerate into the bulk material but remains at the surface. Substitution of OH^- groups by F^- ions from solution into the HAP surface is very exothermic, releasing 193 kJ mol^{-1} when located in the surface layer. However, incorporation into the second and third layers is progressively less exothermic, respectively releasing 164 and 68 kJ mol^{-1}, whereas subsequent segregation of fluoride further into the bulk is energetically approximately neutral at -4 kJ mol^{-1} for the process $OH_{OH}^- + F_{aq}^- \rightarrow F_{OH}^- + OH_{aq}^-$. It is thus relatively easy to replace surface hydroxyl groups by fluoride ions, but the fluoride is not expected to penetrate deeply into the apatite material itself.[108,109] These findings significantly increase our understanding of the role of fluoride in stabilizing HAP in tooth enamel and suggest that only repeated exposure to fluoride will have a lasting effect on the tooth enamel structure and its resistance to dissolution and caries formation.[108,109]

Incorporation of HPO_4^{2-} may occur by protonation of phosphate sites, while carbonate may substitute both for OH^-

and phosphate.[38] LeGeros showed that carbonate substitutes mainly for phosphate.[110] Charge balance may be achieved by sodium ion incorporation, and the substitution of carbonate usually results in poorly crystalline structures. In cases where carbonate occupies the phosphate sites, the smaller size induces strain in the lattice, leading to a unit cell contraction. An EXAFS spectroscopic study[67] reveals marked structural changes within the HAP unit cell accompanying the substitution of the phosphate ion for carbonate. The structural geometry beyond the nearest neighbor oxygen coordinations to calcium is changed in a manner consistent with an increase in structural disorder. However, the nearest neighbor coordination to calcium is not detectably influenced by the presence of carbonate. To maintain such coordination in the HAP lattice, it was concluded that the carbonate ion must be placed so that the oxygens coincide with those sites previously occupied by the phosphate oxygens. Consequently, the vacant oxygen sites are probably directed away from the calcium ions, inducing lattice strain and accounting for the observed unit cell contraction seen by X-ray diffraction. Infrared analysis[111] of *in vitro* hydrolyzed OCP shows the presence of HPO_4^{2-}, which may indicate missing or substituted calcium ions in the structure and may account for the observed increase in the a axis, when compared with stoichiometric HAP.

For the preparation of biphasic mixtures (HAP + β-TCP) of controlled ratios with the combined substitution of essential biocompatible trace elements (Na, Mg, and F), incorporated elements have played a significant role in the thermal stability of the apatites up to 1400 °C.[112] Increased calcium deficiency in the apatites has led to the formation of a higher proportion of β-TCP in the biphasic mixtures. However, minor discrepancies in the structural parameters due to the incorporated trace elements and the matching of phases of the synthesized powders with respect to the stoichiometric HAP were apparent.[112]

Computer modeling techniques have been employed to qualitatively and quantitatively investigate the dehydration of HAP to oxyapatite and the defect chemistry of calcium-deficient HAP, where a number of vacancy formation reactions are considered.[113] The dehydration of HAP into oxyhydroxyapatite is calculated to be endothermic by $E = +83.2$ kJ mol^{-1}, in agreement with experiment, where thermal treatment is necessary to drive this process. Calcium vacancies are preferentially charge-compensated by carbonate ions substituting for phosphate groups ($E = -5.3$ kJ mol^{-1}), whereas charge-compensating reactions involving PO_4 vacancies are highly endothermic (652 kJ mol^{-1}).[113] The exothermicity of the charge compensation of a Ca vacancy accompanied by a PO_4/CO_3 substitution agrees with their co-occurrence in natural bone tissue and tooth enamel. Calculations of a range of defect structures predict (i) that calcium vacancies as well as substitutional sodium and potassium ions would occur together with carbonate impurities at phosphate sites but that other charge compensations by replacement of the phosphate groups are unfavorable and (ii) that the hydroxy ions in the channel are easily replaced by carbonate groups but that the formation of water or oxygen defects in the channels is thermodynamically unfavorable. Calculated elastic constants are reported for the defect structures.[113] Furthermore, two substitutional defects are considered: the type-A defect, where the carbonate group is located in the hydroxy channel, and the type-B defect, where the carbonate group is located at the position of a

phosphate group.[113] de Leeuw et al. made a direct comparison of the energies per substitutional carbonate group; the results of the different defect simulations show that the type-A defect where two hydroxy groups are replaced by one carbonate group is energetically preferred ($\Delta H = -404$ kJ mol^{-1}), followed by the combined A–B defect, where both a phosphate and a hydroxy group are replaced by two carbonate groups ($\Delta H = -259$ kJ mol^{-1}).[113,114] The type-B defect, where a phosphate group is replaced by both a carbonate group and another hydroxy group in the same location, is energetically neutral ($\Delta H = -1$ kJ mol^{-1}). However, when the replacement of the phosphate group by a carbonate ion is charge compensated by the substitution of a sodium or potassium ion for a calcium ion, the resulting type-B defect is energetically favorable ($\Delta H_{-Na} = -71$ kJ mol^{-1}, $\Delta H_{-K} = -6$ kJ mol^{-1}) and its formation is also promoted by A-type defects present in the lattice.[114] These simulations suggest that it is energetically possible for all substitutions to occur, and they can be interpreted as ion-exchange reactions from aqueous solution. Carbonate defects are widely found in biological HAP and the simulations, showing that incorporation of carbonate from solution into the HAP lattice is thermodynamically feasible and in agreement with experiment.[114] Both types have unbalanced charges, and various forms of charge compensation are involved.[115] When calculated energies of selected stable compounds are used, the formation energies of different carbonate substitutions with accompanying charge compensation defects can be compared. The results indicate that compact complexes are energetically favored, and a B-type material with charge compensation by a calcium vacancy together with a hydrogen atom which bonds to a neighboring phosphate is the most stable of all those considered.[115] The number of HAP surface P–OH groups was at a maximum for Ca/P = 1.6 while the quantity of irreversibly adsorbed CO_2 was at a minimum at the same Ca/P. This indicates that the surface P–OH groups are not only the reversible adsorption sites for CO_2 but also interfere with the irreversible adsorption of CO_2.[116]

In contrast to the more sparingly soluble apatites, both OCP and DCPD dissolve more readily, contain water in their crystal lattices, and do not tend to incorporate impurity ions.[117] The influence of foreign ions on the rate of formation of apatite from DCPD and OCP depends, in part, on the possibility of their incorporation into the precipitating apatitic phase. In many situations, both *in vivo* and *in vitro* ions such as carbonate will catalyze the formation of carbonated apatite so rapidly that it is usually impossible to detect intermediate phases, such as DCPD and OCP, if they exist during the reaction. Thus, the overall "hydrolysis" of the acidic phases is apparently catalyzed by the presence of such ions. In contrast, some ions, present in the solution phase, are effective inhibitors of some calcium phosphate phases, leading to the kinetic stabilization of initial transient phases. Thus, the frequently observed amorphous phase, ACP, during *in vivo* mineralization may be a consequence of the presence of Mg^{2+} ions, which kinetically stabilize acidic calcium phosphate phases during *in vitro* precipitation reactions.[58] It is interesting to note that in the early fetal bones of magnesium-deficient animals, only an apatitic phase can be detected;[3] normally, the presence of this ion would stabilize ACP.[118,119]

3. Crystal Nucleation and Growth from Solutions

3.1. General Remarks

Considerable attention has been paid to surface features on crystals and equilibrium crystal shapes.[120,121] Classic crystallization theory assumes that crystals nucleate and grow from elementary species (ions, molecules) in a supersaturated solution, although phase transformations may also occur in the later stages. The association of solution species to form "growth units" is an important initial step. These may then grow in size by aggregation, with local loss of solvent, and undergo amorphous–crystalline transformations or phase transformations en route to a thermodynamically stable macrocrystal. Additionally, it is important to note that amorphous assemblies or aggregates serve as substrates to direct the growth of mineral phases.[122,123] Despite the emergence of several theories in recent decades,[124–127] much confusion still surrounds these dynamic processes. This has been due in part to the limitations of existing experimental approaches. Colloidal suspensions have been used as experimental model systems for the study of crystal nucleation and structural phase transitions,[128–130] since their crystallization phase diagrams are analogous to those of atomic and molecular systems, and solid phases can be visualized using confocal microscopy.[131] However, as the thermodynamic driving force remained undefined in almost all of these experimental systems, important factors such as critical nuclei sizes and nucleation rates are at best semiquantitative. Liu et al. recently presented quantitative measurements of the pre- and postnucleation processes of colloidal spheres using a new imaging approach under well-defined thermodynamic driving forces.[132] Moreover, computer simulations have been widely used to obtain quantitative predictions of homogeneous and hetergeneous nucleation in the absence and presence of impurities.[133–136]

One of the exciting aspects of the advent of AFM was the ability to observe directly many of the surface features and growth mechanisms predicted much earlier theoretically.[137,138] As a consequence, there is generally good overlap between experiment and theory at longer times (approaching equilibrium) and over a range of length scales. At present, both simulation and experiment have the potential to provide the deepest insight into crystal growth and nucleation. It is apparent that the simulation methods provide key information that can be used to guide and interpret crystallization experiments. However, it is imperative to address the simulation on a much smaller scale (a few thousand atoms) and at short time scales (up to a few nanoseconds) to larger length scales and longer times relevant to real crystal growth systems. Recent studies from Gale et al. have shown that it is still possible to operate kinetic Monte Carlo simulations at much longer length and time scales.[139]

There are many factors that will influence nucleation, such as the use of a foreign surface as the nucleator rather than a crystal of the same material. The increase of foreign particle size may lower $f(m,x)$ (a parameter describing the influence of foreign particles on the nucleation barrier) and promote the nucleation rate at lower supersaturations.[140,141] Small particles may also control the nucleation kinetics at higher supersaturations.[142] Cacciuto et al. have found that, to be effective crystallization promoters, seed particles need to exceed a well-defined minimum size. Just above this size, seed particles act as crystallization "catalysts"[135] while smaller seeds hardly affect the height of the nucleation

barrier; the precritical nuclei break away from the seed surface, and the critical nuclei are formed only in the bulk.[135] As each crystal nucleus is detached, the seed again becomes free to produce a new crystal. As a consequence, the number of crystallites will be much larger than the number of seeds and the final crystallites will be small.[135] This has important consequences for the size distribution of crystallites formed in heterogeneous nucleation; large, nearly flat seeds tend to produce one single crystal that grows to macroscopic size.[135,143] In addition, surface properties of flat seeds such as amphiphilicity will also affect crystal nucleation and growth. *In vivo*, an interesting result has been reported, following surgery, for the potential calcification of intraocular len (IOL) surfaces implanted in cataract patients.[144,145] A hydrophilic surface may induce the nucleation and growth of OCP crystallites under biological conditions when implanted IOL surfaces were modified with functional groups, such as carboxylate, serving as active nucleation sites.

Although the crystallization of a solid from solution appears to be simple, in spite of Ostwald's 1897 work on crystal nucleation,[86] Gibbs's thermodynamic results,[146] and the development of classical nucleation theory (CNT), this process is still not fully understood.[146] According to Ostwald's rule, normally, the first occurring phase in polymorphism, is the least stable and closest in free energy to the mother phase, followed by phases in order of increasing stability. An intriguing example of Ostwald's rule is the so-called two-step crystallization (TSC) that was originally demonstrated by ten Wolde and Frenkel in protein crystallizing systems.[147] TSC occurs widely in biocrystallizations[148] and may be a mechanism underlying most crystallization processes in atomic systems.[149,150] Thus, the occurrence of a transient amorphous precursor will modify the formation of crystalline structures. Zhang and Liu used a colloidal model system to quantitatively study the kinetics of crystallization via an amorphous precursor, the so-called multistep crystallization (MSC).[151] In MSC, amorphous dense droplets are first nucleated from the mother phase. Subsequently, a few unstable subcrystalline nuclei can be created simultaneously by fluctuation from the tiny dense droplets, which is different from previous theoretical predictions. It is necessary for these crystalline nuclei to reach a critical size $N_{crys}*$ to become stable. However, in contrast to subcrystalline nuclei, stable mature crystalline nuclei are unexpectedly created not by fluctuation but by coalescence of subcrystalline nuclei.[151] To accommodate a mature crystalline nucleus larger than the critical size $N_{crys}*$, the dense droplets have to first acquire a critical size $N*$.[151] This implies that only a fraction of amorphous dense droplets can serve as crystal nucleation precursors. As an outcome, the overall nucleation rate of the crystalline phase is, to a large extent, determined by the nucleation rate of crystals in the dense droplets, which is much lower than the previous theoretical expectation. Furthermore, it is surprising to note that MSC will promote the production of defect-free crystals.[151]

The central problem in both nucleation theory and experiment is to express the nucleation rate as a function of the controlling parameters, the most important of which is the thermodynamic driving force or the supersaturation.[141] To model the thermodynamic properties of a solution, it is first necessary to know the solubility product (K_{sp}) for all possible solid phases in a precipitation reaction at a given temperature.[141]

3.2. Crystal Nucleation

3.2.1. Solution Speciation

In order to be able to discuss the formation of calcium phosphates during a sequential nucleation reaction, the concentrations of free-ion species in the solution must be calculated. Both calcium and phosphate ions may form ion pairs, thereby decreasing the effective concentrations of the free ions. Tribasic orthophosphoric acid is quite strong with respect to the first dissociation and moderately and very weak with respect to the second and third dissociations, respectively. As a result, it is necessary to take into account not only phosphate protonation equilibria but also the formation of phosphate ion pairs with other multivalent cations, as well as the appreciable protonation of phosphate ions at precipitate surfaces.[152] The concentrations of ionic species at any time during crystallization reactions may be calculated from electroneutrality and mass balance relationships, together with the appropriate equilibrium constants, by successive approximations for the ionic strength, I.[3,30]

3.2.2. Thermodynamic Driving Forces

As noted above, interactions between ions in electrolyte solutions reduce the effective free ion concentrations from their stoichiometric values as defined by eq 3.1:[153]

$$a_i = c_i y_\pm \tag{3.1}$$

where a_i is the activity, c_i is the concentration of the ith ion, and $y_\pm$ is the mean activity coefficient, which can be calculated using an extended form of the Debye–Hückel equation such as that proposed by Davies (eq 3.2):[153]

$$\log y_\pm = -A z_i^2 \left(\frac{I^{1/2}}{1 + I^{1/2}} - 0.3I \right) \tag{3.2}$$

In eq 3.2, z_i represents the charge on the ith ion and A is a temperature-dependent constant. The ionic strength, I, usually adjusted to the physiological level for biomimetic mineralization studies, is defined as

$$I = 0.5 \sum c_i z_i^2 \tag{3.3}$$

The crystallization of sparingly soluble electrolytes (this includes most calcium phosphate biominerals) from a supersaturated solution may result from mixing cationic and anionic components, as in eq 3.4,[141,154]

$$mA^{n+} + nB^{m-} \rightarrow A_m B_n \tag{3.4}$$

where n and m are the cationic and anionic valences, respectively. The actual ion activity product (IAP) and its value at equilibrium (K_{sp}) (the solubility product for a precipitation reaction) are given by IAP $= (a_{A^{n+}})^m (a_{B^{m-}})^n$ and $K_{sp} = (a^e_{A^{n+}})^m (a^e_{B^{m-}})^n$, respectively.[141,154]

The chemical potential of species i is given by[154]

$$\mu_i = \mu_i^\circ + kT \ln a_i \tag{3.5}$$

where μ_i° is the chemical potential of species i in the standard state ($a_i = 1$). The thermodynamic driving force given by eq 3.6

$$\frac{\Delta \mu}{kT} = \ln \frac{a_i}{a_i^e} \tag{3.6}$$

and is often expressed as σ in terms of the relative supersaturation defined by[154]

$$\sigma = \frac{a_i - a_i^e}{a_i^e} = \frac{a_i}{a_i^e} - 1 \qquad (3.7)$$

Equation 3.6 can then be rewritten

$$\frac{\Delta\mu}{kT} = \ln(1 + \sigma) = \ln\frac{(a_{A^{n+}})^m (a_{B^{m-}})^n}{K_{sp}} = \ln\frac{IAP}{K_{sp}} \qquad (3.8)$$

The relative supersaturation can be expressed by

$$\sigma = \frac{IAP}{K_{sp}} - 1 = S - 1 \qquad (3.9)$$

where S is the supersaturation ratio. Thus, for HAP,

$$S = \frac{[a(Ca^{2+})]^{10}[a(PO_4^{3-})]^6[a(OH^-)]^2}{K_{sp}}$$

For $S = 1$, the mineral and solution are in equilibrium, for $S < 1$, the solution is undersaturation and the mineral will dissolve, and for $S > 1$, the solution is supersaturated and the mineral will grow. However, a commonly used definition of S is given by eq 3.10:[155]

$$S = \left(\frac{IAP}{K_{sp}}\right)^{1/\nu} \qquad (3.10)$$

where ν is the number of ions in a formula unit. The advantage of using eq 3.10 is that data for salts with different stoichiometries can be directly compared and thus the values of S would not depend on the choice of chemical formula. For example, $K_{sp} = 2.35 \times 10^{-59}$ for the half-unit cell representation, $Ca_5(PO_4)_3OH$, and $K_{sp} = 5.52 \times 10^{-118}$ for the corresponding full unit cell expression of $Ca_{10}(PO_4)_6$-$(OH)_2$. From this example, one can see that $S_{full} \approx S_{half}^2$, which points to the necessity of normalizing by the number of growth units when making comparisons between minerals with different stoichiometries.[6,141]

The extended Debye−Hückel equation has been shown to satisfactorily represent the activity coefficients of multiply charged ions up to ionic strengths of about 0.15 M. The necessity for carefully taking into account ionic strength effects and for making activity coefficient corrections becomes increasingly apparent as the value of I increases. For instance, at an ionic strength of about 0.1 M, HAP ionic products may be in error by as much as a factor of 10^6 if activity coefficients are neglected. Fortunately, it can be seen in the Debye−Hückel equation that the activity coefficients, at least in terms of this primitive model, depend only upon the ionic strength of the system, and most studies are made at constant ionic strengths close to the physiological level (0.15 M), so that the activity effects can be assumed to be constant during the precipitation reactions. Care must be exercised, however, to take into account ion-pair and complex formation of both calcium and phosphate species by foreign ions that may also be present in the solutions.[141]

3.2.3. Homogeneous Nucleation

Nucleation is the initial appearance of a new phase during a first-order phase transition, in which small nuclei formed spontaneously in a supersaturated solution overcome a nucleation barrier. However, unless their size exceeds a critical value—the so-called critical nucleus—they will redissolve rather than grow.[133,134,154] Using macroscopic argu-

ments to estimate the free energy required to form a crystallite, the CNT offers a simple thermodynamic explanation as to why small crystal nuclei are less stable (i.e., they have a higher free energy) than the supersaturated parent phase. The decrease in free energy due to the transfer of N particles from the metastable liquid to the solid state is approximated as $N\Delta\mu$, where $\Delta\mu = \mu_{solid} - \mu_{liquid}$ is the difference in chemical potential between the solid and the liquid state ($\Delta\mu < 0$).[133,134,154] The CNT estimate for the free-energy cost involved in the creation of the surface area A of the nucleus is γA, where γ is the surface free energy of the solid−liquid interface.[156] The free-energy costs are greater for small nuclei because they have a higher ratio of surface area to bulk volume, so small crystallites have to reach the "critical nucleus" to survive. According to CNT, the total Gibbs free-energy cost to form a spherical crystallite with radius r is[133,134,156]

$$\Delta G = \frac{4}{3}\pi r^3 \rho_s \Delta\mu + 4\pi r^2 \gamma \qquad (3.11)$$

where ρ_s is the number-density of the solid ($\rho_s = 1/\Omega$, where Ω is the volume per molecule). The first term on the right-hand side of eq 3.11 is a "bulk" term that expresses the fact that the solid is more stable than the supersaturated fluid. This term is negative and proportional to the volume of the crystallite. The second is a "surface" term that takes into account the free-energy cost of creating a solid−liquid interface. This term is positive and proportional to the surface area of the crystallite. The function ΔG goes through a maximum where $d\Delta G/dr = 0$ at $r_c = 2\gamma/\rho_s|\Delta\mu|$ and the height of the nucleation barrier is[133]

$$\Delta G_{crit} = \frac{16\pi\gamma^3}{3(\rho_s|\Delta\mu|)^2} \qquad (3.12)$$

The crystal-nucleation rate J per unit volume at which nuclei are formed depends exponentially on ΔG_{crit}

$$J = \kappa \exp(-\Delta G_{crit}/kT) = \kappa \exp\left[-\frac{16\pi}{3}\gamma^3/(\rho_s|\Delta\mu|)^2\right] \qquad (3.13)$$

where T is the absolute temperature, k is Boltzmann's constant, and κ is a kinetic preexponential. Equations 3.12 and 3.13 show that the height of the nucleation free-energy barrier, ΔG_{crit}, is proportional to $\gamma^3/|\Delta\mu|^2$, emphasizing how strongly the nucleation rate depends on both supersaturation and interfacial energy (γ).

Direct observation of crystal nucleation is difficult, often because once crystal nuclei are large enough to be seen they are well beyond the critical stage. Simulations provide insights into the structure, shape, and packing of critical nuclei, as illustrated by Auer and Frenkel.[133] Analysis of snapshots of a critical nucleus observed in their simulations showed that the face-centered cubic (fcc) and hexagonal close packed (hcp) stackings are equally likely.[133,141] In the early stages of nucleation, the random-hexagonal close-packed (rhcp) structure is simply more stable than fcc packing. Only later does this metastable rhcp structure transform into the stable fcc structure.[133,141] Auer and Frenkel also suggested that if the range of sizes of the suspended colloidal particles is sufficiently large, the colloidal mixture will be truly amorphous and cannot crystallize due to increase of the solid−liquid interfacial free energy at high supersaturations.[134] These simulation results provide possible clues that

the pathway to the final crystalline state of calcium phosphate will pass through all the less stable states in order of increasing stability,[30] or the resulting amorphous materials cannot transform into the crystallite phase. The first observed example of such a process in a living organism is seen in the chiton, a mollusk that has mineralized teeth that are used for scraping rocks to extract algae buried beneath the surface.[157] The outer layer of the tooth contains magnetite, a hard magnetic mineral. It forms from a disordered ferrihydrite precursor phase.[158] The inner layer of the tooth contains carbonated apatite, similar to the mineral present in bone which forms by way of an amorphous calcium phosphate precursor phase.[159] The hallmark of the biological strategy for making certain mineralized skeletal parts is that the first-formed solid deposits as disordered and often hydrated phases that, with time, transform into the stable crystalline deposit.[30,157]

CNT assumes that the (pre-) critical nuclei are effectively spherical due to surface tension and have the same structure as the stable bulk phase that is nucleating. However, Gasser et al. have observed elliptical nuclei by using confocal microscopy in which the crystallite surfaces are quite rough.[131] The surface roughness is associated with high surface free energy, which may facilitate the attachment of particles to the nucleus, thereby contributing to a more rapid nucleation.[160] The assumption of a spherical nucleus may be disputed because the critical nucleus could be anisotropic with different free energy costs associated with different faces. This would have repercussions on the growth rate, as different faces are likely to grow at different rates.[161] Yau and Vekilov reported direct observations of small (100-nm scale) "crystallites" taking part in the very first stages of crystallization of the protein apoferritin, which has a relatively slow time scale for crystallization because of its large size. Surprisingly, the critical nucleus of apoferrition resembles a raft, consisting of a nearly planar layer of crystal with a partial second layer on top.[162] The shape of the critical nucleus could have a large effect on its energy and therefore on the subsequent rate of crystal formation. One possibility is that the critical nucleus is not crystalline but rather a disordered, liquid-like aggregate of 20−50 molecules, with crystallinity appearing only at later stages in the growth process.[163]

3.2.4. Heterogeneous Nucleation

The addition of small "seed" particles to a supersaturated solution can greatly increase the rate at which crystals nucleate. This process is better understood, at least qualitatively, when the seed has the same structure as the crystal that it spawns.[86,135] More than a century ago, Ostwald explained that supercooled liquids can be made to crystallize by the introduction of a small seed crystal. However, the microscopic mechanism of seeding by a "foreign" substance is still not well understood.[86] The classical theory of nucleation provides a natural explanation as to why a seed crystal or a foreign object facilitates crystal nucleation;[156] in the absence of a seed, a rare, spontaneous fluctuation is needed to form a crystal nucleus that exceeds the critical size. However, crystallization can proceed spontaneously if we add to the metastable liquid phase a seed crystal or a foreign particle that is larger than the critical nucleus.

In homogeneous nucleation, the increase in the size of an embryo must overcome a free energy nucleation barrier before it can reach a critical radius and become a stable

growing crystal. In the presence of foreign objects (e.g., organic substrates for biomineralization processes), the nucleation barrier may be reduced to[154,164,165]

$$\Delta G = \Delta G_{\text{homo}} f(m, x) \ (0 \leq f(m, x) \leq 1) \quad (3.14)$$

where $f(m,x)$ is the interfacial correlation factor, varying from 0 to 1, describing the lowering of the nucleation barrier due to the presence of additive molecules or a suitable substrate.[165] This factor will depend upon supersaturation, the interfacial interaction parameter m, and the relative size of foreign particles x. $m = (\gamma_{\text{af}} - \gamma_{\text{ac}})/\gamma_{\text{cf}}$, where γ_{af}, γ_{ac}, and γ_{cf} are the interfacial free energies between the foreign particle (a) and fluid (f) and crystal nucleus (c) interface; γ_{cf} depends on the correlation and structural match between the nucleating phase and the substrate.[154,164] $x = R^s/r_c$ (where r_c the critical size of nuclei, $r_c = 2\Omega\gamma_{\text{cf}}/kT \ln(1 + \sigma)$, Ω is the molecular volume per growth unit, and R^s is the average radius of spherical shaped foreign particles).[154] When the interaction between the nucleating phase and the substrate is optimal, $f(m,x) \to 0$. Conversely, if the interfacial correlation is very poor, $f(m,x) \to 1$, and the additive molecule or the substrate exerts almost no influence on the nucleation barrier. It can be seen that $f(m,x)$ describing the interfacial correlation between biominerals and substrates will increase with supersaturation.[154,164,165] This implies that an increase of supersaturation will drive the substrates/biominerals from an interfacial structural matched state (a lower $f(m,x)$) to a state of higher mismatch (a higher $f(m,x)$). This phenomenon is referred to as supersaturation-driven interfacial structural mismatch.

Figure 4A and B illustrates that changes from one state to the other occur abruptly at certain supersaturations due to the anisotropy of the crystalline phase.[165] It follows that a good structural synergy between biominerals and additive molecules or substrates will promote an ordered biomineral structure and occurs only at low supersaturations.[165]

Taking into account the effect of the additive molecule or the substrate on both the nucleation barrier and the transport process, the nucleation rate is given by[154,165]

$$J = (R^s)^2 N^0 f''(m, x)[f(m, x)]^{0.5} B \exp\left[-\frac{\Delta G_{\text{homo}}}{kT} f(m, x)\right] \quad (3.15)$$

where N^0 is the density of the foreign particles or substrates and B is a kinetic constant.

The technical difficulties involved in directly evaluating crystal nucleation have led to other approaches to study initial crystallization events. One of the most common ways to characterize the kinetics of nucleation is to measure the induction period (t_s) prior to nucleation at different supersaturations. By definition,[166] the nucleation rate J can be expressed as eq 3.16,

$$J = 1/(t_s V) \quad (3.16)$$

where V is the volume of the system. Combining eqs 3.15 and 3.16 yields eq 3.17,

$$\ln t_s = \frac{\kappa f(m, x)}{[\ln(1 + \sigma)]^2} - \ln\{V(R^s)^2 N^0 f''(m, x)[f(m, x)]^{1/2} B\} \quad (3.17)$$

where $\kappa \ [=16\pi\gamma_{\text{cf}}^3\Omega^2/3(kT)^3]$ remains constant under a given set of conditions.[165] According to eq 3.16, the plot of $\ln(t_s)$ against $1/[\ln(1 + \sigma)]^2$ will give rise to a straight line whose
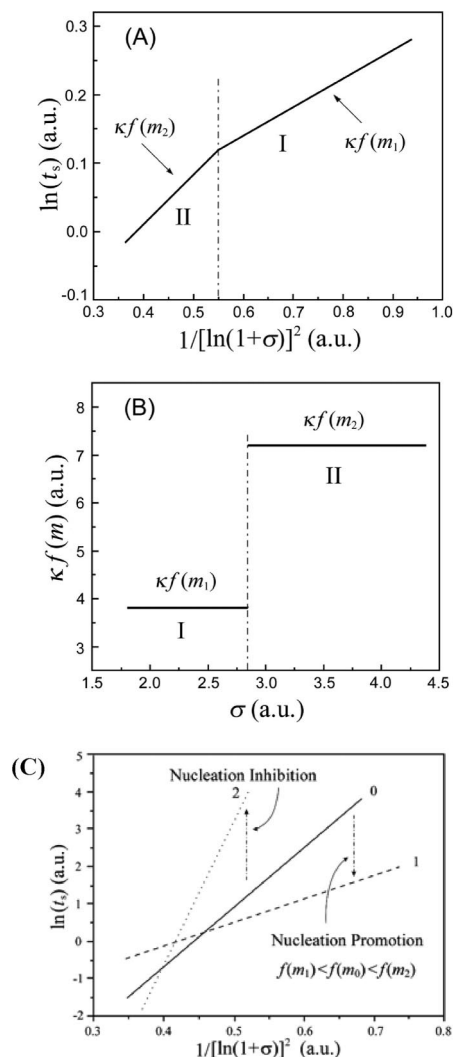
Figure 4. (A) Schematic plot of ln t_s against $1/[\ln(1 + \sigma)]^2$ for nucleation. Within the range of supersaturations, two fitted lines with different slopes intercept each other, dividing the space into two regimes. (B) Supersaturation-driven interfacial structure mismatch. With increase of supersaturation, the interfacial correlation factor $f(m)$ will increase abruptly at a certain supersaturation corresponding to the transition from an orderly and matched structure to a more mismatched state of the crystal/substrate interface. (C) Effect of additives on the interfacial correlation factor $f(m)$ and the nucleation kinetics. A promotion or inhibition effect will lower or increase, respectively, the interfacial correlation factor $f(m)$ in the $\ln(t_s) \sim 1/[\ln(1 + \sigma)]^2$ plot (a.u., arbitrary units). Reprinted with permission from refs 167 and 168. Copyright 2004 and 2005 American Society for Biochemistry and Molecular Biology.

slope is determined by κ and $f(m)$.[154,165] Obviously, for a given system (constant κ and B), the slope of the straight line will change according to $f(m,x)$. In this sense, the slope of the $\ln(t_s)$ against $1/[\ln(1 + \sigma)]^2$ plot gives the relative $f(m,x)$ for the system.[154,165] Through the analysis of $f(m,x)$ changes and correspondingly the interfacial correlations between the substrate and HAP crystalline phases in terms of the variation of the slope, collagen fibers have been found to serve as much better templates than other common foreign particles by more effectively lowering the nucleation barrier of HAP.[165] Interestingly, some biomolecules such as chondroitin sulfate may suppress the supersaturation-driven interfacial structure mismatch and promote the formation of ordered HAP crystallites.[167,168]

It follows from eq 3.17 that, for HAP nucleation, a plot of $\ln(t_s)$ against $1/[\ln(1 + \sigma)]^2$ will give rise to a straight line for a given $f(m)$. As illustrated in Figure 4C, in the case of nucleation promotion (transition from curve 0 to curve 1), the adsorption of additives on the original substrate will lead to a stronger interaction and a better structural match between the substrate and the nucleating phase.[168] This will then result in a decrease of the nucleation barrier. Since, for a given nucleation system, κ is constant, such a change can then be identified from the lowering of the slope (corresponding to $\kappa f(m)$) and the increase of the intercept of the $\ln(t_s)$ versus $1/[\ln(1 + \sigma)]^2$ plot (*cf.* eq 3.17). Conversely, if the adsorption of additives leads to repulsion and an interfacial structure mismatch between the substrate and the nucleating phase, it results in a larger nucleation barrier. The inhibition effect can be identified from the increase in the slope and the decrease of the intercept (*cf. curve 0* to *curve 2* in Figure 4C). Therefore, in the following discussion, we can apply these parameters to analyze the effect of the biomolecule on the kinetics of HAP nucleation.[168]

The constant composition (CC) method for calcium phosphate nucleation induction time measurements was modified so that supersaturation-driven structural mismatches could be detected through analysis of the control of apatite nucleation and growth by amelogenin (Amel).[169] A relatively low supersaturation was selected in order to acquire data from well-controlled nucleation and mineralization experiments in which the influence of amelogenin on nucleation could be readily detected at relatively low protein concentrations. During the induction period, the solution concentration and pH were unchanged. Once nucleation took place, the reduction in solution pH with time due to deprotonation of $H_2PO_4^-$ and HPO_4^{2-} ions associated with the formation of mineral precipitates was monitored. Amel kinetically promotes HAP nucleation (Figure 5a), and elongated ribbon-like apatite crystals (SEM) were grown in the presence of 5.0 μg mL^{-1} Amel (Figure 5b), whereas in the absence of Amel, HAP crystallites were randomly aggregated (Figure 5c).[170] After an initial induction period of about 250 min in the presence of 5.0 μg mL^{-1} Amel, the pH slowly decreased from 7.40 by approximately 0.01 units (stage I, Figure 5a). This was followed by a more rapid pH reduction to <7.35 (stage II, Figure 5a). High resolution TEM of collected precipitated solids removed after stage I indicated the first nuclei detected were uniform-sized nanorods (about 50 nm wide and about 250 nm in length) which formed in the presence of 5.0 μg mL^{-1} Amel (Figure 6a). The nanorods were aligned in parallel pairs but still separated, as shown by the arrows (Figure 6a); others were already fused into larger nanorods (Figure 6a). The less mineralized areas (white rectangle 1, Figure 6a) of the nanorods consisted of ~3 to 5 nm nanocrystallites indicated by dotted circles in Figure 6b, and the selected-area electron diffraction (SAED) pattern confirmed the diffraction pattern corresponding to the (002) plane of HAP (inset in Figure 6b). In the more mineralized areas (white rectangle 2, Figure 6a) of the nanorods, the primary nanoparticles were not randomly oriented but were ordered into aggregated (larger) clusters with parallel crystallographic axes. The measured lattice spacing of ~0.344 nm corresponds to the (002) HAP lattice plane.

The CC method allows the capture of an intermediate structure, the nanorod, following the formation of the critical nuclei at the earliest nucleation stages of calcium phosphate crystallization. The nanorod building blocks form spontane-
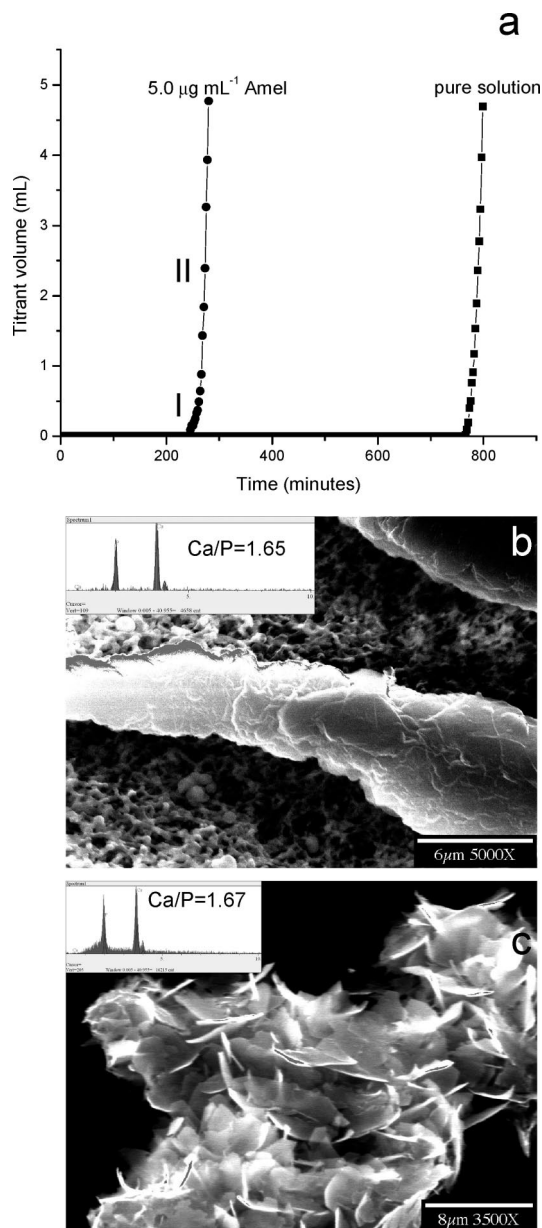
Figure 5. (a) Representative CC nucleation data plot, (b) HAP nucleated in the presence of 5.0 μg mL^{-1} Amel, and (c) HAP nucleated in the absence of Amel. Modified with permission from ref 170 Copyright 2008 American Chemical Society.

ously by synergistic interactions between flexible Amel protein assemblies and rigid calcium phosphate nanocrystallites. These intermediate structures further assemble by a self-epitaxial growth mechanism to form the final hierarchically organized microstructures that are compositionally and morphologically similar to natural enamel (Figure 6c).

Moradian-Oldak et al. have proposed that the hydrophilic C-terminal of Amel can be exposed on the surface of its nanospheres, creating structured domains with which apatite can preferentially interact.[171] This has been confirmed by solid state nuclear magnetic resonance[172] and molecular dynamics simulation[173] of Amel–HAP interactions through the hydrophilic COOH-terminal region of the Amel.[174] The notion that Amel nanospheres have their negatively charged domains exposed at their surfaces was experimentally supported by recent streaming potential measurements.[175] Beniash et al. have demonstrated that the C-terminal domain is essential for HAP organization into parallel arrays in the

presence of higher concentrations (1 mg mL^{-1}) of full-length Amel.[176] Thus, the presence of structured Amel nanospheres at lower concentrations will promote nucleation and nanoparticle assembly of apatite to induce nanorod formation. The introduction of an organic molecule that selectively adheres to a particular crystal facet can selectively slow the growth of that face relative to others, leading to the formation of rod-shaped nanocrystals.[177] Kinetic shape control through selective adhesion has been suggested by the strongest interaction of Amel with the (010) face, followed by the (001) face, and weak interaction with the (100) face of OCP crystals.[178] This may well account for the initial elongated growth of OCP crystals. Moreover, linear arrays of spherical substructures have also been detected in the enamel extracellular matrix *in vivo*.[179,180] Fusion of enamel crystallites in the early stages of mineral formation has been proposed to explain the unusually long crystals formed in mature enamel.[181] A very recent molecular dynamic simulation study showed that the carboxyl groups mainly contribute to the adsorption of leucine-rich Amel protein (LRAP) at the HAP (001) face.[173] It was suggested that two carboxyl oxygen atoms behaved like a "claw" to grasp the calcium cations occupying the outmost layer of the HAP (001) face in the *c*-axis. This Coulombic interaction dominated the adsorption of LRAP to HAP; LRAP has many such "claws" in the molecule fusing the HAP nanorods together to form larger and elongated microstructures. This simulation might provide an explanation for the elongation of growing HAP crystallites in the presence of Amel.

The relatively high supersaturations used in many calcium phosphate crystallization studies inevitably obscure the events that would take place in a slow crystallization process. High supersaturations increase the possibility of structural mismatch between mineral and organic substrate, inducing the formation of less ordered mineralized structures.[167] Recently, Tarasevich et al. also reported a promoting influence of low Amel (rM179) concentration on OCP nucleation.[182] Unfortunately, however, relatively high supersaturations were used to induce the formation of the less ordered mineralized structures. It was shown by Wang et al.[169] that, in an OCP solution at high supersaturation, the induction times in the absence and presence of Amel showed no significant change; less ordered structures were formed when compared to those at a lower supersaturation. Interestingly, at higher supersaturations the structures were more ordered in the presence than in the absence of Amel. This observation may constitute direct evidence that, at higher supersaturations, the less ordered structures that are formed can be explained by supersaturation-driven interfacial structural mismatch;[165] on the other hand, some nuclei without strong interactions with Amel may form too rapidly to have opportunities for further organization. It was therefore essential to use a relatively low supersaturation in order to acquire a slow and well-controlled nucleation by magnifying the Amel additive/template effect on the nucleation/growth at relatively low protein concentrations.

Because of differences in the solution conditions in many crystallization system studies and the physiological microenvironment in the enamel extracellular matrix, it is difficult to directly relate *in vitro* results to *in vivo* enamel formation. However, an important initial step has been achieved toward a further understanding of an isolated factor: namely, how Amel controls HAP nucleation and postnucleation growth at the earliest stages of mineralization. Hierarchical self-
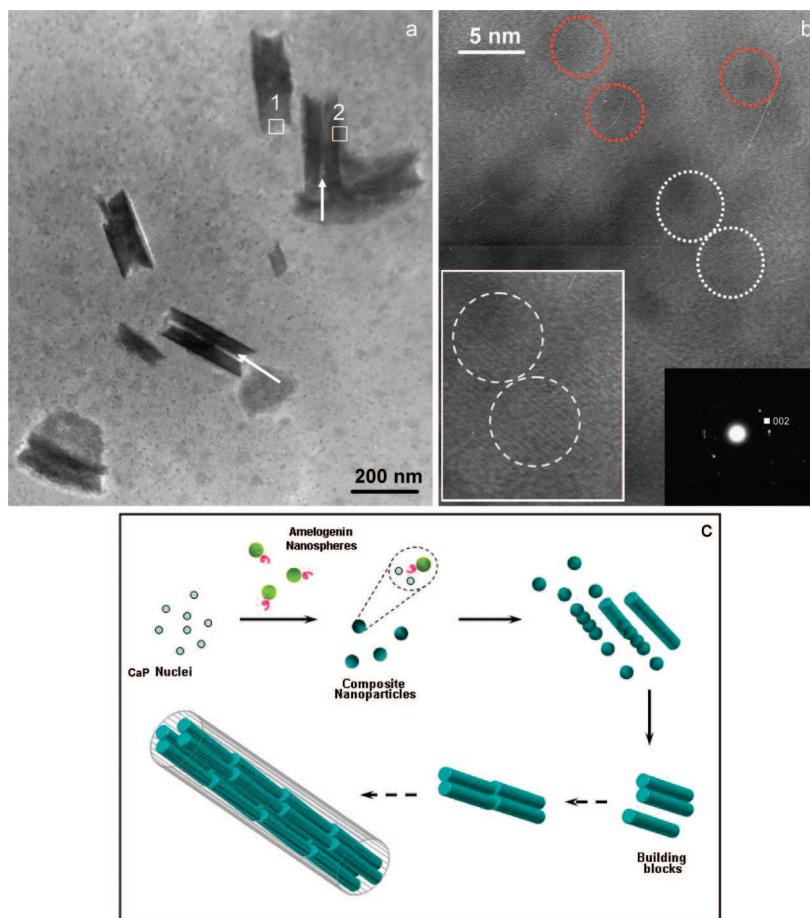
Figure 6. (a) Low magnification TEM image of nanorods at stage I in the presence of 5.0 μg mL^{-1} Amel. (b) HRTEM image taken from rectangle 1 in Figure 6a, revealing that the less mineralized area of the nanorods consists of nanocrystallites $\sim$3$-$5 nm in diameter (indicated by dotted circles). The SAED pattern corresponds to the (002) plane of HAP (right inset, Figure 6b). Some adjacent 3- to 4-nm particles aggregated, and their structures adopted parallel orientations in three dimensions, as shown by two white dotted circles and their enlargement (left inset, Figure 6b). (c) Illustration of the proposed mechanism of *in vitro* hierarchically organized microstructure formation by self-assembly of nucleated apatite nanocrystallite-Amel nanosphere mixtures based on experimental evidence (solid arrows) and theoretical analysis (dotted arrows). Reprinted with permission from ref 170. Copyright 2008 American Chemical Society.

assembly, a nucleation-growth pathway, gives rise to a remarkably high degree of cooperativity and a greater interfacial structural match between inorganic and organic nanophases, and self-epitaxial alignment between inorganic nanorods at lower driving forces. Under cooperative kinetic control, self-assembly of nucleated nanoparticles−Amel nanospheres/oligomer mixtures appears to play an explicit role in guiding nanoparticles toward nanorods. Kinetic formation of nanorods as secondary building blocks may not be arbitrary; they will most likely remain relatively stable to form larger structures by the self-epitaxial assembly mechanism during the slow crystallization process.[169,170]

3.2.4.1. Self-Epitaxial Nucleation-Mediated Assembly. Self-aligned biomineral crystallite aggregation has attracted considerable attention because of its importance in life sciences. Dental enamel consists mainly of enamel rods within which minute HAP crystallites are tightly packed and well aligned, resulting in the remarkable strength of dental enamel. As far as the formation of this crystallite aggregation is concerned, it is believed that the formation takes place via the interaction between crystalline surfaces with unlikely surface charges or sintering processes.[183,184] Nevertheless, such a process normally leads to a random aggregation with transient and weak contacts among the crystallites. Dental enamels, consisting of well aligned and intercorrelated HAP crystallite aggregates, are very unlikely to form via this

process. Based on perfect alignment and strong bonding between HAP crystallites, a self-(homo)epitaxial nucleation-mediated assembly mechanism was proposed to describe the HAP crystallite alignment in hard tissues. The self-aligned HAP aggregates are formed when new daughter HAP crystallites epitaxially grow at the actual surface of the parent HAP crystallites (Figure 7, regime B).[166,167] In this process, the parent HAP crystallites serve as substrates for the self-epitaxial nucleation and growth of the daughter HAP crystallites; therefore, the alignment and structure correlation between parent and daughter crystallites are excellent.[167] Because the self-epitaxial nucleation is actually a special type of heterogeneous nucleation, here we discuss its effect on the formation of structure patterns for HAP assembly under different conditions. As in normal heterogeneous nucleation and growth, the kinetics of self-epitaxial nucleation and growth depends on the supersaturation at the surface of the growing crystal, which increases monotonically with bulk supersaturation. At low supersaturations (Figure 7, regime A) due to a high ΔG_{mis}^*, it is difficult for self-epitaxial nucleation with a large mismatch to occur and for single crystals to grow normally (Figure 7).

3.2.4.2. Heterogeneous Nucleation on LB Films and SAMs. The well-ordered two-dimensional structure of Langmuir−Blodgett (LB) monolayers at air/water interfaces may act as nucleating templates, providing microspace for
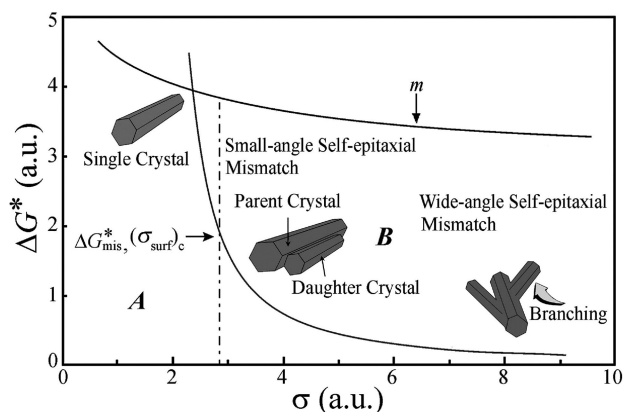
Figure 7. Illustration of self-epitaxial nucleation and growth. Regime *A*, normal single crystal growth at relatively low supersaturations. Regime *B* at low supersaturations, well aligned self-epitaxial nucleation and growth on crystal prism faces, resulting in small-angle self-epitaxial mismatch. At high supersaturations, self-epitaxial nucleation and growth results in wide-angle self-epitaxial branching (a.u. = arbitrary units). Reprinted with permission from ref 167. Copyright 2004 the American Society for Biochemistry and Molecular Biology.

biomineral growth. This method has added important insight into the relationships between the structure of a substrate and overgrowing crystals. Nucleation beneath monolayer films relies upon the degree of molecular recognition between the film and the nucleating species. This recognition may be manifested by an exact match of the headgroup of the film formation molecules to the nucleating species, usually called "template matching", whereby the film mimics a particular plane in the nucleating crystal and so leads to nucleation bounded by this plane.[185,186] Alternatively, electrostatic attraction and either geometrical matching or stereochemical complementarity may play the main role in the nucleation and crystallization of minerals in biomineralization.[187,188] Calcium phosphates have been investigated extensively using Langmuir films because they are the main inorganic components of hard tissue.[189−191] It was demonstrated that the combination of calcium ions (or phosphates) to the monolayer/subphase interface is a prerequisite for subsequent nucleation. It was found that DPCD has a biphasic structure containing both amorphous and crystalline phases and was formed through a multistage assembly process, during which an initial amorphous DPCD phase was followed by a phase transformation into a crystalline phase and then to the most stable HAP.[192] This provided new insights into the template−biomineral interaction and a mechanism for biomineralization.[192]

Established calcium carbonate studies have provided critical evidence for the molecular specificity of templated nucleation and support for the hypothesis that reduction of interfacial energy is the underlying driving force. However, they defined neither the physical mechanisms of nucleation control nor the molecular contacts that directed crystal formation. Thus, the physical processes by which nucleation control is established and the thermodynamic and kinetic parameters that define those processes remain largely unknown. Notably, the early sequence of events leading to formation of the growing nucleus, critical for defining orientation, distribution, and morphology, has received almost no attention. In nearly all of the studies of crystal nucleation on self-assembly monolayers (SAMs), the observed final orientation of the crystal phase, as well as the known structure of the mineral-free well-ordered SAM, were as-

sumed to define the structural state of the crystal nucleus and film at the time of nucleation.[193]

Although very few calcium phosphate nucleation studies using this technology have been reported, experimental evidence for the carbonate system suggests the feasibility of this approach for the phosphate system. The nucleation and growth mechanisms of calcium phosphate from supersaturated solutions on a SAM with tailored functional groups were investigated using an in situ microbalance.[193] Deposition kinetics showed a long induction period followed by a second region of extensive growth, both of which depended on the solution supersaturation. Solution studies revealed that the growth of calcium phosphate onto the surfaces following the induction period corresponded to nucleation and growth in solution. Nuclei formed in solution, started to grow, adsorbed onto the substrates, and then grew further to form apatite films composed of coalesced, oriented crystallites.[193] This solution-formed critical nucleus mechanism is in contrast to heterogeneous nucleation and reveals an important mechanism for calcium phosphate growth onto surfaces.

Recent advances in SAM technology have provided new opportunities for probing the molecular determinants of nucleation at organic matrix surfaces. Calcium phosphate nanodots, 5−10 nm in diameter on an 11-mercaptoundecanoic acid SAM in a pseudophysiological solution, were arranged two-dimensionally in a hexagonal closely packed structure in the initial stage of nucleation (≤3 h), reflecting the molecular arrangement of a thiol layer. Following this stage, the surface was covered by random nucleated calcium phosphate particles, 20−30 nm in diameter.[194] HAP crystals from developing enamel were bound most effectively by negatively charged self-assembled monolayer (COO$^-$ and SO$_3^-$) surfaces, demonstrating an important role for such substrates in AFM imaging of biological samples under aqueous fluids and suggesting that the prevalent charge on enamel crystal surfaces is positive.[195] The negative surface (OH-SAM) was favorable for HAP nucleation in a stable solution, while a selective deposition was observed on the positive surface (NH$_2$−SAM) in a metastable solution. These results suggest that the electrostatic accumulation of Ca^{2+} ions near the negative surface promoted HAP nucleation in a stable solution and the electrostatic adhesion of microparticles formed in the solution played an important role in the formation of HAP on the positive surfaces.[196]

Furthermore, a more complicated substrate, the extracellular matrix (ECM) has been shown to serve as a template for the mineralization of HAP.[197] The cellular behavior depended on the type of underlying substrate used for the HAP growth, as well as the immersion time of the samples in the simulated body fluid. Increasing the thickness of the HAP layer visibly altered the cellular response.

3.2.4.3. Two-Dimensional (2D) Nucleation Kinetics of HAP (0001) Faces. In 2D nucleation growth, the influence of impurity is more complex than that in spiral growth, since the growth rate, *R*, is related not only to the step velocity, *v*, but also to the 2D nucleation rate, *J*, as in eq 3.18[89,198]

$$R = h(v)^{2/3}(J)^{1/3} \qquad (3.18)$$

where *h* is the step height. Kanzaki et al. investigated the (0001) face of HAP, which was found to grow by multiple 2D nucleation under pseudophysiological conditions.[199] The presence of magnesium and zinc in the solutions reduced the *R* value by adsorbing at kink sites of 2D islands.[199] The sizes of 2D islands were decreased by 20−40% and 50−70%

in 0.06 mM magnesium and 0.75 μM zinc solutions, respectively. The decrease in size of 2D islands indicates a decrease in the step velocity, v ($v = C_e \varpi \beta \sigma$, where C_e is the equilibrium concentration and ω is the molecular volume of HAP), through a reduction in the step kinetic coefficient, β, caused by impurity adsorption at the kinks or steps of 2D islands.[198,199] The growth rates monotonically increased with σ in all cases. γ was calculated from these data in order to estimate the effect of impurities on J. According to the heterogeneous 2D nucleation theory by Liu et al., J is given by[89,200]

$$J = C_1 \beta (1 + \sigma) \{\ln(1 + \sigma)\}^{1/2}$$
$$\times \exp[-\pi \gamma_0^2 f/(kT)^2 \ln(1 + \sigma)]\delta \quad (3.19)$$

where C_1 is a constant, taking into account the effect of an impurity on 2D nucleation, using two factors, f and δ. The value of f is related to the ratio between the radius of an impurity particle and the critical nucleus radius and the contact angle between an impurity particle and the nucleus.[89,198,200] Using eqs 3.18 and 3.19, R beomes

$$R = C_2 \beta \sigma^{2/3} (1 + \sigma)^{1/3} \{\ln(1 + \sigma)\}^{1/6}$$
$$\times \exp\{-\pi \gamma_0^2 f/3(kT)^2 \ln(1 + \sigma)\}\delta^{1/3} \quad (3.20)$$

where C_2 is a constant. Equation 3.20 also covers homogeneous nucleation when $f = \delta = 1$. Taking logarithms of eq 3.20,[89,198]

$$\ln[R/[\sigma^{2/3}(1 + \sigma)^{1/3}\{\ln(1 + \sigma)\}^{1/6}]] = \ln C_2 + \ln \beta -$$
$$\{\pi \gamma_0^2 f/3(kT)^2\} \times 1/\ln(1 + \sigma) + \ln \delta^{1/3} \quad (3.21)$$

Equation 3.21 shows the relationship between σ and R, and from the slopes of eq 3.21, edge free energies are calculated as $\gamma_0 = 3.3kT$, $\gamma_{Mg} = 3.0kT$, and $\gamma_{Zn} = 3.4kT$.[198] If magnesium and zinc were to inhibit or promote 2D nucleation, γ would monotonically increase or decrease depending on the impurity concentration, since γ is affected by the number of impurity particles on the surface. Thus, the γ of the HAP (0001) face does not change, at least up to 0.06 mM magnesium and 0.75 μM zinc concentrations,[89,198] for which the edge free energies were constant and almost the same as the value in the absence of impurities in the supersaturation range of $\sigma = 9.8-22.0$.[198,199] This indicates that magnesium and zinc did not influence the energy barrier for 2D nucleation at least up to these concentrations, even though these impurities inhibited the growth rate of the (0001) face by adsorbing at kink sites of 2D islands. One reason why magnesium and zinc did not promote the 2D nucleation of HAP is the σ with respect to HAP; heterogeneous nucleation is likely to occur in a low σ range.[201,202] Taking into account the effect of impurities on J, the adsorption constants K of the Langmuir kink model were calculated as $K_{Mg} = (1.30 \pm 0.2) \times 10^4$ L/mol and $K_{Zn} = (1.23 \pm 0.1) \times 10^6$ L/mol at $\sigma = 22.0$ and 25 °C.[198,199]

3.3. Crystal Growth

3.3.1. Overview

Although many studies of growth mechanisms of apatite crystals have been published,[2,203-208] consistent conclusions have yet to be obtained, especially the reason for the exceedingly low growth rate, even when a large degree of supersaturation is maintained,[209] and the low crystallinity of crystals deposited under physiological conditions,[210] as well as the reasons for the frequent changes in stoichiometry.[88] Many of these open issues relating to the growth mechanisms of HAP are partly due to the lack of studies using sufficiently dense single crystals.[3,126,211] It is difficult to synthesize large single apatite crystals in which the desired crystal faces can be observed (especially crystals for which the chemical composition is well controlled), so researchers use either polycrystalline samples or sets of tiny single crystals at the macroscopic level. The growth kinetics of HAP using synthesized HAP single crystals was investigated and interpreted using a cluster growth model.[212]

3.3.2. Cluster Growth Model

In natural systems, the growth of crystals has typically been interpreted in terms of atom-by-atom addition to an inorganic or organic template or by dissolution of unstable phases (small particles or metastable polymorphs) and reprecipitation of a more stable phase. However, a growing body of experimental work indicates that additional self-assembly based coarsening mechanisms can operate in certain nanophase materials under some conditions; that is, microstructures grow via an aggregation-based pathway under natural biomineralization conditions.[213] Calcium phosphate clusters from which HAP crystals can be constituted must form in solutions as HAP grows.[12] There are calcium phosphate clusters of a certain size in the solution that constitute the apatite growth units, and this size ought to be more or less the same as the minimum step height in the crystal surface. In the AFM observation results discussed above, the minimum step height on the a-face was 0.8 nm.[89] Accordingly, the size of the clusters thought to exist in solutions is presumably also 0.8 nm. The sizes of clusters using a simple $CaCl_2-H_3PO_4-KCl-H_2O$ system in the absence of the organic buffer were investigated.[214] The observed particle size distribution was centered at about 0.8 nm, and the clusters with Ca/P ratios in the range $1-8$ remained stable for at least 100 h.[214] The tris-aminomethane buffer used in this study had no influence on the formation of the calcium phosphate clusters. Simulating the peak distribution obtained when various assumptions are made about the particle size of calcium phosphate clusters and their prevalence relative to tris-aminomethane molecules confirmed that particles ranging in size from 0.8 to 1.0 nm are likely to exist as clusters in simulated body fluid.[12]

As stated previously concerning the unit cells of apatite crystal structures projected on the ab-plane, they appear to be $Ca_9(PO_4)_6$ clusters measuring 0.815 nm along the a-axis and 0.87 nm along the c-axis.[89] This provides a very convenient explanation for the "maturation phenomenon" in which the Ca/P ratio of apatite gradually increases toward the stoichiometric ratio of 1.67 after the crystal has been deposited, and this cluster accumulation model is that the clusters stack along the c-axis.[89] The clusters exhibit a chiral relationship with C_3 symmetry.[11] It is uncertain whether they are identical to the calcium phosphate clusters in the solution, since it is extremely difficult to obtain experimental information on the cluster structures that exist in solution. Using a computational chemistry technique,[10-12] the internal structure of the cluster is kept in a compact form, and the energy per unit monomer takes a minimum value for a cluster of three units ($[Ca_3(PO_4)_2]_n$, $n = 3$).[11,89] These structures generally become more energetically stable, and in the actual crystal
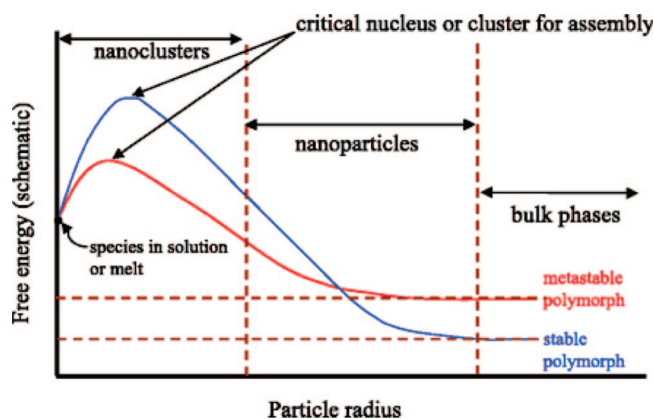
Figure 8. Schematic representation (free-energy and diameter axes do not have numerical values) of energetics of two different polymorphs as a function of particle radius. Differences in critical nucleus size and activation energy and crossover in phase stability of nanoparticles are shown. Reprinted with permission from ref 215. Copyright 2004 the National Academy of Sciences, U.S.A.

growth process, the existence of calcium phosphate clusters acting as HAP growth units seems highly likely.[89]

Nanocluster and nanoparticle precursors may play a major role in biomineralization.[215] The small differences in enthalpy and free energy among metastable nanoscale phases offer controlled thermodynamic and mechanistic pathways. Clusters and nanoparticles offer concentration and transport control of reactants.[215] Control of polymorphism, surface energy, and surface charge on nanoparticles can lead to morphological control and appropriate growth rates of biominerals. Rather than conventional nucleation and growth, assembly of nanoparticles may provide alternative mechanisms for crystal growth.[215] The Ostwald step rule, based on a thermodynamic view of nucleation and growth, is supported by the observation that more metastable phases tend to have lower surface energies.[215] The metastable phases are somehow structurally more similar to their precursors in solution and are able to nucleate more readily. If there is a general correlation between increasing metastability and decreasing surface energy, then crossovers in thermodynamic stability at the nanoscale may be a common occurrence. That is, not only will the nucleus of the metastable phase have a lower activation barrier (and smaller critical size) but also there may be a lower free energy for the growing crystal of the metastable polymorph relative to that of the phase stable in the bulk over a relatively wide size range (Figure 8). Once such metastable crystals grow, a separate set of nucleation events (and/or a dissolution–reprecipitation process) is required to form the next more stable phase.[215]

3.3.3. Constant Composition Kinetics

Constant composition (CC) is a quantitative crystal growth method where growth rates can be measured systematically as a function of the parameters controlling crystallization, especially for monitoring slow reactions at very low driving forces. As a macroscopic crystal growth technique, CC overcomes the problems associated with the changing solution composition during crystallization and the chemical potential of the solution species that are maintained constant during the reaction.[216] For example, in seeded calcium phosphate crystallization, the initial consumption of crystal lattice ions, accompanying crystal growth, is detected by a change in the hydrogen ion activity as sensed by a glass electrode. The lowering of the pH is used to trigger the

Table 4. Effective Reaction Orders, n, for Different Mechanisms[217]

n	probable mechanisms
1	volume diffusion; adsorption; volume diffusion + adsorptiion
1–2	combined mechanisms such as: adsorption + surface diffusion; volume diffusion + integration; volume diffusion + polynucleation; etc.
2	surface diffusion; integration; surface diffusion + integration
>2	polynucleation growth; polynucleation + spiral growth

simultaneous addition of two titrant solutions from stepper-motor-driven burets that serve to maintain constant pH, the concentrations of calcium and phosphate, and the ionic strength of the reaction solutions. The crystal growth rate is obtained from the titrant addition rates after normalizing for the crystal surface area. The CC method also allows the measurement of dissolution rates and induction times of homogeneous/heterogeneous nucleation.[141]

The mechanisms of crystal growth and dissolution are usually evaluated from measured reaction rates as a function of thermodynamic driving forces.[141,216] As is true for numerous crystallization reactions involving sparingly soluble calcium phosphate salts, the rate of growth, R, can be empirically written:

$$R = k\sigma^n \qquad (3.22)$$

in which k is a rate constant and n the effective reaction order. The latter are derived from logarithmic plots of rate, R, against supersaturation, σ, using eq 3.23

$$n = \frac{\partial \ln R}{\partial \ln \sigma} \qquad (3.23)$$

For the CC crystallization experiments, the molar rates of reaction may be calculated from the volume of added titrant using eq 3.24

$$R = \frac{C_{\text{eff}}}{S_A m_s} \frac{dV}{dt} \qquad (3.24)$$

where dV/dt is the titrant curve gradient, C_{eff} is the equivalent number of moles precipitated per liter of added titrant, S_A is the specific surface area of the seed crystals, and m_s is the initial seed mass. Based on the reaction order, the probable mechanisms, summarized in Table 4,[217] can be deduced, recognizing that more than one elementary process may operate simultaneously.[218] The reaction mechanisms correspond to the various crystal growth models. Thus, the Burton–Cabrera–Frank (BCF) surface diffusion and dislocation model can correspond to $n = 2$ at very low σ and $n = 1$ at large σ;[219] the BCF bulk diffusion model can be applicable for $n > 2$ at very low σ (large step spacing, y_0) and for $n = 1$ at low σ (small y_0).[219]

3.3.3.1. Kinetics of Bulk Crystallization of Calcium Phosphates. It will be apparent from the foregoing that although the likelihood of precipitation of a particular phosphate phase is ultimately determined by the thermodynamic formation driving force, kinetic factors may be considerably more important in controlling the nature of the solids formed. There is, therefore, considerable interest in characterizing the kinetics of the growth of individual calcium phosphate phases, as well as their transformation to the thermodynamically most stable apatitic phase. Such studies have usually been made by introducing seed crys-

tallites into metastable solutions and following the changes in lattice ion concentrations as a function of time.[217] However, as suggested by Figure 1, different calcium phosphate phases may participate as the concentrations relax to solubility conditions with respect to HAP. One improvement of these free-drift studies was the incorporation of a glass electrode and pH-stat so that alkali could be introduced in order to maintain constant hydrogen ion activity. However, changes in the degree of supersaturation during these experiments still resulted in the transient formation and dissolution of phases as the concentrations were reduced during the reactions.[141,217,219] Moreover, the relatively small changes in monitored calcium and phosphate concentrations during the reactions made it difficult to use these data in order to calculate the stoichiometry of the solid phases undergoing growth and/or dissolution. It is generally not possible to make quantitative physical chemical measurements on the precipitated solids, since the amount of newly formed phase is very small.[141,217]

The problems associated with these conventional free-drift studies were overcome with the development of the CC and more recently dual constant composition (DCC) methods, in which the chemical potentials of the solution species are maintained constant during the reactions.[216] Following the addition of well-characterized seed material to metastable solutions of calcium phosphate at the desired pH and supersaturation, the concentrations of lattice ions are maintained at their initial values by the simultaneous addition of titrant solutions containing calcium, phosphate, hydroxide ions, and background electrolyte from coupled burets. These additions may be controlled by suitable potentiometric probes, such as glass, calcium, and other ion specific electrodes. In this way, significant amounts of new phase can be formed, even at very low supersaturation, enabling their characterization by physical chemical methods.[2] Provided that the effective titrant concentrations are such that their stoichiometry is the same as that of the precipitating phase, the activities of all ionic species in the supersaturated solutions remain constant during the reactions. By using very dilute titrants, it is possible to obtain reliable rate data from the plots of titrant addition as a function of time, even for very slow reactions with a precision normally unattainable in conventional free-drift experiments. Another advantage of the CC method is the ability to select particular points on the solubility isotherms in Figure 2 so that the formation of DCPD and OCP phases during a sequential growth reaction can be readily probed. Thus, in the region between DCPD and OCP solubility curves, it was possible to grow, exclusively, OCP in the pH range 6.0−7.0 upon adding OCP seed crystals.[220]

Analysis of the experimental data, together with those for the formation of OCP during the transformation of DCPD,[220,221] yielded a value $n = 2$, suggesting a spiral growth mechanism at low supersaturation with respect to OCP changing to a polynucleation mechanism, with $n = 4$ at higher driving forces. In these reactions, the formation of highly crystalline OCP platelets during the reaction led to marked decreases in specific surface area, consistent with the observed morphology changes.[3,222] Calculations based on the Hartman−Perdok theory[223−225] also predicted the formation of the observed bladelike morphology of OCP. However, it should be cautioned that phase-formation conclusions based purely on morphological arguments may be entirely unjustified. Thus, Driessen et al.[226] suggested

that the boardlike form of the mineral particles in mature bone and dentin indicates that they may have originated from an OCP phase, while the flattened needle-like crystallites of mature enamel indicated DCPD as precursor phase.[3,226] Such arguments must be made with caution, since they cannot be supported by the results of *in vivo* mineral characterization. *In vitro* seeded crystal growth studies clearly demonstrate the importance of pH and σ in controlling the phase that forms.[3] Thus, in CC studies using OCP seed crystals at pH = 5 in solutions supersaturated with respect to all phases (Figure 1), DCPD was formed on the seed crystallites following an initial induction period, reflecting the nucleation of the new phase.[227] As the supersaturation increased, the induction period for DCPD formation was reduced.[3] A DCC study[228] showed that the phase transformation of DCPD to OCP occurs by dissolution of DCPD at pH 7, followed by precipitation of OCP. At higher pH (7.4−8.0), both the hydrolysis of OCP seed crystals and the formation of a more basic phase occurred.

The use of titrant solutions designed for the control of a specific phase, such as DCPD growth, resulted in a nonconstancy of composition, since the titrant stoichiometry did not match that of the precipitating phase.[3] However, the measured changes in calcium and phosphate concentration during the experiments could then be used to calculate the titrant stoichiometry needed to control the concentration and thereby determine the stoichiometry of the precipitating defect apatite.[3] This method was used to characterize the kinetics of crystallization of a series of defect apatites, $Ca_{10-x}H_x(PO_4)_6(OH)_{2-x}$ in which $0 \leq x \leq 2$.[88,229] The calcium/phosphate molar ratios of phases grown at HAP surfaces over a pH range from 6.0 to 9.0 varied from 1.49 to 1.65. Moreover, a sufficient new phase was formed to enable X-ray diffraction confirmation of the solid stoichiometry. At the physiological pH of 7.40, the constancy of calcium and phosphate concentrations during the growth experiments indicated a solid phase stoichiometry, consistent with $x = 0.57$. In all these studies, it is very important to distinguish between the formation of truly nonstoichiometric apatites and the initial ion-exchange reactions that occur upon the introduction of seed material into solutions, which, in composition, may be quite different from those in which seed crystals had been aged.[3]

3.3.3.2. Effect of Solution Stoichiometry. Zhang and Nancollas have given a detailed analysis of the effect of ionic ratio and solution stoichiometry on rates of step movement and spiral growth of an *AB* crystal following a Kossel model.[230] The theoretical analysis and related functions represent relative growth rates with respect to the maximum value at kinetic ionic ratios for integration $r_i = 1$. For a binary electrolyte *AB*, the correction function is symmetric when plotted semilogarithmically and has a maximum value of unity at $r_i = 1$. The dependence on r_i is more marked at higher *S* values. The kinetic ionic ratio, r_i, is actually the ratio of the overall forward transition rates of lattice ions. The occurrence of a maximum rate at $r_i = 1$ for a symmetrical electrolyte may be understood as follows: The advance of an *AB* step requires alternate addition of *A* and *B* ions at a kink site. Suppose that the integration rate of *A* ions is much less than that of *B* ions; then the kink waits much longer for the arrival of an *A* ion. As soon as an *A* ion integrates, the kink will immediately accommodate a *B* ion before once again awaiting an *A* ion. The kink propagation rate is thus limited to a large extent by the ions with smaller integration

rates, and a maximum rate is expected when the overall forward transition rates are the same for both ions.[230] Since the rate constants for both ions are rarely the same, the maximum growth rate may not occur when the solution stoichiometry matches that of the crystal. If the rate constants are quite different, a moderate change in the $[A]/[B]$ ratio may have a marked effect on the rate, as shown by eqs 3.25 and 3.26[230]

$$R = k_{in}\left(\frac{[B]}{[A]}\right)^{1/4}\left(S - \frac{1}{S}\right)S^{1/2}\ln S \qquad (3.25)$$

with

$$k_{in} = \frac{2a(k_A k_B^3)^{1/4}\exp(-\varepsilon/kT)}{19\gamma/kT} \qquad (3.26)$$

where k_{in} is the rate constant for spiral growth controlled by integration, $[A]$ and $[B]$ are the activities of the A and B ions, S is the saturation ratio, a is the mean ionic diameter, k_A and k_B are the forward rate constants for A and B ions, ε is the kink formation energy, and γ is the edge energy.[230] Equation 3.26 indicates that the rate is, to a greater extent, governed by the slower ion ($k_B < k_A$). However, it is interesting to note that eq 3.25 does not reduce to that of a Kossel crystal. For the growth of electrolyte crystals, the integration rates for the cation and anion may be considerably different because of the differences in dehydration frequencies. Thus, eq 3.25 is expected to be valid only in some cases.[230]

The influence of ionic ratio on the diffusion-controlled mechanism of crystal growth has also been discussed, especially in the presence of nonlattice ions at sufficiently high concentrations; the diffusion of lattice ions in solution is uncorrected.[230] A correction function is expected to apply to the growth rate controlled by adsorption and surface diffusion processes in the presence of supporting electrolytes.[231] In the following discussion, we will refer to diffusion, adsorption, and surface diffusion as "transport" processes, since they may share the same correction function ($q_t(r_t,S)$).

Nielsen derived eq 3.27 for the flux density (J) of lattice ions during diffusion-controlled growth of an AB crystal[232]

$$J = \frac{D_A[A] + D_B[B] - [(D_A[A] - D_B[B])^2 + 4D_A D_B K_{sp}]^{1/2}}{2\delta}$$
$$(3.27)$$

where D_A and D_B are the diffusion coneefficients of A and B ions, respectively, and δ is the diffusion layer thickness. Using the following definition of the kinetic ionic ratio,

$$r_t = \frac{D_A[A]}{D_B[B]} \qquad (3.28)$$

eq 3.27 may be written as

$$J = q_t(r_t, S)\frac{(D_A D_B)^{1/2}K_{sp}^{1/2}(S - 1)}{\delta} \qquad (3.29)$$

For the correction function for transport processes at different supersaturations, a maximum value also occurs at a kinetic ionic ratio for transport $r_t = 1$, and the rate decreases as r_t deviates from the stoichiometric value. As in the case of integration-controlled growth, the kinetic ionic ratio has a more pronounced effect on the rate at higher S values. The growth rate controlled by diffusion is more sensitive to changes in the kinetic ionic ratio than for an integration

controlled process. For a transport-controlled process, the supersaturation is far more than $S \geq 1$, and the correction function for a transport-controlled crystal growth becomes[230]

$$q_t(r_t, S) = r_t^{-1/2}(1 + S^{-1})(3.30) \qquad (3.30)$$

which in combination with eq 3.29 gives

$$J = \frac{D_B([B] - [B]_S)}{\delta} \qquad (3.31)$$

where $[B]_S$ is the concentration of B ions at the interface. Equation 3.31 is the same as that for a monocomponent crystal with the rate limited by the ion having a lower concentration and diffusion coefficient. This contrasts the results for an integration-controlled process where the rate constants for both ions are always present in the rate equations (see eqs 3.25 and 3.26).[230]

For *in vitro* and *in vivo* crystallization and dissolution of calcium phosphates from solutions, the ratios of the activities of the calcium and phosphate ions rarely correspond to the mineral stoichiometry. Even when the total concentrations of lattice ions are stoichiometric, the ionic activity ratio may differ considerably from this value due to the formation of ion pairs and complexes. Although some investigations have shown the marked effect of ionic ratio on growth and dissolution rates, little effort was made to explain the effect theoretically, especially for surface-controlled mechanisms.[230,233,234] Crystal growth theories developed for simple cubic lattices with only one type of growth unit (e.g., AB, a Kossel crystal) have usually been used to analyze growth and dissolution kinetics. However, theories developed for a Kossel crystal may be applicable to electrolyte crystal growth only under restricted conditions. Thus, in the absence of any indifferent ions, the lattice ions may be considered to form AB kinetic entities for volume diffusion control processes as the cations and anions diffuse at the same speed under the constraint of electroneutrality. However, the presence of indifferent ions disturbs the electrical correlation between positive and negative lattice ions during diffusion. The movement of the cations and anions becomes independent, and it is reasonable to consider them as separate growth entities. From the structure of AB steps studied under nonequilibrum conditions, the rate of step movement for different solution stoichiometries was determined.[230] For both growth and dissolution processes, it was shown that the rates cannot be defined solely in terms of the ionic activity products but also depend upon the activity ratios and the relative integration frequencies of the lattice ions. At a given thermodynamic driving force, a maximum rate occurs when this kinetic ionic ratio is unity and this may not correspond to the stoichiometric ratio of the forming crystals, indicating a direct relationship between the composition of the adsorbed surface layer and the resultant growth kinetics. The kinetics of calcium phosphate crystallizing systems appears to involve a solution dependent adsorbed layer, the composition of which is dependent upon the Ca/P in solution. The kinetics of dissolution of OCP at constant relative saturation again showed a marked dependence of dissolution rate on the Ca/P molar ratio.[235] The relationship between surface characteristics and dissolution rates was discussed in terms of the density of kinks and the kinetic Ca/P ionic ratio in the solutions.[235] Since FAP is an important phase at tooth enamel surfaces, the kinetics of growth was investigated on FAP seed crystals using CC in supersaturated solutions containing both stoichiometic and nonstoichiometric crystal lattice ion

molar ratios.[236] The results confirmed that the rate of reaction was surface controlled, probably through diffusion of depositing ions to active growth sites (kinks on steps), with surface diffusion being the predominant rate controlling process.[236] Experiments in supersaturated solutions containing nonstoichiometric lattice ion concentrations showed marked changes even at the same thermodynamic supersaturation.[236] The results again suggest the importance of involving a parameter such as the kinetic ionic ratio in addition to the thermodynamic driving force for the development of crystal growth models.[230]

Chernov et al. measured rates of elementary growth step propagation on CaOx and MgOx crystal faces by AFM and found a dependence of the step rate on the stoichiometric ratio $r = $ [cation]/[anion] in solution in the range $5 \times 10^{-2} < r < 20$ for CaOx and $0.2 < r < 5$ for MgOx.[237] The dependence was nearly symmetrical with respect to the replacement r by $1/r$ and vice versa; that is, $v(r) \cong v(1/r)$, with a clear maximum in stoichiometric solutions, $r = 1$.[237] $v = v(r^{1/2} + r^{-1/2})$ was in approximate agreement with the kink growth rate theory for binary and other non-Kossel crystals,[230,238] on the assumption that the cation and anion attachment frequencies were proportional to the concentrations of these species only and that the proportionality coefficient, the frequency factor, was independent of ion type.[237]

3.3.3.3. Interfacial Energies. The formation of calcium phosphates and other biominerals in supersaturated solution must be mediated not only by the biomacromolecules in solution and the organic matrix but also by factors which control the formation of nuclei of critical dimensions and their subsequent growth into macroscopic crystals. For example, the mineralization of collagen-containing matrices may occur by an interaction between the crystal lattice ions in the extracellular fluid and the organic components of the matrix such as the collagen fibers.[141] Traditionally, focus has been aimed primarily on the composition, structure, and morphology of the matrix while chemists have been mainly concerned with the parameters discussed in the foregoing sections such as solution composition, ionic strength, ionic activity coefficient, association constants, pH, and temperature. However, interfacial energy has hitherto usually been ignored in discussions of such induced/controlled crystallization of mineral phases and the connections between chemical processes and biological events. For most solid−liquid systems, the magnitude of the surface free energy is very difficult to predict accurately and the majority of experimental studies have been based on measurements of homogeneous nucleation, where the results often differ widely.[239] Thus, the surface free energy of HAP derived from classical heterogeneous nucleation theory ranges from 100 to 331 mJ m^{-2}, based on the rate or induction time for HAP crystal nucleation/growth in the presence of various macromolecular additives.[240,241] These impossibly high estimates promoted the need for direct measurements of contact angles at powdered calcium phosphate and dentin surfaces. Interfacial energies were obtained by a thin-layer wicking method,[242] based on the Washburn equation (eq 3.32),[243] relating contact angles of the liquid formed on the solid surfaces to the rate of penetration of liquids through the powdered substrate[244]

$$h^2 = \frac{tR\gamma_L \cos\theta}{2\eta} \qquad (3.32)$$

In eq 3.32, R is the effective interstitial pore radius, γ_L, the surface tension, θ, the contact angle of the liquid on the solid, η, the viscosity of the liquid, and h, the distance moved by the liquid column in a given time t. For the determination of contact angles formed between a liquid and finely divided powdered particles, for which direct contact angle measurements cannot be performed, a thin layer wicking capillary rise procedure through a packed column of the powder was used to calculate the contact angle.[245,246] Calculations of the interfacial energy terms from the measured contact angles were based on Young's equation adapted for polar systems,[219,247,248] yielding values for the apolar, Lifshitz−van der Waals component of the surface energy and the Lewis acid/base surface energy parameters.

$$\gamma_L(1 + \cos\theta) = 2\left(\sqrt{\gamma_S^{LW}\gamma_L^{LW}} + \sqrt{\gamma_S^+\gamma_L^-} + \sqrt{\gamma_S^-\gamma_L^+}\right) \qquad (3.33)$$

where γ_S^{LW} is the Lifshitz−van der Waals (LW) component of the surface energy of the solid and γ^+ and γ^- are the Lewis acid and base surface energy parameters, respectively. Interfacial tensions in mJ m^{-2} calculated from thin layer wicking (TLW) contact angles were as follows: DCPD, −4.2; OCP, 4.3; HAP, 10.0; FAP, 18.5; human dentin, 4.5; and human enamel, 8.8.[219] The values compared well with the data calculated from dissolution kinetics experiments invoking different reaction mechanisms. Agreement between the directly measured interfacial energies and those calculated from the kinetics experiments provided valuable corroborative information about individual growth and dissolution mechanisms.[249,250] The much smaller interfacial tensions of OCP and DCPD in water as compared with the values for HAP and FAP strongly support the suggestion that the former phases are precursors in HAP and FAP biomineralization.[3,30] Another important factor to be taken into account in the biomineralization of calcium phosphates is that of aggregation and colloid stabilities of suspensions of these phases. The relative stabilities of OCP, DCPD, and HAP dispersions may be understood in terms of the Derjaguin−Landau−Verwey−Overbeek (DLVO, electrical double-layer repulsion and van der Waals attraction) theory.[246,248] In order to understand the stability of colloid suspensions of these phases, the energy due to overlap of electrical double layers (usually repulsive) and the van der Waals energy (usually attractive) were calculated in terms of interparticle distance. For OCP and HAP, the energy of the interparticle interaction was negative while the DCPD value was positive at all separations. This explains why OCP and HAP suspensions tend to flocculate rapidly while DCPD, due to repulsive Lewis acid/base forces, remains dispersed.[246,248] The critical parameter accounting for this difference in behavior was the Lewis base surface tension parameter, which was much greater for DCPD than for OCP and HAP, indicating a hydrophilic DCPD surface whereas OCP and HAP are more hydrophobic.[251] The hydrophilicity may have resulted from the crystal structure of DCPD, which consists of chains of CaPO$_4$ arranged parallel to each other interlayered with lattice water molecules.[25] The negative interfacial energy against water for DCPD is normally associated with thermodynamically unstable interfaces.[245]

3.3.3.4. Influence of Seed Crystal Surfaces. The induced crystallization of one phase by the surface of another is a

common event in the mineralization of bone and dental hard tissues. As discussed above, the calculated low interfacial energy between OCP and HAP provides strong support for the suggestion that OCP is an early forming phase in HAP crystallization.[252] The kinetics of growth of crystals induced by HAP seed crystals was investigated in supersaturated solutions of FAP and of FAP seed crystals in supersaturated solutions of HAP.[253] In supersaturated solutions of FAP, this phase was nucleated at added HAP surfaces and underwent growth at a rate more than three times greater than that of FAP seed crystal of equivalent surface area. TEM and diffraction patterns clearly confirmed a true epitaxy with the new needle-like Hap phase originating at the FAP surfaces with the (002) HAP planes growing on FAP. In contrast, the mutual orientation of FAP crystallization on HAP seed crystals could not be established. It is significant that the values of the TLW interfacial energies resulted in a calculated contact angle of 118° for FAP nucleation on an HAP substrate and a perfect wetting of 0° for HAP on FAP. The former system therefore represented a much higher energy barrier for nucleation, and the results deomonstrate the usefulness of surface energy measurements to predict and interpret the abilities of surfaces to nucleate minerals.[253] Similar surface energy considerations accounted for the epitaxial growth of DCPD on calcium sulfate dehydrate.[254]

3.3.3.5. Influence of Small Ions. It is clear from the foregoing that any discussion of the phase stability and crystal lattice substitutions of calcium phosphates must take into account the probable influence of extraneous small ions such as Mg^{2+}, Zn^{2+}, CO_3^{2-}, and F^-. The observation of deposits of ACP in liver mitochondria indicates the presence of natural inhibitors able to stabilize this phase in the presence of Mg^{2+}.[255] ATP and Mg^{2+} synergistically delay transformation to HAP by acting as growth poisons and allowing the cells to store ACP as a reservoir of calcium phosphate. Posner et al. also suggested that the binding of ATP and Mg^{2+} to HAP nuclei prevented their growth.[256] Regulation of the levels of ATP and Mg^{2+} might therefore allow the cells to store calcium phosphate as ACP until required for crystallization;[256] ATP also delays the *in vitro* onset of transformation of ACP. Both studies, therefore, suggest that the apparent stabilization of ACP may be due to binding of the inhibitors to newly formed nuclei, not only preventing these from reaching a critical growth size, but leading to redissolution.[257,258] Both Mg^{2+} and Zn^{2+} also inhibit HAP crystal growth. Clearly, the uptake of these small ions is mainly electrostatic, and their adsorption affinities are relatively small.[3] Consequently, higher concentrations are required in order to substantially reduce the rate of crystallization. It is interesting to note that the adsorption of Mg^{2+} continues at HAP seed surfaces, reaching a plateau with little further uptake. In contrast, Zn^{2+} binding increases monotonically with increased solution concentration beyond the point of monolayer coverage.[3] This is probably due to the precipitation of zinc phosphate at the apatite surface as the concentration of zinc ions is increased, and this is an important factor to take into account when attempting to interpret the results of simple ion uptake during adsorption experiments. The equilibrium adsorption of Zn and Mg ions on HAP and electrophoretic mobility measurements suggest that, at solution concentrations of zinc ion above about 1 ppm, the formation of zinc phosphate (hopeite) dominates the surface properties. In the presence of zinc and magnesium ions, the constant composition growth of HAP is markedly
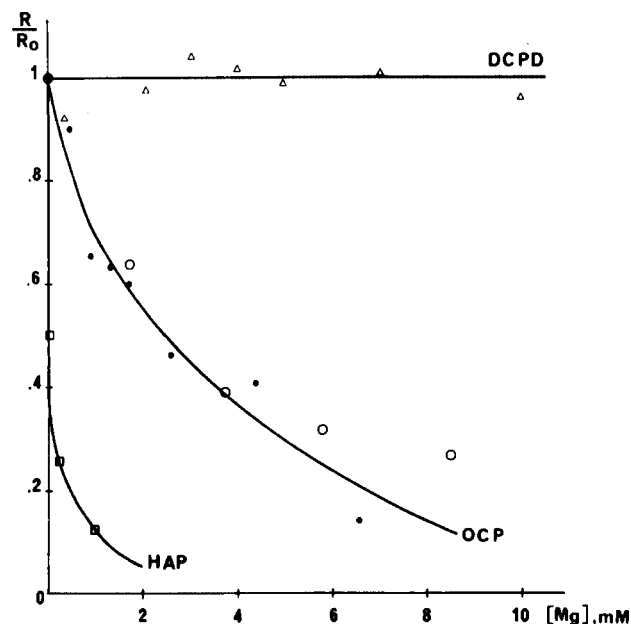

Figure 9. Normalized rates of growth of DCPD, OCP, and HAP in the presence of magnesium ions. R and R_0 are the rates of growth (mol min^{-1} m^{-2}) in the presence and absence of magnesium, respectively. Reprinted with permission from ref 117. Copyright 1985 the American Chemical Society.

reduced and the results suggest a Langmuir-type adsorption of these additives at active growth sites on the HAP crystals. Zinc ion is one of the most effective of the simple metal ions in inhibiting HAP crystal growth.[259]

The influence of fluoride ion is especially interesting in view of its importance in controlling caries. The accommodation of F^- at OH^- sites, forming a less soluble fluorohydroxyapatite phase, enhances the crystal growth reaction, reducing the rate of dissolution.[260,261] The influence of fluoride ion continues to be a subject of considerable interest, and although statements are made to the effect that fluorapatite catalyzes the formation of HAP, it should be remembered that a new phase is forming, namely, partially or totally substituted fluorhydroxyapatite.[3] The degree of substitution may be important, since studies of the solubility of apatites with various degrees of fluoride content have shown that partially fluoridated apatite may have a lower solubility than either HAP or FAP itself.[262] In contrast to fluoride, carbonate, which is also incorporated readily into the apatite lattice, inhibits HAP crystal growth, probably due to adsorption at surface sites and also the less favorable coordination in phosphate or hydroxide sites in the lattice.[263,264]

Studies of the crystallization kinetics of DCPD and OCP in the presence of impurities show, in general, a similar trend to that of HAP, although these hydrated phases are less sensitive. The observed differences in the degree of inhibition are important in helping to understand the nature of the calcium phosphate phases observed *in vivo*, especially for pathological mineralization processes. Thus, in a seeded CC crystal growth study,[117] it was shown that the magnesium ion markedly inhibits HAP crystal growth in a solution supersaturated only with respect to this phase, has a modest influence on the kinetics of OCP growth, and has practically no effect on DCPD crystallization (Figure 9).[117] A possible reason for this wide range of inhibition properties may be attributable to the presence of lattice water in OCP and DCPD, decreasing the adsorption of foreign ions. Magnesium is able to mediate in the precipitation process by selectively

stabilizing more acidic precursor phases.[265] Moreover, citrate and phosphocitrate showed similar influences on crystal growth of calcium phosphates.[266]

3.3.3.6. Influence of Macromolecules and Proteins. The crystallization of calcium phosphates must take into account the probable influence of biomacromolecules in the solution phase.[3,141] In general, at physiological pH, anionic proteins show a considerably greater influence on HAP crystallization than positive or neutral species, suggesting that they bind to calcium ions at the surface.[3] Moreover, their inhibiting influence during extended CC growth periods suggests that they are able to bind to active growth sites that may be formed during crystal growth, as well as those intrinsic to the seed crystallites. These inhibiting properties can be measured either by preadsorbing the molecules to HAP seed crystal surfaces before adding to calcium phosphate meta-stable solutions or by making CC crystal growth studies in solutions containing the additives. The general agreement between the results of these studies suggests that many adsorbed molecules are resistant to desorption from the seed crystals. Adsorption, in such cases, probably involves multiple binding sites at the surface.[3] Proteins or other macromolecules with an abundance of carboxylated amino acids influence the crystal morphology of a typical apatite precursor, OCP, differently than phosphorylated proteins.[267] These different morphological effects were attributed to the adsorption of the proteins to specific OCP crystal faces. The controlling factor that would dictate how this protein−crystal recognition alters crystal morphology could involve either crystal growth kinetics or protein inhibitory function.[267] CC growth kinetics of OCP in the presence of polyaspartic acid (PAA) and phosphophoryn (PPn) suggested their specific adsorption on the (100) and (010) DCPD faces, respectively.[268] Protein effects on crystal growth were examined at sustained constant supersaturation, and it was found that the maximum adsorbed molecular surface concentration for PPn was 100-fold less than that for PAA. Inhibitory effects, interpreted in terms of molecular surface coverage, showed PPn to retard OCP growth more effectively than PAA. However, when considering the percentage of crystal surface covered by protein, PAA and PPn showed similar maximum adsorption concentrations on the (100) and (010) faces. PAA inhibited OCP growth by 20% when only 1% of the (100) face (representing 1% total crystal area) was covered. PPn had to reach over 200% (010) face coverage (or 28% total crystal area) before a similar level of crystal growth inhibition was obtained.[268] This difference in inhibitory effect may be the result of a more effective β-strand conformation of the shorter PAA molecule or may indicate that the growth of the (100) face is rate controlling, and therefore >1% coverage of this face is needed before a significant decrease in rate is observed. When PPn area coverage was >100% of the (010) face, either multilayering occurred or only a segment of the molecule was attached to the crystal. At these higher concentrations, PPn may then be nonspecifically adsorbed to the (100) face and approach the level of PAA inhibition.[268] Moreover, both poly-L-Asp and poly-L-Glu behaved as HAP and OCP nucleators when immobilized on a germanium surface.[269] Despite the fact that the only difference in the structure is an additional CH_2 group on the side chain of the Glu residue, poly-L-Glu and poly-L-Asp are known to exhibit marked differences in their biochemical behavior as well as their involvement in biomineralization. The adsorption isotherms of these polyelectroytes were interpreted in terms of a Langmuir model, and a theoretical analysis of the data based on a model proposed by Hesselink suggested a "train-loop" type of adsorption with nonelec-trostatic energy terms 3.51 and $4.76kT$ for poly-L-Glu and poly-L-Asp, respectively.[270] CC kinetics studies of the nucleation of immobilized protein and other macromolecule surfaces showed that OCP was precipitated on phosphati-dylserine vesicles immobilized on germanium surfaces introduced into the calcium phosphate solutions supersatu-rated with respect to OCP.[271] The results again pointed to the involvement of an interaction of the calcium ions with the ionized carboxyate groups of the phospholipids.[271] For poly-L-aspartic acid (PLAA) influence on OCP growth, the crystallization of OCP from aqueous solutions at pH 5 resulted in the direct assembly of a complex inorganic-polymer spherical-shell architecture without the intervention of external templates.[272] The hollow microstructures consist of a thin porous membrane of oriented OCP crystals that are highly interconnected.[272] Bigi et al. continued to dem-onstrate that low PLAA concentrations (up to 22 μM) resulted in a reduction of the mean dimensions of the platelets and the formation of aggregates, which in the TEM-ED images appeared mostly as fibers aggregated parallel to their length and exhibiting unidirectional disorder in the direction orthogonal to the c-axis.[273] Relatively high PLAA concentra-tions (up to 110 μM) greatly reduced the total amount of crystal, which precipitated as almost spherical aggregates with increasing structural disorder.[273] The modification of the X-ray diffraction pattern on increasing PLAA concentra-tion indicates an increasing disorder and an increasing contribution of the apatitic layer of the OCP structure, which could be related to the observed reduction of thermal stability, and suggests a possible interaction of PLAA with the hydrated layer of OCP.[273]

The influence of several potential cariostatic agents, the organic phosphonates, on the growth of HAP indicated that traces of some phosphonates ($<10^{-6}$ M) are extremely effective in inhibiting mineralization. Their influence could be interpreted in terms of a Langmuir adsorption isotherm, with the phosphonate binding groups blocking active growth sites on the crystal surfaces. The evidence again strongly suggests a surface controlled mechanism for HAP crystal growth.[274] Furthermore, a fibroblast growth factor (FGF-2), introduced into calcium phosphate solution, resulted in an ACP-HAP phase transitions. The FGF-2 became enveloped by the HAP and not simply adsorbed at the HAP surfaces.[275] The presence of the cysteine-rich Mdm2 peptide (containing 48 amino acids in ring finger configuration) inhibited HAP crystal growth by 59−92% through adsorption at active growth sites. The kinetic results favored a Langmuir-type adsorption model, and the value of the calculated affinity constant was $k_{aff} = (258 \pm 21) \times 10^4$ dm^3 mol^{-1}.[276] At 37 °C, $I = 0.15$ M, pH 7.40, the rates of crystal growth measured in the presence of acetaminophen 1.654×10^{-4} mol dm^{-3} to 6.616×10^{-4} mol dm^{-3} were reduced by 43% to 79%, respectively. Kinetic analysis again suggested a Langmuir-type adsorption on the HAP surfaces with an affinity of 2.4×10^{-4} dm^3 mol^{-1}.[277] The modified peptides containing poly(aspartic acid), poly(glutamic acid), or a bisphosphonate (pamidronate) that have well-documented affinities to HAP, were incubated with HAP in phosphate-buffered saline at physiological conditions over 24 h, and a significant amount ($>90\%$) of conjugated peptides adsorbed to the HAP as compared to unmodified peptides ($<5\%$).[278]

Recombinant human-like type I collagen, an acidic protein, can direct growth of HAP nanocrystals *in vitro* in the form of self-assembly of nanofibrils of mineralized collagen resembling an extracellular matrix; mineralized collagen fibrils were aligned parallel to each other. HAP nanocrystals grew on the surface of these collagen fibrils with the *c*-axis of nanocrystals of HAP oriented along the longitudinal axis of the fibrils.[279] Controlled morphologies of ultraflat platelets of HAP with characteristic lateral dimensions in the micrometer range and a thickness of a few nanometers were grown at ambient temperature from supersaturated calcium and phosphate solutions in the presence of a bis-amidinium cation.[280] Morphologies of HAP with partial substitution of fluorine have also been finely modulated through alteration of the reaction conditions and the addition of glutamic acid.[281] Kniep et al. showed some evidence for a direct correlation between intrinsic electric dipole fields and the self-organized growth of FAP-gelatine. These fields are caused by a parallel orientation of triple-helical protein fibers of gelatine, in the case of FAP-gelatine seeds. The dipole field influences the further growth development of the seed, and in this way, it monitors the fractal morphogenesis of the composite aggregate.[282,283] However, this FAP-gelatin crystal growth phenomenon in the absence of gelatin was also reproduced, rendering these conclusions questionable. Prymak et al. showed that the special dumbbell morphology of FAP is due to the crystallization conditions (mainly pH and supersaturation) and does not require a specific additive or templating molecule.[284]

It is well-known that the most abundant noncollagenous protein in bone, osteocalcin, and several salivary proteins, such as statherin, bind strongly to HAP to regulate crystal growth. Thin apatite-like crystals with hexagonal symmetry grew on the (010) brushite planes. The apatite (0001) planes were fully covered with osteocalcin molecules. Thus, osteocalcin has been found to regulate HAP formation in two different ways: (i) it accelerates nucleation, and (ii) it acts as a specific inhibitor of the apatite (0001) plane, supressing crystal growth perpendicular to this plane. A stress-induced growth model was developed illustrating HAP growth along the brushite-HAP interface, taking into consideration compressions in the protein-covered HAP crystals.[285] Dowd et al. have solved the three-dimensional structure of osteocalcin using ^{1}H 2D NMR techniques and proposed a mechanism for mineral binding.[286]

As a model protein for studying molecular recognition at the protein–mineral interface, statherin has extensively served for understanding the functional activities of proteins in the physical-chemical control of HAP growth because statherin inhibits both the nucleation and the growth of HAP in the supersaturated solutions of saliva.[287–291] Salivary statherin is a highly acidic, 43 amino acid residue protein that functions as an inhibitor of primary and secondary crystallization of HAP. The acidic domain at the N-terminus was shown to be important in protein binding to HAP surfaces. The highly charged 15 residue N-terminal fragment shows greater adsorption at HAP surfaces and inhibition of mineralization in supersaturated solutions than fragments from the center of the molecule or the uncharged C-terminal end. Phosphoserine residues of statherin also appear to play a major role in HAP binding affinity,[292] although the negative charge density of the N-terminus rather than any specific interaction of phosphate groups is probably the most important factor in HAP surface interaction. N-Terminal

peptides also display functional activities in controlling HAP growth.[293] Secondary sequence predictions suggest that the N-terminus has a propensity for α-helix formation, and circular dichroism studies have demonstrated the presence of some α-helical conformations in solution.[292] Moreover, another model protein, phosphorylated osteopontein (OPN) appears to have a major role in the influence of OPN on crystallization and crystal shapes; HAP crystal growth was markedly reduced by dephosphorylation of OPN.[294]

The combination of two protein inhibitors may result in a mixture with an inhibitory activity greater than the sum of the two, suggesting the inhibitory activity of a protein does not completely correlate with Ca^{2+}-binding affinity. Thus, γ-carboxyglutamic acid residues enhance the ability of a protein to inhibit HAP-seeded crystal growth.[295] Jahnen-Dechent et al. suggested that $α_2$-HS glycoprotein/fetuin-A inhibited calcium phosphate precipitation by an extended β-sheet of the cystatin-like domain.[296] Kandori et al. showed that the adsorption rate of lysozyme (LSZ) was greater than that of bovine serum albumin (BSA) due to its larger diffusion coefficient, though the saturation adsorption amount of LSZ was less than that of BSA.[297] The rates of BSA adsorption onto HAP did not change by the addition of LSZ, while those of LSZ were considerably reduced by the addition of BSA due to forming (BSA^--LSZ^+) agglomerates in the solution.[297] The cooperative adsorption behavior of LSZ was observed in the presence of lower amounts of BSA due to the preferential adsorption of the larger (BSA^--LSZ^+) agglomerates. However, in the case of higher BSA content, the adsorption of LSZ was inhibited by capturing the LSZ molecules in the (BSA^--LSZ^+) agglomerates. The similar cooperative adsorption behavior of BSA was also observed on all systems examined in the presence of various amounts of LSZ.[297] In order to clarify the adsorption mechanism of proteins onto HAP surfaces, the adsorption (ΔH_{ads}) and desorption (ΔH_{des}) enthalpies of BSA and myoglobin (MGB) onto HAP were measured with a flow microcalorimeter (FMC).[298] ΔH_{ads}^{BSA} decreased with the pH increase and HAP crystallinity, suggesting that the BSA adsorption readily proceeded onto HAP. This fact indicated a high affinity of HAP for protein. The opposite tendencies in ΔH_{ads}^{BSA} and ΔH_{des}^{BSA} revealed that HAP possessed a high adsorption affinity for BSA (i.e., enthalpy facilitated protein adsorption but hindered its desorption).[298] Similar results were observed with the LSZ system, though the enthalpy values were smaller than those of BSA. In the case of neutral MGB, ΔH_{ads}^{MGB} also exhibited results similar to those of the BSA and LSZ systems. However, due to its weak van der Waals adsorption, ΔH_{des}^{MGB} was small and almost zero at a high pH value.[298]

Many attempts have been made using other methods to interpret inhibitory or promotion roles of additive molecules. Barralet et al. used a ξ potential method and found a strong increase in the surface charge of TCP and DCPD, as determined by ξ potential. In contrast, the calcium salts of α-hydroxylated organic acids did not alter ξ potentials due to the formation of neutral and stable complexes in aqueous solution.[299] Significant differences in the affinity constants among the bisphosphonates (BPs) for HAP calculated from kinetics data were best explained by variation in molecular charges based on the extent of side chain protonation. ξ potential data showed that the crystal surface was modified by the adsorption of BPs to change solid/liquid interfacial properties, subsequently, to result in the differences in their

binding and inhibition of crystal growth and dissolution.[300] It was also verified that the multilayers modified with model organic molecules of either poly(styrene sulfonate) (PSS) or poly(allylamine) (PAH) exhibited a negative or positive ξ potential, respectively.[301] The effective surface free energies of the crystals formed were estimated to be on the order of 32 mJ·m^{-2} on a multilayer terminating with PSS and to be about 37 mJ·m^{-2} on a multilayer with PAH.[301] These values are lower than the surface tensions 289 mJ·m^{-2} for FAP[302] and 87 mJ·m^{-2} for HAP.[206] This suggests that the poly-electrolyte multilayers are very effective nucleating agents for calcium phosphate crystals. They can also be compared with the surface free energy of the overgrowth based on heterogeneous nucleation of HAP on various substrates as 152 mJ·m^{-2} on DCPD,[83] 93 mJ·m^{-2} for HAP,[303] 70 mJ·m^{-2} on collagen,[241] 55 mJ·m^{-2} on phospholipids,[304] 90 mJ·m^{-2} on highly phosphorylated proteins,[305] and 92 mJ·m^{-2} for phosphorylated copolymers.[303] Moreover, an increase of the concentration of some ions near the top polyelectrolyte layer of the polyelectrolyte multilayers may lead to a decrease of the supersaturation ratio for heterogeneous nucleation and growth of calcium phosphate crystals.

In general, the composition of biological molecules suggests that control of mineral growth is linked to their biochemical features. Recently, Elhadj et al. used AFM to define a systematic relationship between the ability of biomolecules in solution to promote the growth of calcite and their net negative molecular charge and hydrophilicity.[306] This rate enhancement arises from an increase in the kinetic coefficient, whereby biomolecules reduce the magnitude of the diffusive barrier, E_k, by perturbations that displace water molecules.[306] The result is a decrease in the energy barrier for attachment of solutes to the solid phase. These findings show that the growth-modifying properties of small model peptides may be scaled up to analyze mineralization processes that are mediated by more complex proteins.

3.3.4. Crystal Surface Dynamics

3.3.4.1. General Considerations. Although CC has many advantages for quantitative studies of crystal nucleation and growth, it is a bulk method with a limited ability to provide molecular scale information. Molecular level views of crystal growth and inhibition have recently evolved using techniques such as AFM for quantifing crystallization kinetics of specific crystal faces in the absence and presence of additives. AFM is the only tool that allows investigation of solution crystal growth at length scales ranging from that of individual molecules to entire 100 μm crystal faces in real time.[307,308] AFM revealed the relationship between molecular structure and growth features on crystals such as DCPD,[309] COM,[310] and calcite.[137] Quantitative studies have enabled incisive investigations of modulator effects on the morphology,[311−313] kinetics,[314−316] and energetics of crystal growth, as well as the kinetics and morphologic features of nucleation.[308,317] By combining AFM measurements with CC measurements and molecular modeling, all length and time scales from macroscopic growth rates to the sites of molecular interactions and binding energies can provide an understanding of the mechanisms of nucleation and growth modulation.[141] A key to a more fundamental understanding of the control of functional and pathological mineralization in biological systems is quantitative molecular-scale definition of the impact of biological surfaces and soluble modulators on the crystallization process.[160]

3.3.4.2. Adsorption of Molecules at HAP Surfaces and Protein−Mineral Molecular Recognition. Protein−mineral molecular recognition at the organic−inorganic interface clearly plays an important role in biomineral formation through the adsorption of molecules to HAP crystal faces.[318−321] The growth inhibitory effect depends on the nature of the amino acid side groups[322−324] and protein conformations, such as a α-helix or β-sheet.[325] The key questions are as follows: how amino acid side chains come into contact with the crystal surface and how the structures and orientation of protein are related to the dual function of inhibiting or promoting HAP nucleation/growth. Recent solid-state NMR studies of N-terminal statherin peptide fragments suggested the importance of water either in mediating the interaction of the acidic side chains with the HAP surface or in directly stabilizing the α-helix conformation.[326−328] It has been previously proposed that the α-helix motif could be used as a scaffolding mechanism for aligning acidic side chain residues with HAP by lattice matching through a more general electrostatic complementarity.[329,330]

Raghunathan et al. incorporated this coupling to reanalyze the ^{15}N$\{^{31}$P$\}$ rotational-echo double-resonance (REDOR) NMR measurement of the lysine side chain of statherin approaching the HAP surface and have refined the binding models proposed earlier.[331] ^{15}N$-^{31}$P distances between 3.3 and 5 Å from these models are indicative of the possibility of a lysine−phosphate hydrogen bond.[332] In the peptide fragment derived from the N-terminal 15 amino acids of salivary statherin (i.e., SN-15), the side chain of the phenylalanine nearest the C-terminus of the peptide (F14) is dynamically constrained and oriented near the surface, whereas the side chain of the phenylalanine located nearest to the N-terminus of the peptide (F7) is more mobile and is oriented away from the HAP.[333] A further solid-state NMR measurement showed that the statherin C-terminal region folds into an α-helix upon adsorption to HAP crystals.[334] The helical segment is shown through long-range distance measurements to fold back onto the intermediate region (residues Y16−P28), defining the global fold of the protein. Statherin, previously shown to be unstructured in solution, undergoes conformation selection on its substrate mineral surface.[334] This surface-induced folding of statherin can be related to its functionality in inhibiting HAP crystal growth.[334]

Statherin adsorption is characterized by an exothermic enthalpy of about 3 kcal/mol that diminishes to zero at about 25% surface coverage. The initial heat of statherin adsorption increases with temperature, displaying a positive heat capacity change of 194 ± 7 cal K^{-1} mol^{-1} at 25 °C.[335] The free energy of adsorption is dominated at all coverages by a large positive entropy (≥ 23 cal K^{-1} mol^{-1}), which may be partially due to the loss of organized water that hydrates the protein and the mineral surface prior to adsorption.[335] Single point mutations of the basic side chains to alanine lowered the binding affinity to the surface but did not perturb the maximal surface coverage and the adsorption enthalpy. Simultaneous replacement of all four basic amino acids with alanine lowered the adsorption equilibrium constant by 5-fold and the maximal surface coverage by nearly 2-fold.[335] The initial exothermic adsorption exhibited by native statherin is preserved in this mutant, along with the α-helical structure and the dynamic properties of the N-terminal domain. These results help to refine the two binding site models of statherin adsorption of wild-type statherin.[335] The basic charges

function to reduce protein–protein charge repulsion on the HAP surface, and in their absence, there is a considerable decrease in statherin packing density on the surface at binding saturation.[336] All-atom Monte Carlo plus-minimization search algorithms applied to the statherin–HAP system revealed a molecular recognition motif of statherin for HAP.[337] The simulations isolate particular residues as being primary contributors to the adsorption free energy (hydrogen bonding, van der Waals, and electrostatic energies),[337] in agreement with previous mutagenesis, deletion, and single amino acid experiments. Moreover, a molecular recognition motif of the N-terminal α-helix of statherin places all four of its basic residues to match the periodicity of open phosphate triad clusters across the [001] monoclinic face of the HAP surface.[337]

There are various interactions between additive molecules and HAP crystal faces, one being hydrogen bonding between carboxylate groups in macromolecular side chains and the surface P–OH groups of HAP crystals.[338] A solid-state NMR experiment showed the possible calcium phosphate crystal surface binding site of a glutamate carboxylate group.[339] Adsorption of low molecular weight poly(acrylic acid) from aqueous solution on HAP showed that the irreversible isotherm first rises, to a maximum, and then decreases.[340] This is qualitatively explained on the basis of the increasing self-association of polymeric molecules with concentration and the inability of associated molecules to adsorb as their hydrogen bonding capability is used up.[340] Moreover, the detailed adsorption behavior of glycine (Gly) and glutamic acid (Glu) on HAP (001) and (100) crystal faces by molecular dynamics (MD) simulation suggested that the positive amino groups occupied vacant calcium sites, and their negative carboxylate groups occupied vacant P or OH sites as an ordered adsorption layer was formed.[341] The AFM pulling studies and free energy calculation showed that Glu was much more difficult to pull off the HAP (001) face than the (100) face. This result indicated that Glu preferentially adsorbed to the HAP (001) face, resulting in the formation of platelike HAP crystals. However, Gly did not show any significant preferential adsorption between these two HAP faces. Thus, the habit of rodlike HAP crystallites was not altered during the HAP crystallization in the presence of Gly.[341] Computer modeling also suggested that citric acid would more strongly inhibit growth of surfaces other than {0001}, leading to an elongated morphology in the *c*-direction of the apatite crystal.[342] Modeling techniques were also employed to investigate the adsorption of some relatively large, organic surfactant molecules to FAP surfaces.[343] The adsorbates coordinate mainly to the surfaces through interaction between their oxygen (or nitrogen) atoms and surface calcium ions, followed by hydrogen-bonded interactions with surface oxygen ions and, to a much lesser extent, surface fluorides sites. All adsorbates containing carbonyl and hydroxy groups interact strongly with the surfaces, releasing energies between approximately 100 and 215 kJ mol^{-1}, but methylamine, containing only the -NH$_2$ functional group, adsorbs to the surfaces to a much lesser extent (25–95 kJ mol^{-1}).[343]

In addition to the adsorption of molecules to crystal faces, crystal surfaces can also induce peptide/protein folding and conformational changes. A de novo designed peptide, JAK1, undergoes surface-induced folding at the HAP–solution interface.[344] HAP-induced folding is largely governed by periodic positioning of γ-carboxyglutamic acid (Gla) residues within the primary sequence of the peptide.[344] This study demonstrates the feasibility of using HA surfaces to trigger the intramolecular folding of designed peptides. Moreover, a proline-rich acidic salivary protein (PRP1), upon binding to HAP or CAP, undergoes significant conformational changes, from the random coil domain to the β-turn.[345] The results demonstrate that binding to apatitic mineral surfaces leads to major conformational changes in PRP1, which might reflect the expulsion of water and the formation of protein–mineral and/or protein–protein interactions in the adsorbed layer.[345]

X-ray crystallography is another excellent tool for the analysis of protein–mineral interaction. However, the prerequisite is the need to acquire pure protein crystals. Osteocalcin is the first protein related to bone biomineralization analyzed at 2.0 Å resolution by X-ray, which reveals a negatively charged protein surface that coordinates five calcium ions in a spatial orientation that is complementary to calcium ions in a HAP crystal lattice.[346] Figure 10 shows a model of porcine osteocalcin (pOC) engaging a HAP crystal based on a Ca^{2+} ion lattice match. The tertiary structure of the protein consisted of an unstructured N terminus and a C-terminal loop (residues 16–49) formed by long-range hydrophobic interactions. One calcium atom was coordinated by three side chain oxygen atoms, two from Asp30 and one from Gla24. The second calcium atom was coordinated to four oxygen atoms, two from the side chain in Gla 24 and two from the side chain of Gla 21. The third calcium atom was coordinated to two oxygen atoms of the side chain of Gla17.[346]

3.3.4.3. Growth Rate of Calcium Phosphate Crystal Faces by AFM. Growth takes place by the deposition and incorporation of dissolved solute molecules onto steps on the crystal surfaces, causing them to advance quickly along the surface, perpendicular to the step.[347] The growth of crystals by facets usually occurs in the classic spiral pattern predicted by BCF,[348,349] whereby one or more screw dislocations on the crystal surface provide a continuing source of steps. The important parameters controlling the growth rate are the energy required to create a step at the crystal surface and the free-energy barrier for an adsorbed solute molecule to be incorporated into the crystal.[347] In this process, the incorporation of these "growth units" into kinks is rate-determining at relatively low supersaturation. Kink sites are the most reactive portions of step edges (Figure 11A). At higher supersaturations, a "birth and spread" growth model predicts two-dimensional (2D) nucleation on existing crystal surfaces (Figure 11B).[350] Hannon et al. used low-energy electron microscopy to provide a real-time picture of the motion of steps on the surface and to observe these spiral shapes.[351] Clearly, crystal growth is limited to specific experimental conditions with various driving forces and requires modification to provide a general description of crystal growth.[352]

Many AFM studies have investigated step velocity (v_i) and morphology.[160] A basic parameter controlling step growth is the step length; the classic Gibbs–Thomson (G-T) effect predicts that the critical length (L_c) near equilibrium is related to the step-edge free energy (γ) and supersaturation (σ) ($L_c \propto \gamma/\sigma$).[137] The impact of the Gibbs–Thomson (G-T) effect is that growth occurs exclusively at dislocation hillocks where steps always exist. Therefore, the step free energy can be obtained from the critical length as a function of supersaturation. This concept of critical size also applies
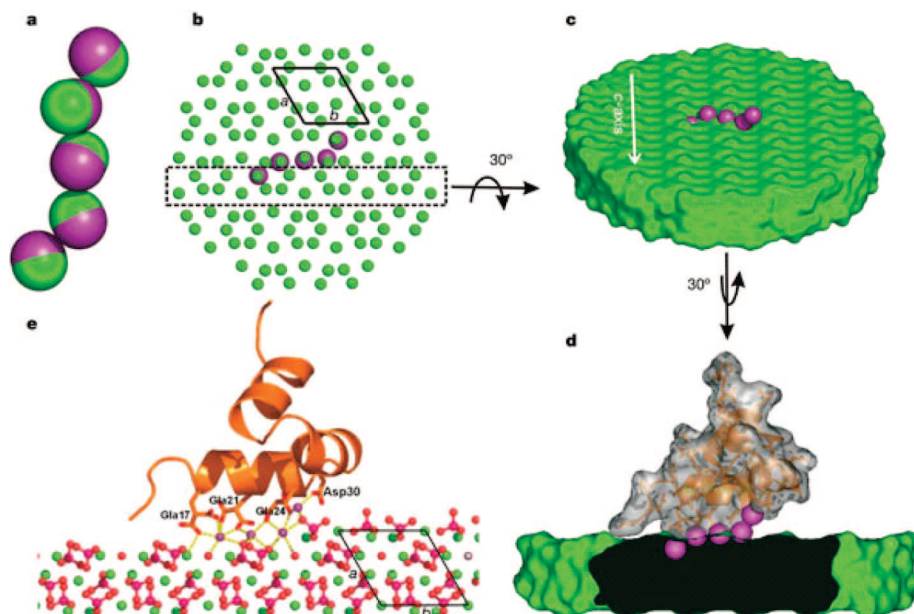
Figure 10. Model of porcine osteocalcin (pOC) engaging a HAP crystal based on a Ca^{2+} ion lattice match. (a) Alignment of pOC-bound (purple) and HA (green) Ca^{2+} ions. (b, c) Orientation of pOC-bound Ca^{2+} ions in a sphere of a HA-Ca lattice (b) and on the HA surface (c). In part b, the parallelogram indicates a unit cell; the box approximates the boundary of the slab shown in parts c and d. (d) Docking of pOC (orange backbone with gray semitransparent surface) on HAP. (e) Detailed view of part d showing the Ca–O coordination network at the pOC–HA interface. Yellow broken lines denote ionic bonds. Isolated red spheres and tetrahedral clusters of magenta and red spheres represent OH^- and PO_4^{3-} ions, respectively. Reprinted with permission from ref 346. Copyright 2003 Nature Publishing Group.

to step segments. A step segment advances as a new step edge is created adjacent to the segment (Figure 11C, D). As a step advances from a dislocation, the new side created along a step does not advance until a critical length (L_c) is attained. This side then advances and creates another new side.

In addition to the parameters discussed above, AFM studies of crystal growth provide molecular-scale information defining a kinetic coefficient (β) based on the following equation.

$$v_i \propto \beta(a - a_e) \tag{3.34}$$

where a and a_e are the actual and equilibrium solute activities in the regime of linear kinetics and, β, the kinetic coefficient, is a constant.

$$\beta \propto \exp(-E/kT) \tag{3.35}$$

In eq 3.35, E is the activation energy barrier required for all the processes that take place at the crystal surface (adsorption, incorporation, attachment at a kink, etc.), but in the slow crystal growth of apatite, where the incorporation process governs the growth rate, it may be regarded as the activation energy required for the incorporation of growth units. The magnitude of β is controlled by two primary factors, the first is the density of kink sites along the step, and the second is the net probability of attachment to a site.[306] β is assumed to scale with surface impurity coverage in the presence of impurity.

Understanding the true nature of the apatite crystal growth mechanism involves identifying the stages that control the growth rate. Onuma et al. tracked the movement of steps from a series of captured AFM images and thereby determined the step velocity.[353,354] The step kinetic coefficient of the HAP a-face was calculated to be 0.4×10^{-4} cm/s, that is smaller than those of most inorganic salts (about 10^{-3} cm/s)[355,356] and similar to those of proteins (10^{-4} to 10^{-5} cm/s).[357–359] Compared with the values for other types of soluble inorganic crystals and organic proteins, it is hypoth-

esized that the growth units of apatite are not small ions but large clusters.[89] If this result is correct, the c-face should grow by this cluster mechanism. However, it is difficult to measure this face growth rate by AFM because the thickness of the crystal surface increased more or less uniformly, so that there were no immovable points in the field of view to act as the reference markers necessary for AFM measurement.[89] Alternatively, therefore, the growth rate was measured using "real-time phase shift interferometry".[360,361] Based on the growth rates at various supersaturations, the edge free energy $\gamma = 3.3kT$ was derived. This value is very close to that for a lysozyme protein crystal[362] and much larger than that for crystals of soluble inorganic salts ($\gamma < 1kT$).[363] This suggests that c-face growth rate measurements confirm the cluster growth model hypothesis derived from observations of the a-face.[89]

3.3.4.4. Cabrera–Vermilyea (C–V) Step Pinning Model. The Gibbs–Thomson (G-T) effect also plays an important role in control of crystal growth by modulators or impurities. Indeed, organisms have already applied impurity strategies to tune physical and chemical properties, reflecting a specific control over the nucleation, growth, and shape of mineralized tissues. For example, fluoride ions incorporate into the outer layer of tooth enamel to reduce the onset of apatite dissolution,[108] and magnesium enhances mineral solubility through incorporation to inhibit calcite growth.[364] Some small organic molecules such as chiral amino acids adsorbed to calcite surface steps result in macroscopic crystal shape modifications by a change of interfacial energies.[312] De Yoreo et al. proposed four mechanisms of microscopic crystallization dynamics influenced by impurities:[160] (1) step pinning, (2) incorporation, (3) kink blocking, and (4) step edge adsorption. Each of these major mechanisms for growth inhibition exhibits a characteristic dependence of step speed on supersaturation and impurity concentration.[141,365] A classical model of growth inhibition known as the Cabrera–Vermilyea or C-V model[366] explained quantita-
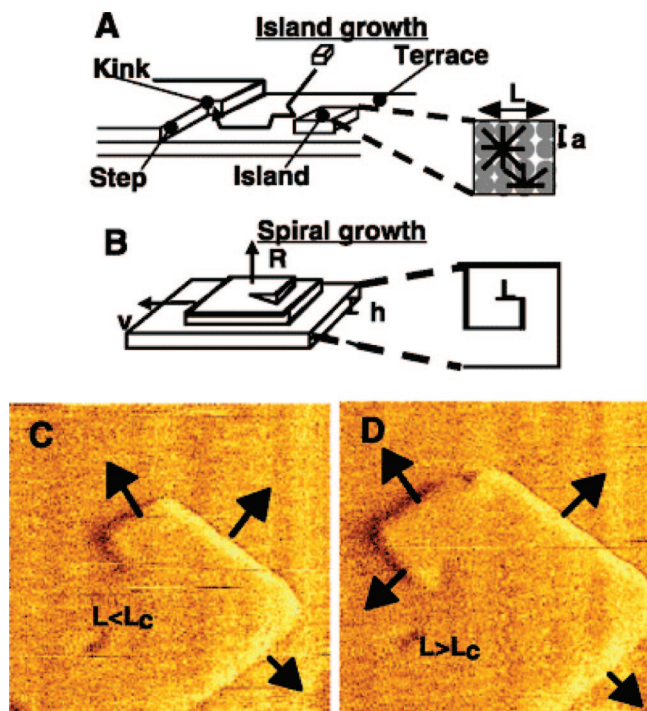
Figure 11. Illustration of growth at a crystal surface by attachment of molecules to step edges on either islands (A) or dislocation spirals (B). (C and D) Sequential AFM images showing the portion of the growth spiral with $L < L_c$ at $t = 0$ and $L > L_c$ at $t = 25$ s. Step edges with arrows are advancing. L is the length of a step edge, L_c is the critical length of a step edge, a is the distance between two adjacent atoms in the crystal lattice, v is the velocity of step movement, R is the growth rate, and h is the step height. Reprinted with permission from ref 160. Copyright 2003 Mineralogical Society of America.

tively the crystal growth inhibition by citrate at both microscopic[367] and macroscopic[368] levels.

In the C-V model, the influences of impurities on crystal growth are attributed to their adsorption at kinks, edges, and terraces of a growing surface, thus reducing the growth rate by hindering the movement of growth steps.[314,369] Impurities adsorbed at step edges or on the terraces ahead of migrating steps create a field of "impurity stoppers" that act to block the motion of elementary steps, thereby decreasing their velocity. When the average spacing between impurity molecules (L_i) is less than a critical distance, whose magnitude is given approximately by the G-T critical diameter ($2r_c$), the steps are unable to advance. As a consequence, the C-V model predicts the presence of a "dead zone"—a region of positive supersaturation (σ_d) where no growth occurs. As the supersaturation is increased beyond σ_d and the critical diameter becomes smaller than L_i, the steps begin to squeeze through the "fence" of impurities and the step speed (v_i) rises rapidly, eventually reaching that of the pure system.[370] Despite the general acceptance of this theory, no macroscopic observations of growth rates have ever been directly linked to this microscopic impurity step-pinning model. Irrespective of which crystal faces are affected, the theoretical C-V relationship for the relative growth rate and impurity concentration is given by eq 3.36:

$$\frac{R_i}{R_0} = 1 - Dr_c C_i^{0.5} \text{ for } Dr_c C_i^{0.5} \leq 1 \quad (3.36)$$

where D is a coefficient that reflects a combination of geometric factors of the crystal lattice, sticking probability,
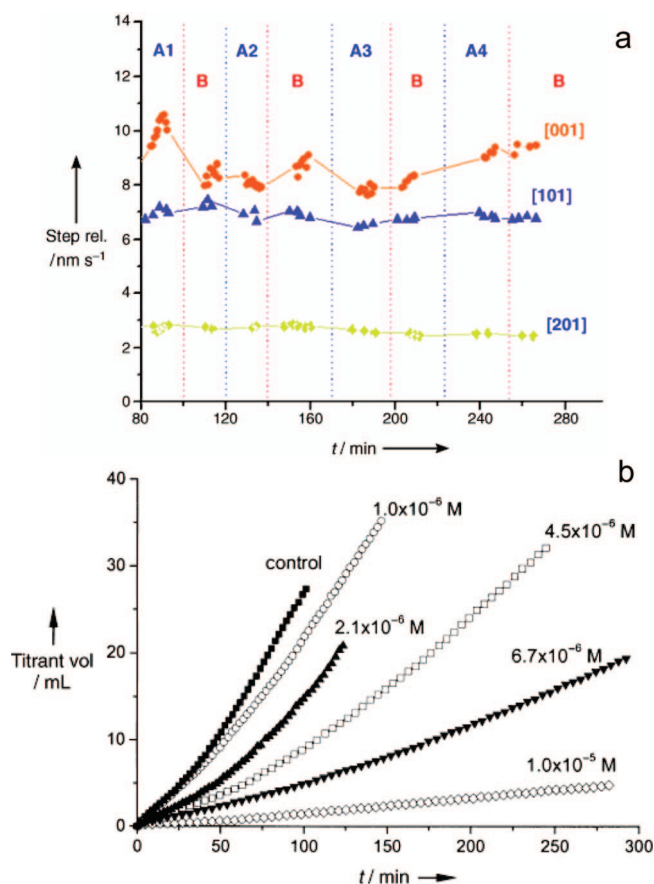

Figure 12. (a) Evolution of the velocities of all three steps for DCPD crystals grown in solutions with and without citrate. All experimental conditions were kept constant, and there was no change in the spreading rates of steps in the absence and presence of citrate. The vertical red dotted lines indicate the time at which the crystals were exposed to a pure growth solution supersaturated with calcium phosphate (marked as B areas), while the blue dotted lines indicate the times at which the growth solutions contained citrate. In areas A1, A2, A3, and A4, the citrate concentrations were 1.0×10^{-6}, 5.0×10^{-6}, 1.0×10^{-5}, and 2.0×10^{-5} M, respectively. (b) CC growth curves of brushite in the presence of citrate. The relative supersaturation with respect to brushite (σ) was 0.250; the pH value and ionic strength were 5.60 and 0.15 M, respectively; the curves have been normalized to the same seed mass of 10.0 mg. Reprinted with permission from ref 373. Copyright 2005 from Wiley-VCH.

and impurity lifetime on the surface. C_i is the bulk solution concentration of impurity. r_c is the G-T critical radius that is given by

$$r_c = \frac{\gamma\Omega}{kT\sigma} \quad (3.37)$$

Here γ is the step-edge free energy per unit step height, Ω is the molecular volume, k is Boltzmann's constant, and T is the absolute temperature. Consistent with the AFM step speed observations,[371] bulk CC growth rates were observed to gradually decrease with an increase of citrate concentration at different supersaturations.[368,372] This is the first experimental evidence of the inhibition of bulk crystallization that can be reasonably explained by a microscopic C-V model.

3.3.4.5. Step Density and Interfacial Energies. The interaction of citrate with DCPD reveals another mechanism by which impurity molecules reduce step density without influencing the step speed and morphology.[373] Figure 12a shows that the velocities of all three steps on DCPD (010)

faces are not significantly changed in the presence of citrate. Although the measured step velocities are not perfectly constant, the maximum variation is only about 10%. Nevertheless, in parallel CC experiments, citrate effectively retards the bulk growth rate (Figure 12b).[373] It is important to question how the microscopic AFM step kinetics can be reconciled with the bulk CC kinetics. One possibility is that citrate may modify the step kinetics of other faces rather than the (010) face or decrease the step density. Taking the average distance between two steps in a spiral growth as λ_0 (spacing) and their heights as d_{hkl}, the growth rate of one face is given by $R_{hkl} = v_{step}d_{hkl}/\lambda_0$, thus showing that a lower density (larger spacing between parallel steps) has a lower face growth rate.[141]

AFM results for a DCPD (010) face in the absence and presence of citrate showed that citrate dramatically decreases the step densities, especially,[101] and [001] steps,[373] and this accounts for the observed inhibition in the bulk CC growth experiments. If this new step segment remains at equilibrium with the adjacent reservoir of growth units, then it will only advance with the change in free energy, ΔG. The total change in free energy of the system is given by eq 3.38:

$$\Delta G = -n\Delta\mu + 2a\gamma \qquad (3.38)$$

Here, $n = L/b$, L is the length of the step, b is the intermolecular distance along the step, a is the distance between rows, and $\Delta\mu$ is the change in chemical potential per growth unit during this phase transformation. The second term gives the free energy of the step edge γ. Setting ΔG to zero and substituting $kT\sigma$ for $\Delta\mu$ shows that the free energy only decreases if the length of the step exceeds a critical value, L_c ($L_c = 2bc\gamma/kT\sigma$). AFM images[373] show that the smallest step is below the critical length and is stationary, but when it has exceeded the critical length it begins to move. Step density is a function of the time that it takes for a new step to begin to move. This can be related to the critical length or to the probability of nucleating a kink, depending on whether thermodynamics or kinetics is in control.[141] If the steps are at equilibrium, the increase in step density implies an increase in the critical length and a concomitant increase in step free energy. The interfacial tensions of DCPD exposed to solutions with increasing citrate concentrations measured by a thin-wicking method directly confirmed that the presence of citrate molecules may decrease the growth rate by altering the interfacial energies and corresponding step density.[373] This study suggests that the presence of additive molecules may modify the growth rate by changing the step density and/or the interfacial energies; and this finding broadens our understanding of the mechanisms of biomineralization.

4. Dissolution

By analogy to growth, the dislocation-based BCF model and the 2D-nucleation model predict rates that vary with the Gibbs free energy change ($\Delta G < 0$) of the dissolution reaction. The most often invoked relation has been based on the principle of detailed balancing or transition state theory, leading to the rate law shown as eq 4.1[374]

$$R = A_c(1 - e^{\alpha(\Delta G/kT)}) \qquad (4.1)$$

where A_c and α are general constants, dependent on pH, temperature T, or inhibitor molecules. However, complexities involving wide ranges of defects (pits) and active surface-

chemistry of mineral structures are expected in the dissolution of rocks and biominerals.[375,376] Many inconsistencies in dissolution studies cannot be explained by the largely kinetic "laws". Therefore, it is important to analyze the possible kinetic surface characteristics and then understand the deviations from eq 4.1 under actual dissolution reaction conditions.

4.1. Dissolution Model at the Nanoscale

Unlike BCF or 2D nucleation mechanisms, eq 4.1 does not contain surface molecular complexes such as etch pits as rate-determining factors in crystal dissolution. Recently, AFM studies on the dissolution of sparingly soluble calcium phosphates have revealed that pit formation and growth are the principal elements of the dissolution process and that the microscopic critical size effects should be embodied in any macroscopic dissolution model under similar experimental conditions.[309] The self-inhibiting effects observed in bulk dissolution using a CC method show that particle size greatly influences the kinetics.[376]

Figure 13a and b illustrates the dissolution of a (010) DCPD face close to equilibrium; the pit steps lose their orientations and become isotropic. However, their dissolution still proceeds by the initiation and growth of pits.[377] Only the spreading of large pit steps ($>0.2-0.4$ μm) contributes to dissolution. Although small pits are present ($<0.2-0.4$ μm), three types are recognizable, shown as 1−3 in Figure 13. The smaller pits, 1 and 2, in comparison with the larger pit, make only extremely small contributions to dissolution. Some, such as pit 3, even disappear from the surface during dissolution. Figure 13c shows the relationship between the expanding velocities and sizes of (201) and (001) steps on dissolving (010) brushite faces, as revealed by AFM.[377] At the lower relative undersaturation, 0.060, with the experimental critical pit sizes of $0.2-0.3$ μm, the step displacement velocities are extremely low, but with increase in size, the dissolution rate increases and tends to reach a relatively constant value. In comparison with the value for $\sigma = 0.060$, the rates at $\sigma = 0.172$ increase much more rapidly and achieve a high, relatively constant, value.

These results can be explained in terms of a dissolution model incorporating particle size considerations.[376] Demineralization of sparingly soluble salts such as HAP is generally initiated and accompanied by the formation and development of pits on the crystal surfaces, and the dissolution rates are also determined by the pit densities and spreading velocities. Analogous to the formation of two-dimensional nuclei/hillocks for crystal growth, in dissolution, the rate of step movement from a pit of radius r can be obtained based on the above analysis:[376]

$$R(r) = R_\infty\left[1 - \frac{e^{(1-S)r^*/r} - 1}{e^{1-S} - 1}\right] \qquad (4.2)$$

$$\approx R_\infty\left(1 - \frac{r^*}{r}\right) \qquad (4.3)$$

where r^* is the critical radius for the formation of a two-dimensional pit/dissolution step. R_∞ is the velocity of dissolution steps at $r \to \infty$.

According to classical nucleation theory (CNT), the free energy, ΔG, for the nucleation of a pit is[378]

$$\Delta G(r) = \frac{\pi r^2 h}{\Omega} kT \ln S + 2\pi r h \gamma \qquad (4.4)$$

where r is the radius and h is the depth of a pit, γ is the surface free energy, and Ω is the molecular volume. When $S < 1$, the solutions are undersaturated, and the first term on the right side of eq 4.4 is negative, reflecting the decrease of chemical potential, but the second term is positive due to the increase of surface roughness (pit formation) with loss of crystal mass and expansion of the solid−liquid interfacial area.[378,379] Thus, the dependence of the Gibbs free energy on the radius (r) passes through a maximum, and the critical size (i.e., r^*) can be obtained by setting $\partial(\Delta G)/\partial(r) = 0$; thus,

$$r^* = \frac{\gamma \Omega}{|kT \ln S|} \qquad (4.5)$$

It has been shown that only pits which are larger than r^* provide the active dissolution sites that contribute to dissolution. When r is closer to r^*, there is no fast movement of its stepwave and the dissolution rate approaches zero. In terms of the dissolution model (eq 4.2), the small size, 0.2−0.4 μm, can be regarded as having the critical dimension for pits and steps under these dissolution conditions (Figure 13 a, b). Since r^* is a function of undersaturation (eq 4.5), these critical values, at $\sigma = 0.172$, for (201) and (101) steps are reduced to about 0.06 and 0.08 μm, respectively (Figure 13a, b). The solid and dashed lines in Figure 13c show the good agreement between the value calculated using eq 4.2 and the AFM experimental results, which implies that, on a microscopic physical level, the dissolution rate is a function of the step size and its critical value.[309,377]

This is consistent with the CC bulk dissolution results,[380,381] which show that, for crystallite sizes approaching the critical values, the rates (the slopes of the CC curves in Figure 14a) decrease markedly with time despite the sustained driving force. At a high undersaturation ($S = 0.02$), HAP seed crystals undergo rapid dissolution and almost all of the solid phase is dissolved in less than 3 h. However, at lower undersaturation, the rates decrease during the reaction; at $S = 0.580$, the initial rate, $3.2 \pm 0.2 \times 10^{-7}$, decreases to $1.6 \pm 0.1 \times 10^{-7}$ mol m^{-2} min^{-1} and $0.8 \pm 0.1 \times 10^{-7}$ mol m^{-2} min^{-1} at 50 and 90 min, respectively. The CC dissolution curves reach plateaus prior to complete dissolution, thus indicating the creation of metastable states in which the reaction is effectively terminated even though the HAP crystallites remain in contact with the undersaturated solutions. At $S = 0.315$, 90% (by mass) of the seed crystals are dissolved and this decreases markedly with deceasing undersaturation; at an undersaturation of 0.580, only a relatively small fraction (38%) of the apatite crystallites undergo dissolution before the reaction is effectively stopped or reduced to a very low rate. No immediate CC dissolution of the seed crystallites could be detected at lower undersaturations ($S = 0.828$). Clearly, this dissolution termination is a kinetic phenomenon and cannot be attributed to reaction retardation as a result of surface modification by additives.
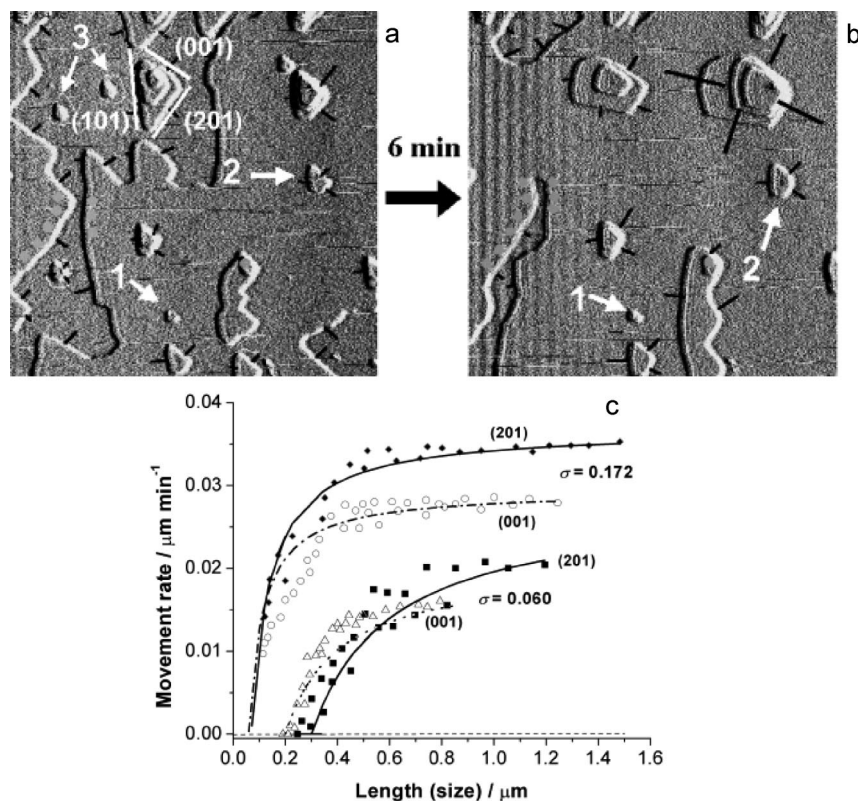

Figure 13. (a, b) AFM movie frames of brushite dissolution on (010) surfaces near the equilibrium condition of $\sigma = 0.060$. The significant developments are only observed for the large pit steps. The smaller ones are almost stationary (pit 1) in comparison with the large pits, and they make extremely small contributions to the reaction (pit 2). Some of the small pits even disappear from the surface (pit 3) during dissolution. The black lines indicate the displacement directions. The scale of the images is 5 μm. (c) Step displacement rates as a function of size for (201) and (001) steps at undersaturation values of $\sigma = 0.060$ and 0.172, respectively. The lines are plotted according to eq 4.2. A direct relationship between the dissolution rate and the length of the dissolution step is shown at the micron level (the relative undersaturation is defined by $\sigma = 1 - S$ to make it positive in dissolution experiments, pH = 4.50, $I = 0.15$ mol L^{-1}, 37 °C). Reproduced by permission from ref 377. Copyright 2004 from Wiley-VCH.
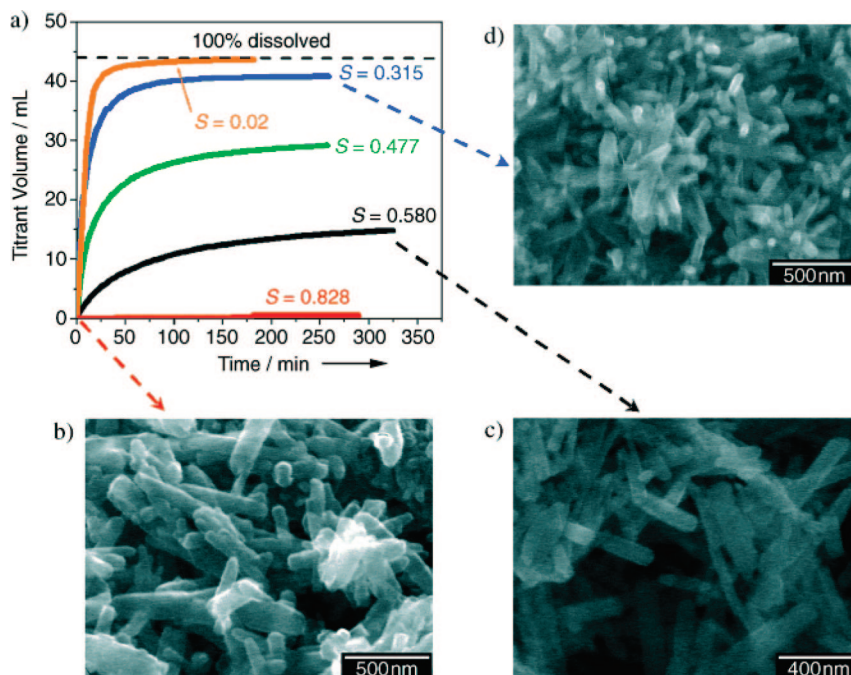
Figure 14. *In vitro* CC dissolution of synthetic HAP. (a) CC plots of titrant volume against time at different undersaturations. The red lines indicate the titrant volumes for full dissolution of the added seeds. Only at very high undersaturation ($S = 0.02$), does the dissolution go to completion. The dissolution rates decrease with time, and eventually, only a fraction of the added seeds undergo dissolution before the rates approach zero. Near equilibrium ($S = 0.828$), no dissolution can be detected in the undersaturated solutions. For the smaller hydroxyapatite seeds (length, 200–300 nm; width, 50–80 nm), no CC dissolution can be detected at an even higher undersaturation of $S \geq 0.720$. This value for enamel is $S \geq 0.4$, showing the much less extensive dissolution. (b) SEM of seed crystals and (c) crystallites remaining at the end of dissolution experiments at $S = 0.580$ and (d) $S = 0.315$. Reprinted with permission from ref 380. Copyright 2004 from Wiley-VCH.

The direct relationship between the sizes of crystallites remaining after dissolution and undersaturations can be studied by precisely controlled CC experiments and by SEM (Figure 14b–d). These confirm that the size decreases with increasing undersaturation. In terms of a 3D macroscale dissolution model for pure HAP, the extent of dissolution and the particle critical sizes can be estimated from the CC kinetics results. From eq 4.5, the ratios of the critical sizes for S of 0.580, 0.477, and 0.315 are 2.11:1.55:1.00, respectively. The results from CC dissolution kinetic experiments, 1.97:1.60:1.00, are in excellent agreement. The data are also supported by scanning electron micrographs (Figure 14b–d), which show that although the initial seed crystals are not uniform in size, the small nanosized dissolution residues (Figure 14d) have similar size distributions (length, 120 ± 20 nm; width, 40 ± 10 nm).

This unexpected dissolution suppression was also observed with the other sparingly soluble calcium phosphates such as β-TCP,[382] OCP,[376] and carbonated apatites.[383] The unusual CC dissolution results of various calcium phosphates are consistent with the microscopic step/pit-based model. When the particle size of dissolving crystals is sufficiently reduced, demineralization is thought to be dynamically stabilized due to the absence of active pits/defects on the very small crystallite surfaces.[141]

4.2. Role of Impurities

Impurities significantly inhibit the dissolution of calcium phosphates. For example, the dissolution kinetics of β-TCP was investigated at 37 °C using the CC method over a range of undersaturation. The rates decreased markedly with time despite the sustained driving force and eventually approached zero, indicating a critical condition in the dissolution process.[382] The calculated reaction order with respect to relative undersaturation, 5.5, suggested a surface-pit (poly-nucleation) mechanism of β-TCP dissolution. The interfacial tension between β-TCP and the solution phase obtained from this model, $\gamma_{SL} = 3.8$ mJ m^{-2}, was consistent with its dissolution mechanism and relatively high solubility. The addition of magnesium or zinc ions retarded β-TCP dissolution, with the latter completely suppressing the reaction at a concentration as low as 2×10^{-6} mol L^{-1}. Peytcheva et al. chose DCPD for dissolution studies due to its related stablility against other structural rearrangements and exhibiting a smooth and even (010) plane suitable for the scanning force microscopy (SFM) observation.[384] In the presence of poly(sodium) aspartate, the SFM height images did not change compared to those in the absence of this additive, suggesting the absence of polymer adsorption onto the crystal surface. This result is in good agreement with equilibrium binding constants for a similar polyaspartate on the related HAP.[270] All interactions of the polymer with the (010) plane are therefore temporary and kinetic. The complexing with carboxylic acid units promoted dissolution along the (201) step. The conversion of DCPD into HAP is completely suppressed during the dissolution process.[384] This polymer can specifically interact with a number of faces or edges, and a highly selective dissolution (site-specific dissolution) is not caused by pH changes. Presumably, the polymer modifier accumulates near the crystal because of partial binding and controls the surface by promoting dissolution of different sites with different selectivities. The proximity of a polymer lowers the interfacial energy of the different crystal surfaces, which gives rise to an altered dissolution behavior.[384] Their results agreed well with the observations of Nancollas et al.,[268] who described effective blocking of
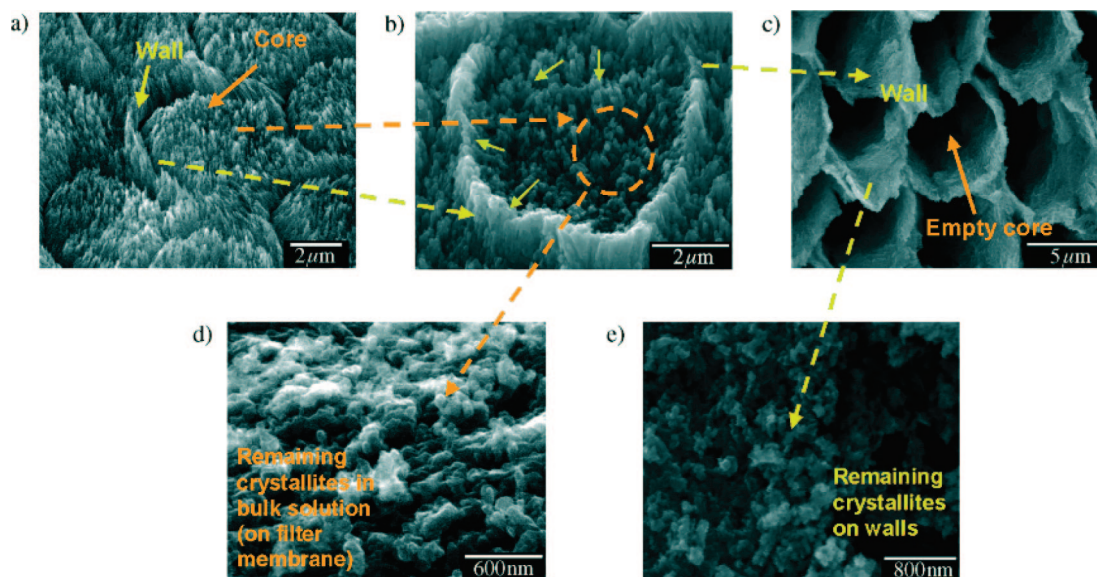
Figure 15. Demineralization of dental enamel: yellow and orange labels mark the dissolution of the walls and cores, respectively, thus showing that they undergo similar dissolution processes. (a) Well-organized rod structures on mature human enamel surfaces: both the walls and cores are composed of numerous needlelike apatites that have the same chemical and physical properties. However, the crystallites in the cores are oriented perpendicular to the enamel surface while those on the walls are inclined by $10-40°$. (b) During dissolution, crystallites become smaller and nanosized apatite particles (shown by green arrows) are formed on both walls and cores. (c) After 7 days of dissolution, the cores are emptied but the walls remain. (d) Nanosized apatite particles collected from the bulk solution by filtration (Nucleopore N003 filter membrane) at the end of dissolution experiment. These particles have escaped from cores and walls but are resistant to further dissolution even though the solution is undersaturated. (e) SEM of the wall at higher magnification; nanosized apatite residues, retained on the wall surfaces, are kinetically protected against further dissolution. Reprinted with permission from ref 380. Copyright 2004 from Wiley-VCH

crystal growth of calcium phosphate in the presence of polyaspartic acids at a surface occupation of 1% of the total crystal area, thus precluding simply a structural explanation.

4.3. Enamel and Bone Demineralization

The new dissolution model of sparingly soluble calcium phosphate salts also applies to the *in vitro* demineralization of biological materials such as tooth enamel.[385,386] Human enamel is an inhomogeneous tissue with an approximately 10% reduction in mineral concentration from the surface to the dentin−enamel junction (DEJ).[387] This anisotropy and inhomogeneity of enamel suggest that the rate of demineralization would depend on the direction and position of the acid attack within a developing lesion.[388] The dissolution rate perpendicular to the enamel rod c-axis decreased as the reaction proceeded from $5.4 \pm 0.5 \times 10^{-11}$ mol mm^{-2} min^{-1}, at 180 min of reaction, to $3.5 \pm 0.5 \times 10^{-11}$ mol mm^{-2} min^{-1}, at 3000 min of dissolution, and the rate of demineralization parallel to the rod c-axis decreased from $4.2 \pm 0.5 \times 10^{-11}$ mol mm^{-2} min^{-1}, at 200 min of reaction, to $3.3 \pm 0.5 \times 10^{-11}$ mol mm^{-2} min^{-1}, at 1800 min of dissolution.[385] These CC results suggest that the inhomogeneity factor does not influence the linearity of the mineral loss with time when the enamel surface is demineralized following the initial removal of the polishing layer. The rates of demineralization in directions perpendicular and parallel to the rod c-axis are both approximately constant with time, with the former being the higher. Other measurements also showed that the rates of demineralization of enamel perpendicular and parallel to the natural surface were both approximately constant with time after an initial sigmoidal period of dissolution.[141]

Demineralization, initiated at core (prism or rod)/wall (prism sheath) interfaces, developed anisotropically along the c-axes (Figure 15a). Dissolution of walls and cores at an

intermediate stage of the dissolution reaction showed apatite nanoparticles $100-200$ nm in size on both cores and walls (Figure 15b). Further dissolution of the nanoparticles was suppressed in CC experiments; those from cores were released directly into the solution by fluid diffusion flux, resulting in empty cores (Figure 15c). After long reaction times (12 weeks), nanosized apatite particles collected from the bulk solution by filtration were kinetically protected against further dissolution even though the solutions remained undersaturated (Figure 15d and e). The CC dissolution curves reached plateaus prior to complete dissolution regardless of whether primary and permanent teeth (Figure 16a and b) were involved. Comparison of CC studies of the demineralization of enamel from primary and permanent teeth showed significant differences. Primary enamel had a greater susceptibility to dissolution during an initial linear stage: $1.5 \pm 0.5 \times 10^{-10}$ mol mm^{-2} min^{-1} compared with $2.6 \pm 0.5 \times 10^{-11}$ mol mm^{-2} min^{-1} for permanent enamel (Figure 16c).[386] CC kinetics also showed inhibition of dissolution of dental enamel following laser irradiation.[389]

Similar nanoparticles were insensitive to demineralization after dissolution of bone in CC studies.[390] The demineralization of anorganic baboon osteonal bone has been investigated at relative undersaturations σ_{HAP} ranging from -0.220 to -0.523 at pH 5.50. Typical titrant−time curves using the nanomolar-sensitive CC technique reached plateaus over an extended experimental period prior to complete dissolution. This indicates the formation of metastable states in which the reaction was effectively suppressed even though the reaction solutions remained undersaturated.[390] Similar reproducible self-inhibited dissolution was observed during CC dissolution of synthetic carbonated apatite (CAP), ruling out the possible influence of complicating biological factors such as the presence of organic matrix components and other impurities. There are two possible sources for the observed
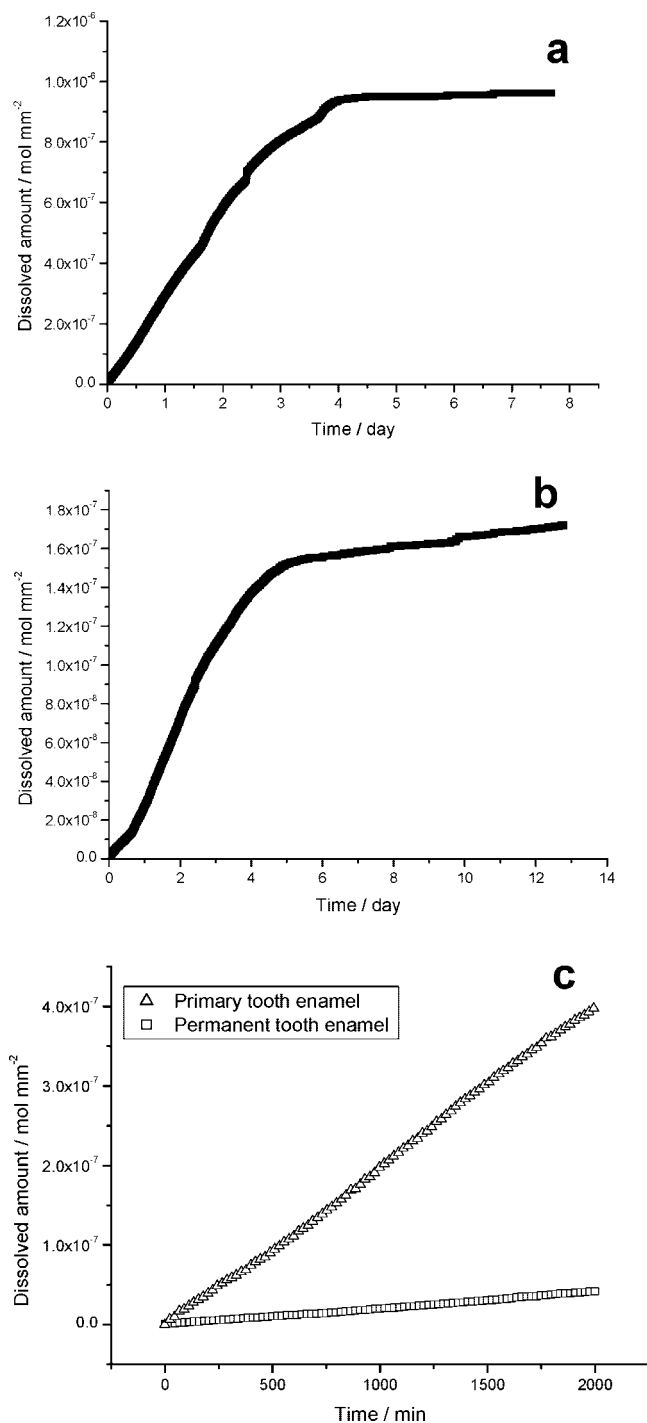
Figure 16. CC curves of (a) primary and (b) permanent tooth enamel dissolution. The rates decreased virtually to zero at the end of dissolution reactions. (c) Comparison of dissolution rates of primary and permanent tooth enamel during the initial linear stages of dissolution. Reproduced by permission from ref 386. Copyright 2006 International and American Association of Dental Research.

nanoparticles following dissolution: (1) They may be present in the initial bone structure and are not products of dissolution, or (2) they are formed as a result of the dissolution of the bone platelet crystals. It is also conceivable that both sources exist.[141] By observing the fracture/nonfracture surfaces of anorganic baboon bone, spherical to cylindrically shaped particles, approximately 20 nm in diameter, are present.[390] These particles were also observed on uncoated anorganic bone specimens, thereby excluding the possibility

that they were coating artifacts or collagenous matrix. In the high resolution back scattered electron image, the spherical particles have a contrast similar to the crystal platelets. They are thus likely to have similar mineral properties. In general, the crystals in bone are plate-shaped with thicknesses of 2−4 nm and have highly variable length and width dimensions. Most are arranged in layers within a collagen matrix.[391,392] This nanoscale structure forms the basic composite material of bone and most probably is responsible for much of its materials properties.[393] Residues of these nanoparticles at the end of dissolution reactions or pre-existing nanoparticles that are stabilized due to the lack of surface defects/pits are able to resist dissolution. This phenomenon of dissolution termination can also be explained by the previously discussed dissolution model, and these very small particles are not arbitrary; rather, the self-tuned and dissolution-insensitive effects for tiny crystallites occur specifically at the nanoscale.

The unexpected presence of spherical to cylindrical shaped nanoparticles in mature bone and their formation during dissolution may, however, have important implications for the dual functions of bone, namely during load bearing and as a reservoir for mineral ions needed for metabolism.[141]

5. Summary and Future Research Directions

5.1. Summary

In order to understand the fundamental processes leading to CaP-based biomineralization, this review focuses on the earliest events of homo/heterogeneous nucleation from an initial supersaturated solution phase and subsequent crystal growth involving various possible precursor phases (amorphous or crystalline) to the final mineral phase by specific templating and the influences of other modulators. Analysis of the effects on crystallization kinetics has abundantly shown the regulation of crystal growth by organic molecules. However, the range of biomineralized structures in nature indicates that their role in nucleation is also crucial. Biominerals often grow in exact locations (cell compartments) within complex crystal composites and exhibit specific crystallographic orientations. Such features can only be determined during the nucleation stage. Indeed, a substantial body of circumstantial evidence suggests that proteins and other organic molecules in a wide range of biomineral structures serve as nucleation "templates", providing preferential sites for nucleation and controlling the orientation of the resulting crystals. We also discuss how the combination of macroscopic constant composition and microscopic atomic force microscopy provides insights into the physical mechanisms of crystal growth and phase stability and the influences of proteins, peptides, or other small molecules. Biodemineralization reactions of tooth enamel and bone may be inhibited or even suppressed when particle sizes fall into certain critical nanoscale levels. This phenomenon actually involves particle size-dependent critical conditions of energetic control at the molecular level. This size is not arbitrary; rather, it appears to give biominerals such as bone and tooth remarkable physical characteristics.

5.2. Future Research Directions

Biological control, either by localizing crystallization or by stabilizing the otherwise short-lived amorphous forms, has been attributed to proteins and their cooperative combinations, peptides and inorganic ions, on the assumption

that each exhibits roughly the same influence in inhibiting the nucleation and growth of crystallites. Although extensive investigations of calcium phosphate crystallization have been performed, many have studied the final structures and morphologies and have not emphasized the need to consider the molecular contacts between mineral and matrix that drive nucleation or the thermodynamic and kinetic controls imposed by matrix and soluble proteins during the nucleation stage. Initial contacts between an organic matrix and mineral nuclei may be crucial for the highly structured mineralization of teeth and bones. Moreover, the presence of soluble proteins in bone and tooth mineral and observations of mineral growth in their presence suggest they act as controling agents over growth rates and morphologies. Current concepts of crystal nucleation and growth at the molecular level, and the role of site-specific interactions in crystallization, provide possible mechanisms of calcium phosphate crystallization that are connected to the mineralization of teeth and bones. It is possible to combine constant composition, in situ AFM, and molecular modeling to investigate the kinetics and energetics of apatite formation on various surfaces including dentin and collagen at realistic driving forces, determine the evolution of phases, identify the sites of nucleation, and define the structural relationships and stereochemical interactions that govern mineral formation on these matrices.

The form of the dependence of nucleation rates at foreign substrates on supersaturation is well-known. The key result is that, by measuring nucleation rates and crystal orientations as a function of supersaturation and modulator concentration, one can test the hypothesis that foreign surfaces promote mineral formation by lowering the interfacial energy for nucleation, quantify the degree of reduction, extract the activation energy for nucleus formation, and define the mechanisms by which soluble proteins mediate the process. Evidence for the importance of interfacial energy has been discussed in this review. This approach has not yet been applied to nucleation on matrix protein surfaces, nor have CC studies allowed an examination of face-specific reductions in interfacial energy or activation barriers or a definition of the molecular contacts between mineral and matrix. Thus, the physical processes by which nucleation control is established and the thermodynamic and kinetic parameters that define those processes remain largely unknown. In nearly all of the studies of crystal nucleation on various templates, the observed final crystal phase and orientation were assumed to define the structural state of the crystal nucleus. This view may fail to capture the complex dynamics and features such as an initial amorphous phase preceding the final, well-ordered product. Since the number of potential metastable phases in the calcium phosphate system is larger than that for the others, such as calcium carbonate, which is now known to have a metastable amorphous phase, it seems prudent to start with the hypothesis that different structural relationships and phases may be seen in the early stages of nucleation without being present in the final product. These considerations seem to dictate that four critical questions about calcium phosphate formation on organic matrix proteins need to be addressed: (1) What is the structural relationship between matrix and mineral during the nucleation stage of mineral formation? (2) Which pathway through the potential cascade of metastable phases does the system follow in going from the solvated state to the final HAP? (3) What are the interfacial energies and kinetic barriers

associated with these processes? (4) What are the roles of proteins in solution in modulating nucleation?

The sensitivity of the CC and Dual CC techniques offer unique opportunities for investigating the simultaneous de- and remineralization of multiple calcium phosphate phases at both synthetic and natural apatite surfaces, thereby providing information about the very earliest nucleation events. Moreover, CC crystallization studies provide strong experimental evidence to support the concept that it is necessary to carefully select the driving forces (supersaturations) for future *in vitro* biomimetic mineralization studies. Nucleation and growth may follow different mechanisms across the continuum of driving force.

As a complementary method for studying the fast nucleation/growth kinetics in solution, the addition of small/wide-angle X-ray scattering (SAXS/WAXS) to future investigative approaches to induction periods is of especial significance, since early nucleation events during induction periods have been previously inaccessible to direct analysis. Based on much evidence for the existence of amorphous phases and subsequent phase transformation in biominerals, related studies have been conducted in solution[394−396] or on LB film[397] using SAXS/WAXS. This technique provides a very useful tool for analyzing in detail the specific influence of additive molecules on these processes, particularly in the early stages of mineralization.

In the light of the foregoing discussions on the cluster growth model (section 3.3.2), it is appropriate to ask the following:(1) By what sequence of events does a biomineral form at the earliest developing stages? (2) Are individual atoms or molecules added as crystals grow on organic template surfaces? Some interesting evidence has already suggested that inorganic nanocrystals (1−10 nm), made up of hundreds or even thousands of atoms, can form fundamental building blocks for highly ordered and complex natural minerals through nanocrystal aggregation. It has also been suggested that mesoscale assembly and cooperative interactions between the forming nanocrystals and assembling proteins are pivotal to biomineralization processes.[141,398−401] A certain density of defects is inevitable even at equilibrium. However, when this same number of atoms is partitioned into nanometer-sized crystals, then, on average, each nanocrystal need not contain any interior defects.[141,402] Nanoparticles without active pits/defects on their surfaces are thus stabilized to resist further dissolution. Moreover, by way of oriented aggregation, the surface energy is reduced substantially because the interface is eliminated.[403,404] During this process, in addition to lowering the nucleation barrier, organic templates will reduce random Brownian motion-driven nanoparticle collisions and may allow adjacent particles to rotate to find the low-energy configuration.[141,405] The incorporation of other smaller impurity species may also be facilitated under conditions where crystals grow by nanocrystal attachment.[402] Furthermore, phase stability can be particle size-dependent because phase transformation and recrystallization are promoted by particle aggregation if the initial particles are metastable.[141,406,407]

Despite their complex hierarchical structure, the basic building blocks of teeth and bones are nanosized mineral particles, both during initial formation and at later stages. The CC kinetics analysis has shown that demineralization reactions of tooth enamel and bone may be inhibited or even effectively suppressed when particle sizes fall to a critical nanoscale level. Dissolution resistance results from critical

conditions of size-dependent energetic control at the molecular level. Nanostructured biominerals can remain relatively stable, despite undersaturation. This dissolution termination is clearly kinetic and does not result from surface modification by additives. Technical aspects (sample preparation) preclude valid independent characterization of these undissolved nanoparticles as crystalline or amorphous by techniques such as TEM and require approaches such as time-resolved SAXS/WAXS to determine particle size and density, as well as the crystalline/amorphous phase of these residual nanosized particles, both after long-term suspension in an undersaturated solution or after very short CC dissolution reactions. In addition to the velocity of dissolution steps on pits formed on enamel and bone crystal surfaces, the morphology and size of residual undissolved particles should be determined as a function of undersaturation using in situ AFM. Comparison of the microstructures of bulk enamel and bone crystals by SAXS/WAXS and AFM will aid understanding of how nanosized particles may contribute to the remarkable mechanical and dynamic stabilizations of enamel and bone in fluctuating physiological milieux.

6. Abbreviations

ACP	amorphous calcium phosphate
AFM	atomic force microscopy
Amel	amelogenin
BCF	Burton−Cabrera−Frank model
BSA	bovine serum albumin
CaP	calcium phosphate
CAP	carbonated apatite
CC	constant composition
CNT	classical nucleation theory
C−V	Cabrera−Vermilyea model
DCC	dual constant composition
DCPD	dicalcium phosphate dihydrate
DEJ	dentin−enamel junction
DMP1	dentin matrix protein
ECM	extracellular matrix
EXAFS	extended X-ray absorption fine structure
f.c.c.	face-centered cubic
FGF	fibroblast growth factor
Fib	fibrinogen
FMC	flow microcalorimeter
G−T	Gibbs−Thomson effect
HAP	hydroxyapatite
h.c.p.	hexagonal close packed
IAP	ion activity product
IOL	intraocular lens
LB	Langmuir−Blodgett
LRAP	leucine-rich Amel protein
LSZ	lysozyme
LW	Lifshitz−van der Waals
MGB	myoglobin
MSC	multistep crystallization
OCP	octacalcium phosphate
OPN	osteopontein
PAA	polyaspartic acid
PC	Posner's clusters
PEs	polyelectrolytes
PGA	poly-L-glutamic acid
PLAA	poly-L-aspartic acid
PLL	poly-L-lysine
pOC	porcine osteocalcin
PPn	phosphophoryn
PRP1	proline-rich acidic salivary protein
PSS	polystyrene sulfonate
r.h.c.p.	random-hexagonal close-packed
SAMs	self-assembled monolayers

SAXS/WAXS	small angle/wide-angle X-ray scattering
SFM	scanning force microscopy
SLS	static light scattering
SN-15	statherin *N*-terminal 15 amino acids
TCP	tricalcium phosphate
TLW	thin layer wicking
TSC	two-step crystallization

7. Acknowledgments

8. References

(1) Dorozhkin, S. V. *J. Mater. Sci.* **2007**, *42*, 1061.
(2) Koutsoukos, P. G.; Amjad, Z.; Tomson, M. B.; Nancollas, G. H. *J. Am. Chem. Soc.* **1980**, *102*, 1553.
(3) Johnsson, M. S. A.; Nancollas, G. H. *Crit. Rev. Oral Biol. Med.* **1992**, *3*, 61.
(4) Dorozhkin, S. V.; Epple, M. *Angew. Chem., Int. Ed.* **2002**, *41*, 3130.
(5) Elliot, J. C. *Structure and Chemistry of the Apatites and Other Calcium Orthosphosphates*; Elsevier: Amsterdam, 1994.
(6) Orme, C. A.; Giocondi, J. L. Unpublished material.
(7) Eanes, E. D.; Gillessen, H.; Posner, A. S. *Nature* **1965**, *208*, 365.
(8) Bienenstock, A.; Posner, A. S. *Arch. Biochem. Biophys.* **1968**, *124*, 604.
(9) Posner, A. S.; Betts, F. *Acc. Chem. Res.* **1975**, *8*, 273.
(10) Treboux, G.; Layrolle, P.; Kanzaki, N.; Onuma, K.; Ito, A. *J. Phys. Chem. A* **2000**, *104*, 5111.
(11) Treboux, G.; Layrolle, P.; Kanzaki, N.; Onuma, K.; Ito, A. *J. Am. Chem. Soc.* **2000**, *122*, 8323.
(12) Onuma, K.; Ito, A. *Chem. Mater.* **1998**, *10*, 3346.
(13) Kanzaki, N.; Treboux, G.; Onuma, K.; Tsutsumi, S.; Ito, A. *Biomaterials* **2001**, *22*, 2921.
(14) Christoffersen, J.; Christoffersen, M. R.; Kibalczyc, W.; Andersen, A. *J. Cryst. Growth* **1989**, *94*, 767.
(15) Christoffersen, J.; Christoffersen, M. R.; Kibalczyc, W. *J. Cryst. Growth* **1990**, *106*, 349.
(16) Betts, F.; Posner, A. S. *Trans. Am. Crystallogr. Assoc.* **1974**, *10*, 13.
(17) Tropp, J.; Blumenthal, N. C.; Waugh, J. S. *J. Am. Chem. Soc.* **1983**, *105*, 22.
(18) Harries, J. E.; Hukins, D. W. L.; Hasnain, S. S. *J. Phys. C* **1986**, *19*, 6859.
(19) Harries, J. E.; Hukins, D. W. L.; Holt, C.; Hasnain, S. S. *J. Cryst. Growth* **1987**, *84*, 563.
(20) Peters, F.; Schwarz, K.; Epple, M. *Thermochim. Acta* **2000**, *361*, 131.
(21) Termine, J. D.; Peckauskas, R. A.; Posner, A. S. *Arch. Biochem. Biophys.* **1970**, *140*, 318.
(22) Boskey, A. L.; Posner, A. S. *J. Phys. Chem.* **1973**, *77*, 2313.
(23) Yin, X.; Stott, M. J. *J. Chem. Phys.* **2003**, *118*, 3717.
(24) Tadic, D.; Peters, F.; Epple, M. *Biomaterials* **2002**, *23*, 2553.
(25) Young, R. A.; Brown, W. E. In *Biological Mineralization and Demineralization*; Nancollas, G. H., Ed.; Springer-Verlag: Berlin, 1982; p 101.
(26) LeGeros, R. Z. In *Hydroxyapatite and Related Materials*; Brown, P. W., Constantz, B., Eds.; CRC: Boca Raton, FL, 1994; p 3.
(27) Arsic, J.; Kaminski, D.; Poodt, P.; Vlieg, E. *Phys. Rev. B* **2004**, *69*, 245406.
(28) Boistell, R.; Lopez-Valero, I. *J. Cryst. Growth* **1990**, *102*, 609.
(29) Abbona, F.; Madsen, H. E. L.; Boistelle, R. *J. Cryst. Growth* **1986**, *74*, 581.
(30) Nancollas, G. H. In *Biological Mineralization and Demineralization*; Nancollas, G. H., Ed.; Springer-Verlag: Berlin, 1982; p 79.
(31) Dickens, B.; Schroeder, L. W.; Brown, W. E. *J. Solid State Chem.* **1974**, *10*, 232.
(32) de Aza, P. N.; Santos, C.; Pazo, A.; de Aza, S.; Cusco, R.; Artus, L. *Chem. Mater.* **1997**, *9*, 912.
(33) de Aza, P. N.; Guitian, F.; Santos, C.; de Aza, S.; Cusco, R.; Artus, L. *Chem. Mater.* **1997**, *9*, 916.
(34) Obadia, L.; Deniard, P.; Alonso, B.; Rouillon, T.; Jobic, S.; Guicheux, J.; Julien, M.; Massiot, D.; Bujoli, B.; Bouler, J. M. *Chem. Mater.* **2006**, *18*, 1425.
(35) Cheng, P. T.; Grabher, J.; LeGeros, R. Z. *Magnesium* **1988**, *7*, 123.
(36) Brown, W. E. *Nature* **1962**, *196*, 1048.
(37) Brown, W. E.; Smith, J. P.; Lehr, J. R.; Frazier, A. W. *Nature* **1962**, *196*, 1049.
(38) Brown, W. E.; Eidelman, N.; Tomzaic, B. B. *Adv. Dent. Res.* **1987**, *1*, 306.
(39) Taves, D. R. *Nature* **1963**, *200*, 1312.

(40) Terpstra, R. A.; Bennema, P. *J. Cryst. Growth* **1987**, *82*, 416.

(41) Mathew, M.; Brown, W. E.; Schroeder, L. W.; Dickens, B. *J. Cryst. Spectrosc. Res.* **1988**, *18*, 235.

(42) Iijima, M.; Nelson, D. G. A.; Pan, Y.; Kreinbrink, A. T.; Adachi, M.; Goto, T.; Moriwaki, Y. *Calcif. Tissue Int.* **1996**, *59*, 377.

(43) Aoba, T.; Komatsu, H.; Shimazu, Y.; Yagishita, H.; Taya, Y. *Connect. Tissue Res.* **1998**, *38*, 129.

(44) Tseng, Y. H.; Mou, C. Y.; Chan, J. C. C. *J. Am. Chem. Soc.* **2006**, *128*, 6909.

(45) Brown, W. E.; Schroeder, L. W.; Ferris, J. S. *J. Phys. Chem.* **1979**, *83*, 1385.

(46) Pieters, I. Y.; De Maeyer, E. A. P.; Verbeeck, R. M. H. *Inorg. Chem.* **1996**, *35*, 5791.

(47) Fowler, B. O.; Markovic, M.; Brown, W. E. *Chem. Mater.* **1993**, *5*, 1417.

(48) Posner, A. S.; Perloff, A.; Diorio, A. F. *Acta Crystallogr.* **1958**, *11*, 308.

(49) Kay, M. I.; Young, R. A.; Posner, A. S. *Nature* **1964**, *204*, 1050.

(50) Onuma, K.; Ito, A.; Tateishi, T.; Kameyama, T. *J. Cryst. Growth* **1995**, *148*, 201.

(51) Rodriguez-Lorenzo, L. M.; Vallet-Regi, M. *Chem. Mater.* **2000**, *12*, 2460.

(52) Jäger, C.; Welzel, T.; Meyer-Zaika, W.; Epple, M. *Magn. Reson. Chem.* **2006**, *44*, 573.

(53) Brown, P. W.; Martin, R. I. *J. Phys. Chem. B* **1999**, *103*, 1671.

(54) Lynn, A. K.; Bonfield, W. *Acc. Chem. Res.* **2005**, *38*, 202.

(55) Kikuchi, M.; Itoh, S.; Ichinose, S.; Shinomiya, K.; Tanaka, J. *Biomaterials* **2001**, *22*, 1705.

(56) Boskey, A. L; Posner, A. S. *J. Phys. Chem.* **1976**, *80*, 40.

(57) Tung, M. S.; Brown, W. E. *Calcif. Tissue Int.* **1983**, *35*, 783.

(58) Boskey, A. L.; Posner, A. S. *Mater. Res. Bull.* **1974**, *9*, 907.

(59) Eanes, E. D.; Posner, A. S *Trans. N. Y. Acad. Sci.* **1965**, *28*, 233.

(60) Eanes, E. D.; Posner, A. S. *Mater. Res. Bull.* **1970**, *5*, 377.

(61) Heughebaert, J. C.; Montel, G. *Calcif. Tissue Int.* **1984**, *34*, 104.

(62) Hochrein, O.; Kniep, R.; Zahn, D. *Chem. Mater.* **2005**, *17*, 1978.

(63) Termine, J. D.; Eanes, E. D. *Calcif. Tissue Res.* **1972**, *10*, 171.

(64) Termine, J. D.; Posner, A. S. *Arch. Biochem. Biophys.* **1970**, *140*, 307.

(65) Eanes, E. D.; Meyer, J. L. *Calcif. Tissue Res.* **1977**, *23*, 259.

(66) Feenstra, T. P.; de Bruyn, P. L. *J. Phys. Chem.* **1979**, *83*, 475.

(67) Harries, J. E.; Hasnain, S. S.; Shan, J. S. *Calcif. Tissue Int.* **1987**, *41*, 346.

(68) Abbona, F.; Baronnet, A. *J. Cryst. Growth* **1996**, *165*, 98.

(69) Harper, R. A.; Posner, A. S. *Proc. Soc. Exp. Biol. Med.* **1966**, *122*, 137.

(70) Termine, J. D.; Posner, A. S. *Calcif. Tissue Res.* **1967**, *1*, 8.

(71) Glimcher, M. J.; Bonar, L. C.; Grynpas, M. D.; Landis, W. J.; Roufosse, A. H. *J. Cryst. Growth* **1981**, *53*, 100.

(72) Kazanci, M.; Fratzl, P.; Klaushofer, K.; Paschalis, E. P. *Calcif. Tissue Int.* **2006**, *79*, 354.

(73) Kim, S.; Ryu, H. S.; Shin, H.; Jung, H. S.; Hong, K. S. *Mater. Chem. Phys.* **2005**, *91*, 500.

(74) Tamai, M.; Isshiki, T.; Nishio, K.; Nakamura, M.; Nakahira, A.; Endoh, H. *J. Mater. Res.* **2003**, *18*, 2633.

(75) Blumenthal, N. C.; Betts, F.; Posner, A. S. *Calcif. Tissue Res.* **1977**, *23*, 245.

(76) Blumenthal, N. C.; Betts, F.; Posner, A. S. *Calcif. Tissue Int.* **1981**, *33*, 111.

(77) Miller, J. D.; Randolph, A. D.; Drach, G. W. *J. Urol.* **1977**, *117*, 342.

(78) Nelson, D. G. A.; McLean, J. D. *Calcif. Tissue Int.* **1984**, *36*, 219.

(79) Nelson, D. G. A.; Wood, D. J.; Barry, J. C.; Featherston, J. D. B. *Ultramicroscopy* **1986**, *19*, 253.

(80) Daculsi, G.; LeGeros, R. Z.; Mitre, D. *Calcif. Tissue Int.* **1989**, *45*, 95.

(81) Daculsi, G.; LeGeros, R. Z.; Heughebaert, M.; Barbieux, I. *Calcif. Tissue Int.* **1990**, *46*, 20.

(82) Landis, W. J.; Glimcher, M. J. *J. Ultrastruct. Res.* **1979**, *63*, 188.

(83) Koutsoukos, P. G.; Nancollas, G. H. *J. Cryst. Growth* **1981**, *53*, 10.

(84) Kanzaki, N.; Onuma, K.; Treboux, G.; Ito, A. *J. Cryst. Growth* **2002**, *235*, 465.

(85) van Kemenade, M. J.; deBruyn, P. L. *J. Colloid Interface Sci.* **1987**, *118*, 564.

(86) Ostwald, W. F. *Z. Phys. Chem.* **1897**, *22*, 289.

(87) Sohnel, O. *J. Cryst. Growth* **1982**, *57*, 101.

(88) Heughebaert, J. C.; Zawacki, S. J.; Nancollas, G. H. *J. Colloid Interface Sci.* **1990**, *135*, 20.

(89) Onuma, K. *Prog. Cryst. Growth Charact. Mater.* **2006**, *52*, 223.

(90) Onuma, K.; Oyane, A.; Tsutsui, K.; Tanaka, K.; Treboux, G.; Kanzaki, N.; Ito, A. *J. Phys. Chem. B* **2000**, *104*, 10563.

(91) Onuma, K. *J. Phys. Chem. B.* **2005**, *109*, 8257.

(92) Lévêque, L.; Cusack, M.; Davis, S. A.; Mann, S. *Angew. Chem., Int. Ed.* **2004**, *43*, 885.

(93) Bigi, A.; Falini, G.; Foresti, E.; Gazzaro, M.; Ripamonti, A.; Roveri, N. *J. Inorg. Biochem.* **1993**, *49*, 69.

(94) Guerra-López, J.; González, R.; Gómez, A.; Pomés, R.; Punte, G.; Della Védova, C. O. *J. Solid State Chem.* **2000**, *151*, 163.

(95) Tsortos, A.; Nancollas, G. H. *J. Colloid Interface Sci.* **2002**, *250*, 159.

(96) Amjad, Z. *Langmuir* **1987**, *3*, 1063.

(97) Despotovic, R.; Filipovic-Vincekovic, N.; Furedi-Milhofer, H. *Calcif. Tissue Res.* **1975**, *11*, 13.

(98) Gajjeraman, S.; Narayanan, K.; Hao, J. J.; Qin, C. L.; George, A. *J. Biol. Chem.* **2007**, *282*, 1193.

(99) Areva, S.; Peltola, T.; Sailynoja, E.; Laajalehto, K.; Linden, M.; Rosenholm, J. B. *Chem. Mater.* **2002**, *14*, 1614.

(100) Bar-Yosef Ofir, P.; Govrin-Lippman, R.; Garti, N.; Füredi-Milhofer, H. *Cryst. Growth Des.* **2004**, *4*, 177.

(101) Peytcheva, A.; Cölfen, H.; Schnablegger, H.; Antonietti, M. *Colloid Polym. Sci.* **2002**, *280*, 218.

(102) Lin, J.; Raghavan, S.; Fuerstenau, D. W. *Colloids Surf.* **1981**, *3*, 357.

(103) Caslavska, V.; Moreno, E. C.; Brudevold, F. *Arch. Oral Biol.* **1975**, *20*, 333.

(104) Menzel, B.; Amberg, C. H. *J. Colloid Interface Sci.* **1972**, *38*, 256.

(105) Baud, C. A.; Bang, S. *Caries Res.* **1970**, *4*, 1.

(106) Yesinowski, J. P.; Mobley, M. J. *J. Am. Chem. Soc.* **1983**, *105*, 6191.

(107) de Leeuw, N. H. *Phys. Chem. Chem. Phys.* **2002**, *4*, 3865.

(108) de Leeuw, N. H. *J. Phys. Chem. B* **2004**, *108*, 1809.

(109) de Leeuw, N. H. *Phys. Chem. Chem. Phys.* **2004**, *6*, 1860.

(110) LeGeros, R. Z. *Nature* **1965**, *206*, 403.

(111) LeGeros, R. Z.; Daculsi, G.; Orly, I.; Abergas, T.; Torres, W. *SEM* **1989**, *3*, 129.

(112) Kannan, S.; Ferreira, J. M. F. *Chem. Mater.* **2006**, *18*, 198.

(113) de Leeuw, N. H.; Bowe, J. R.; Rabone, J. A. L. *Faraday Discuss.* **2007**, *134*, 195.

(114) Peroos, S.; Du, Z. M.; de Leeuw, N. H. *Biomaterials* **2006**, *27*, 2150.

(115) Astala, R.; Stott, M. J. *Chem. Mater.* **2005**, *17*, 4125.

(116) Cheng, Z. H.; Yasukawa, A.; Kandori, K.; Ishikawa, T. *Langmuir* **1998**, *14*, 6681.

(117) Salimi, M. H.; Heughebaert, J. C.; Nancollas, G. H. *Langmuir* **1985**, *1*, 119.

(118) Holt, C.; van Kemenade, M. J. J. M.; Harries, J. E.; Nelson, L. S.; Bailey, R. T.; Hukins, D. W. L.; Hasnaian, S. S.; De Bruyn, P. L. *J. Cryst. Growth* **1988**, *92*, 239.

(119) Holt, C.; van Kemenade, M. J. J. M.; Nelson, L. S.; Hukins, D. W. L.; Bailey, R. T.; Harries, J. E.; Hasnaian, S. S.; De Bruyn, P. L. *Mater. Res. Bull.* **1989**, *23*, 55.

(120) Amelinckx, S. *Nature* **1952**, *170*, 760.

(121) Amelinckx, S. *Nature* **1952**, *169*, 841.

(122) Nassif, N.; Pinna, N.; Gehrke, N.; Antonietti, M.; Jager, C.; Cölfen, H. *Proc. Natl. Acad. Sci., U. S. A.* **2005**, *102*, 12653.

(123) Nudelman, F.; Chen, H. H.; Goldberg, H. A.; Weiner, S.; Addadi, L. *Faraday Discuss.* **2007**, *136*, 9.

(124) Sunagawa, I. In *Advances in Crystal Growth*; Furukawa, Y., Nakajima, K., Sato, K., Eds.; Elsevier: Amsterdam, 2001; p 1.

(125) Kashchiev, D. *Nucleation: Basic Theory with Applications*; Butterworth-Heinemann: Oxford, 2000.

(126) Chernov, A. A. *Modern Crystallography III—Crystal Growth*; Springer: Berlin, 1984.

(127) Laaksonen, A.; Talanquer, V.; Oxtoby, D. W. *Annu. Rev. Phys. Chem.* **1995**, *46*, 489.

(128) Trau, M.; Saville, D. A.; Aksay, I. A. *Science* **1996**, *272*, 706.

(129) Larsen, A. E.; Grier, D. G. *Nature* **1997**, *385*, 230.

(130) Yethiraj, A.; van Blaaderen, A. *Nature* **2003**, *421*, 513.

(131) Gasser, U.; Weeks, E. R.; Schofield, A.; Pusey, P. N.; Weitz, D. A. *Science* **2001**, *292*, 258.

(132) Zhang, K. Q.; Liu, X. Y. *Nature* **2004**, *429*, 739.

(133) Auer, S.; Frenkel, D. *Nature* **2001**, *409*, 1020.

(134) Auer, S.; Frenkel, D. *Nature* **2001**, *413*, 711.

(135) Cacciuto, A.; Auer, S.; Frenkel, D. *Nature* **2004**, *428*, 404.

(136) Sear, R. P. *J. Phys. Chem. B* **2006**, *110*, 4985.

(137) Teng, H. H.; Dove, P. M.; Orme, C. A.; de Yoreo, J. J. *Science* **1998**, *282*, 724.

(138) Macpherson, J. V.; Unwin, P. R.; Hillier, A. C.; Bard, A. J. *J. Am. Chem. Soc.* **1996**, *118*, 6445.

(139) Piana, S.; Reyhani, M.; Gale, J. D. *Nature* **2005**, *438*, 70.

(140) Liu, X. Y. *J. Chem. Phys.* **2000**, *113*, 8807.

(141) Wang, L. J.; Nancollas, G. H. In *Biomineralization. From Nature to Application; Vol. 4. of Metal Ions in Life Sciences*; Sigel, A., Sigel, H., Sigel, R. K. O., Eds.; John Wiley & Sons: Chichester, 2008; p 413.

(142) Liu, X. Y. *J. Chem. Phys.* **2000**, *112*, 9949.

(143) Davey, R. J. *Nature* **2004**, *428*, 374.

(144) Guan, X.; Tang, R.; Nancollas, G. H. *J. Biomed. Mater. Res. A* **2004**, *71A*, 488.

(145) Wu, W.; Guan, X.; Tang, R.; Hook, D.; Yan, W.; Grobe, G.; Nancollas, G. H. *Langmuir* **2004**, *20*, 1356.
(146) Gibbs, J. W. *Collected works, Vol. 1 of Thermodynamics*; Longmans and Green: New York, 1928.
(147) ten Wolde, P. R.; Frenkel, D. *Science* **1997**, *277*, 1975.
(148) Addadi, L.; Weiner, S. *Angew. Chem., Int. Ed. Engl.* **1992**, *31*, 153.
(149) Lutsko, J. F.; Nicolis, G. *Phys. Rev. Lett.* **2006**, *96*, 046102.
(150) Chen, X.; Samia, A. C. S.; Lou, Y.; Burda, C. *J. Am. Chem. Soc.* **2005**, *127*, 4372.
(151) Zhang, T. H.; Liu, X. Y. *J. Am. Chem. Soc.* **2007**, *129*, 13520.
(152) Chughtai, A.; Marshall, R.; Nancollas, G. H. *J. Phys. Chem.* **1968**, *72*, 208.
(153) Davies, C. W. *Ion Association*; Butterworth: London, 1962.
(154) Liu, X. Y. In *From Solid-fluid Interface to Nanostructure Engineering, Vol. II*; Liu, X. Y., De Yoreo, J. J., Eds.; Plenum-Kluwer: New York, 2004.
(155) Mullin, J. W. *Crystallization*, 4th ed.; Butterworth-Heinemann: Oxford, 2001; p 130.
(156) Kelton, K. F. In *Solid State Physics Vol. 45*; Ehrenreich, H., Turnbull, D., Eds.; Academic: New York, 1991; p 75.
(157) Weiner, S.; Sagi, I.; Addadi, L. *Science* **2005**, *309*, 1027.
(158) Towe, K. M.; Lowenstam, H. A. *J. Ultrastruct. Res.* **1967**, *17*, 1.
(159) Lowenstam, H. A.; Weiner, S. *Science* **1985**, *227*, 51.
(160) De Yoreo, J. J.; Vekilov, P. G. In *Biomineralization, Vol. 54 of Review of Mineralogical Society of America Geochemical Society*; Dove, P. M., De Yoreo, J. J., Weiner, S., Eds.; American Geochemical Society: Washington, DC, 2003; p 57.
(161) Anderson, V. J.; Lekkerkerker, H. N. W. *Nature* **2002**, *416*, 811.
(162) Yau, S. T.; Vekilov, P. G. *Nature* **2000**, *406*, 494.
(163) Oxtoby, D. W. *Nature* **2000**, *406*, 464.
(164) Liu, X. Y. *Langmuir* **2000**, *16*, 7337.
(165) Liu, X. Y.; Lim, S. W. *J. Am. Chem. Soc.* **2003**, *125*, 888.
(166) Liu, X. Y. In *Advances in Crystal Growth Research*; Furukawa, Y., Nakajima, K., Sato, K., Eds.; Elsevier: Amsterdam, 2001; p 42.
(167) Jiang, H.; Liu, X. Y. *J. Biol. Chem.* **2004**, *279*, 41286.
(168) Jiang, H.; Liu, X. Y.; Zhang, G.; Li, Y. *J. Biol. Chem.* **2005**, *280*, 42061.
(169) Wang, L. J.; Guan, X. Y.; Du, C.; Moradian-Oldak, J.; Nancollas, G. H. *J. Phys. Chem. C* **2007**, *111*, 6398.
(170) Wang, L. J.; Guan, X. Y.; Yin, H. Y.; Moradian-Oldak, J.; Nancollas, G. H. *J. Phys. Chem. C* **2008**, *112*, 5892.
(171) Moradian-Oldak, J.; Simmer, J. P.; Lau, E. C.; Sarte, P. E.; Slavkin, H. C.; Fincham, A. G. *Biopolymers* **1994**, *34*, 1339.
(172) Shaw, W. J.; Campbell, A. A.; Paine, M. L.; Snead, M. L. *J. Biol. Chem.* **2004**, *279*, 40263.
(173) Chen, X.; Wang, Q.; Shen, J. W.; Pan, H. H.; Wu, T. *J. Phys. Chem. C* **2007**, *111*, 1284.
(174) Lau, E. C.; Mohandas, T. K.; Shapiro, L. J.; Slavkin, H. C.; Snead, M. L. *Genomics* **1989**, *4*, 162.
(175) Gergely, C.; Szalontai, B.; Moradian-Oldak, J.; Cuisinier, F. J. G. *Biomacromolecules* **2007**, *8*, 2228.
(176) Baniash, E.; Simmer, J. P.; Margolis, H. C. *J. Struct. Biol.* **2005**, *149*, 182.
(177) Yin, Y.; Alivisatos, A. P. *Nature* **2005**, *437*, 664.
(178) Iijima, M.; Moriwaki, Y.; Wen, H. B.; Fincham, A. G.; Moradian-Oldak, J. *J. Dent. Res.* **2002**, *81*, 69.
(179) Robinson, C.; Fuchs, P.; Weatherell, J. A. *J. Cryst. Growth* **1981**, *53*, 160.
(180) Robinson, C.; Connell, S.; Kirkham, J.; Shore, R.; Smith, A. *J. Mater. Chem.* **2004**, *14*, 2242.
(181) Travis, D. F.; Glimcher, M. J. *J. Cell Biol.* **1964**, *23*, 447.
(182) Tarasevich, B. J.; Howard, C. J.; Larson, J. L.; Snead, M. L.; Simmer, J. P.; Paine, M.; Shaw, W. J. *J. Cryst. Growth* **2007**, *304*, 407.
(183) Söhnel, O.; Mullin, J. W. *J. Colloid Interface Sci.* **1988**, *123*, 43.
(184) Rodriguez-Clemente, R.; Lopez-Macipe, A.; Gomez-Morales, J.; Torrent-Burgues, J.; Castano, V. M. *J. Euro. Ceram. Soc.* **1998**, *18*, 1351.
(185) Landau, E. M.; Levanon, M.; Leiserowitz, L.; Lahav, M.; Sagiv, J. *Nature* **1985**, *318*, 353.
(186) Landau, E. M.; Grayer, W. S.; Levanon, M.; Leiserowitz, L.; Lahav, M.; Sagiv, J. *J. Am. Chem. Soc.* **1989**, *111*, 1436.
(187) Mann, S.; Heywood, B. R.; Rajam, S.; Walker, J. B. A.; Davey, R. J.; Birchall, J. D. *Adv. Mater.* **1990**, *2*, 257.
(188) Heywood, B. R.; Mann, S. *Adv. Mater.* **1994**, *6*, 9.
(189) Lu, H. B.; Ma, C. L.; Cui, H.; Zhou, L. F.; Wang, R. Z.; Cui, F. Z. *J. Cryst. Growth* **1995**, *155*, 120.
(190) Ma, C. L.; Lu, H. B.; Wang, R. Z.; Zhou, L. F.; Cui, F. Z.; Qian, F. *J. Cryst. Growth* **1997**, *173*, 141.
(191) Xu, G. F.; Aksay, I. A.; Groves, J. T. *J. Am. Chem. Soc.* **2001**, *123*, 2196.
(192) Zhang, L. J.; Liu, H. G.; Feng, X. S.; Zhang, R. J.; Zhang, L.; Mu, Y. D.; Hao, J. C.; Qian, D. J.; Lou, Y. F. *Langmuir* **2004**, *20*, 2243.

(193) Tarasevich, B. J.; Chusuei, C. C.; Allara, D. L. *J. Phys. Chem. B* **2003**, *107*, 10367.
(194) Onuma, K.; Oyane, A.; Kokubo, T.; Treboux, G.; Kanzaki, N.; Ito, A. *J. Phys. Chem. B* **2000**, *104*, 11950.
(195) Zhang, J.; Kirkham, J.; Wallwork, M. L.; Smith, D. A.; Brookes, S. J.; Shore, R. C.; Wood, S. R.; Robinson, C. *Langmuir* **1999**, *15*, 8178.
(196) Zhu, P.; Masuda, Y.; Koumoto, K. *Biomaterials* **2004**, *17*, 3915.
(197) Pecheva, E.; Pramatarova, L.; Altankov, G. *Langmuir* **2007**, *23*, 9386.
(198) Kanzaki, N.; Onuma, K.; Treboux, G.; Tsutsumi, S.; Ito, A. *J. Phys. Chem. B* **2001**, *105*, 1991.
(199) Kanzaki, N.; Onuma, K.; Treboux, G.; Tsutsumi, S.; Ito, A. *J. Phys. Chem. B* **2000**, *104*, 4189.
(200) Liu, X. Y.; Maiwa, K.; Tsukamoto, K. *J. Chem. Phys.* **1997**, *106*, 1870.
(201) Malkin, A. J.; Kuznetsov, Yu. G.; Glantz, W.; Mcpherson, A. *J. Cryst. Growth* **1996**, *100*, 11736.
(202) Sohnel, O.; Mullin, J. W. *J. Cryst. Growth* **1978**, *44*, 377.
(203) Nancollas, G. H.; Koutsoukos, P. G. *Prog. Cryst. Growth Charact. Mater.* **1980**, *3*, 77.
(204) Moreno, E. C.; Zahradnik, R. T.; Glazman, A.; Hwu, R. *Calcif. Tissue Res.* **1977**, *24*, 47.
(205) Moreno, E. C.; Varughese, K. J. *J. Cryst. Growth* **1981**, *53*, 20.
(206) Arends, J.; Christoffersen, J.; Christoffersen, M. R.; Eckert, H.; Fowler, B. O.; Heughebaert, J. C.; Nancollas, G. H.; Yesinowski, J. P.; Zawacki, S. J. *J. Cryst. Growth* **1987**, *84*, 515.
(207) Christoffersen, M. R.; Christoffersen, J. *J. Cryst. Growth* **1992**, *121*, 608.
(208) Christoffersen, M. R.; Christoffersen, J. *J. Cryst. Growth* **1992**, *121*, 617.
(209) Zawacki, S. J.; Koutsoukos, P. B.; Salimi, M. H.; Nancollas, G. H. In *Geochemical Processes at Mineral Surfaces*; Davis, J. A., Hayes, K. F., Eds.; American Chemical Society Symposium Series, Vol. 323; 1986; p 650.
(210) Kokubo, T.; Kushitani, H.; Sakka, S.; Kitsugi, T.; Yamamuro, T. *J. Biomed. Mater. Res.* **1990**, *24*, 721.
(211) Markov, I. V. *Crystal Growth for Beginners: Fundamentals of Nucleation, Crystal Growth and Epitaxy*; World Scientific Publishing Co.: Singapore, 1995.
(212) Ito, A.; Nakamura, S.; Aoki, H.; Akao, M.; Teraoka, K.; Tsutsumi, S.; Onuma, K.; Tateishi, T. *J. Cryst. Growth* **1996**, *163*, 311.
(213) Banfield, J. L.; Welch, S. A.; Zhang, H.; Ebert, T. T.; Penn, R. L. *Science* **2000**, *289*, 751.
(214) Oyane, A.; Onuma, K.; Kokubo, T.; Ito, A. *J. Phys. Chem. B* **1999**, *103*, 8230.
(215) Navrotsky, A. *Proc. Natl. Acad. Sci.* **2004**, *101*, 12096.
(216) Tomson, M. B.; Nancollas, G. H. *Science* **1978**, *200*, 1059.
(217) Zhang, J. W.; Nancollas, G. H. *Rev. Mineral.* **1990**, *23*, 365.
(218) Zhang, J. W.; Nancollas, G. H. *J. Cryst. Growth* **1992**, *125*, 251.
(219) Wu, W. J.; Nancollas, G. H. *Adv. Colloid Interface Sci.* **1999**, *79*, 229.
(220) Heughebaert, J. C.; Nancollas, G. H. *J. Phys. Chem.* **1984**, *88*, 2478.
(221) Heughebaert, J. C.; DeRooij, J. F.; Nancollas, G. H. *J. Cryst. Growth* **1987**, *80*, 450.
(222) Newesley, H. *Adv. Oral Biol.* **1970**, *4*, 11.
(223) Hartman, P.; Perdok, W. G. *Acta Crystallogr.* **1955**, *8*, 49.
(224) Hartman, P.; Perdok, W. G. *Acta Crystallogr.* **1955**, *8*, 521.
(225) Hartman, P. In *Crystal Growth: An Introduction*; Hartman, P., Ed.; North Holland: Amsterdam, 1973; p 367.
(226) Driessens, F. C.; Terpstra, M. R. A.; Bennema, P.; Woltgens, J. H. M.; Verbeeck, R. M. H. *Z. Naturforsch.* **1987**, *42c*, 916.
(227) DeRooij, J. F.; Heughebaert, J. C.; Nancollas, G. H. *J. Colloid Interface Sci.* **1984**, *100*, 350.
(228) Ebrahimpour, A.; Zhang, J. W.; Nancollas, G. H. *J. Cryst. Growth* **1991**, *113*, 83.
(229) Zawacki, S. J.; Heughebaert, J. C.; Nancollas, G. H. *J. Colloid Interface Sci.* **1990**, *135*, 33.
(230) Zhang, J. W.; Nancollas, G. H. *J. Colloids Interface Sci.* **1998**, *200*, 131.
(231) Fox, J. L.; Dave, S. C.; Higuchi, W. I. *J. Colloid Interface Sci.* **1989**, *130*, 236.
(232) Nielsen, A. E. *Croat. Chem. Acta* **1980**, *53*, 255.
(233) Stubicar, N.; Scrbak, M.; Stubicar, M. *J. Cryst. Growth* **1990**, *100*, 261.
(234) Verbeeck, R. M.; Devenyns, J. A. H. *J. Cryst. Growth* **1990**, *102*, 647.
(235) Burke, E. M.; Nancollas, G. H. *Colloids Surf.* **1999**, *150*, 151.
(236) Liu, Y.; Nancollas, G. H. *J. Cryst. Growth* **1996**, *165*, 116.
(237) Chernov, A. A.; Petrova, E. V.; Rashkovich, L. N. *J. Cryst. Growth* **2006**, *289*, 245.
(238) Chernov, A. A. *J. Mater. Sci. Mater. Electron.* **2001**, *12*, 437.
(239) Wu, W. J.; Nancollas, G. H. *J. Colloids Interface Sci.* **1996**, *182*, 365.

(240) Koutsopoulos, S.; Paschalaskis, P. C.; Dalas, E. *Langmuir* **1994**, *10*, 2423.

(241) Koutsoukos, P. G.; Nancollas, G. H. *Colloids Surf.* **1987**, *28*, 95.

(242) van Oss, C. J.; Giese, R. F.; Li, Z.; Murphy, K.; Norris, J.; Chaudhury, M. K.; Good, R. J. *J. Adhesion Sci. Technol.* **1992**, *6*, 413.

(243) Washburn, E. W. *Phys. Rev.* **1921**, *17*, 273.

(244) Ku, C. A.; Henry, J. D.; Siriwardane, R.; Roberts, L. *J. Colloid Interface Sci.* **1985**, *106*, 377.

(245) van Oss, C. J. *Interfacial Forces in Aqueous Media*; Marcel Dekker: New York, 1994; p 1.

(246) Nancollas, G. H.; Wu, W. J. *Dispersion Sci. Technol.* **1998**, *19*, 723.

(247) van Oss, C. J.; Chaudhury, M. K.; Good, R. J. *Chem. Rev.* **1988**, *88*, 927.

(248) Liu, Y.; Nancollas, G. H. *J. Phys. Chem. B* **1997**, *101*, 3464.

(249) Wu, W. J.; Nancollas, G. H. *Pure Appl. Chem.* **1998**, *70*, 1867.

(250) Nancollas, G. H.; Wu, W. J. *J. Cryst. Growth* **2000**, *211*, 137.

(251) van Oss, C. J.; Giese, R. F. *Clays Miner.* **1995**, *43*, 474.

(252) Liu, Y.; Wu, W.; Sethuraman, G.; Nancollas, G. H. *J. Cryst. Growth* **1997**, *174*, 386.

(253) Liu, Y.; Sethuraman, G.; Wu, W.; Nancollas, G. H.; Grynpas, M. *J. Colloids Interface Sci.* **1997**, *186*, 102.

(254) Hina, A.; Nancollas, G. H.; Grynpas, M. *J. Cryst. Growth* **2001**, *223*, 213.

(255) Blumenthal, N. C.; Betts, F.; Posner, A. S. *Mater. Res. Bull.* **1975**, *10*, 1055.

(256) Posner, A. S.; Betts, F.; Blumenthal, N. C. *Calcif. Tissue Res.* **1977**, *22* (Suppl.), 208.

(257) Williams, G.; Sallis, J. D. *Biochem. J.* **1979**, *184*, 181.

(258) Williams, G.; Sallis, J. D. *Calcif. Tissue Int.* **1982**, *34*, 169.

(259) Fuierer, T. A.; LoRe, M.; Puckett, S. A.; Nancollas, G. H. *Langmuir* **1994**, *10*, 4721.

(260) Grynpas, M. D.; Cheng, P. T. *Bone Miner.* **1988**, *5*, 1.

(261) Grynpas, M. D. *J. Bone Miner. Res.* **1990**, *5*, S169.

(262) Moreno, E. C.; Kresak, M.; Zahradnik, R. T. *Caries Res.* **1976**, *11*, 142.

(263) Featherstone, J. D. B.; Nelson, D. G. A. *Aust. J. Chem.* **1980**, *33*, 2363.

(264) Featherstone, J. D. B.; Mayer, I.; Driessens, F. M. C.; Verbeeck, R. M. H.; Heijligers, H. J. M. *Calcif. Tissue Int.* **1983**, *35*, 169.

(265) Cheng, P. T. In *Urolithiasis*; Walker, V. R., Sutton, R. A. L., Cameron, E. C. B., Pak, C. Y. C., Robertson, W. G., Eds.; Plenum Press: New York, 1989; p 225.

(266) Sharma, V. K.; Johnsson, M.; Sallis, J. D.; Nancollas, G. H. *Langmuir* **1992**, *8*, 676.

(267) Bovey, F. A.; Hood, F. P.; Anderson, E. W.; Kornegay, R. L. *J. Chem. Phys.* **1964**, *41*, 2041.

(268) Burke, E. M.; Guo, Y.; Colon, L.; Rahima, M.; Veis, A.; Nancolas, G. H. *Colloids Surf., B* **2000**, *17*, 49.

(269) Tsortos, A.; Nancollas, G. H. *J. Dent. Res.* **1993**, *72*, 276.

(270) Tsortos, A.; Nancollas, G. H. *J. Colloids Interface Sci.* **1999**, *209*, 109.

(271) Nancollas, G. H.; Tsortos, A.; Zieba, A. *Scanning Microsc.* **1996**, *10*, 499.

(272) Bigi, A.; Boanini, E.; Walsh, D.; Mann, S. *Angew. Chem., Int. Ed.* **2002**, *41*, 2163.

(273) Bigi, A.; Bracci, B.; Panzavolta, S.; Iliescu, M.; Plouet-Richard, M.; Werckmann, J.; Cam, D. *Cryst. Growth Des.* **2004**, *4*, 141.

(274) Zieba, A.; Sethuraman, G.; Perez, F.; Nancollas, G. H.; Cameron, D. *Langmuir* **1996**, *12*, 2853.

(275) Onuma, K.; Kanzaki, N.; Kobayashi, N. *Macromol. Biosci.* **2004**, *4*, 39.

(276) Dalas, E.; Barlos, K.; Gatos, D.; Manis, P. *Cryst. Growth Des.* **2007**, *7*, 132.

(277) Mangood, A.; Malkaj, P.; Dalas, E. *J. Cryst. Growth* **2006**, *290*, 565.

(278) Murphy, M. B.; Hartgerink, J. D.; Goepferich, A.; Mikos, A. G. *Biomacromolecules* **2007**, *8*, 2237.

(279) Zhai, Y.; Cui, F. Z. *J. Cryst. Growth* **2006**, *291*, 202.

(280) Ball, V.; Planeix, J. M.; Felix, O.; Hemmerle, J.; Schaaf, P.; Hosseini, M. W.; Voegel, J. C. *Cryst. Growth Des.* **2002**, *2*, 489.

(281) Zhang, H. G.; Zhu, Q. S.; Wang, Y. *Chem. Mater.* **2005**, *17*, 5824.

(282) Tlatlik, H.; Simon, P.; Kawska, A.; Zahn, D.; Kniep, R. *Angew. Chem., Int. Ed.* **2006**, *45*, 1905.

(283) Simon, P.; Zahn, D.; Lichte, H.; Kniep, R. *Angew. Chem., Int. Ed.* **2006**, *45*, 1911.

(284) Prymak, O.; Sokolova, V.; Peitsch, T.; Epple, M. *Cryst. Growth Des.* **2006**, *6*, 498.

(285) Flade, K.; Lau, C.; Mertig, M.; Pompe, W. *Chem. Mater.* **2001**, *13*, 3596.

(286) Dowd, T. L.; Rosen, J. F.; Li, L.; Gundberg, C. M. *Biochemistry* **2003**, *42*, 7769.

(287) Campbell, A. A.; Ebrahimpour, A.; Perez, L.; Smesko, S. A.; Nancollas, G. H. *Calcif. Tissue Int.* **1989**, *45*, 122.

(288) Schwartz, S. S.; Hay, D. I.; Schluckebier, S. K. *Calcif. Tissue Int.* **1992**, *50*, 511.

(289) Raj, P. A.; Johnsson, M.; Levine, M. J.; Nancollas, G. H. *J. Biol. Chem.* **1992**, *267*, 5968.

(290) Johnsson, M.; Richardson, C. F.; Bergey, D. J.; Levine, M. J.; Nancollas, G. H. *Arch. Oral Biol.* **1991**, *36*, 631.

(291) Chin, K. O. A.; Johnsson, M.; Bergey, E. J.; Levine, M. J.; Nancollas, G. H. *Colloids Surf.* **1993**, *78*, 229.

(292) Stayton, P. S.; Drobny, G. P.; Shaw, W. J.; Long, J. R.; Gilbert, M. *Crit. Rev. Oral Biol. Med.* **2003**, *14*, 370.

(293) Wikiel, K.; Burke, E. M.; Perich, J. W.; Reynolds, E. C.; Nancollas, G. H. *Arch. Oral Biol.* **1994**, *39*, 715.

(294) Hunter, G. K.; Kyle, C. L.; Goldberg, H. A. *Biochem. J.* **1994**, *300*, 723.

(295) Romberg, R. W.; Werness, P. G.; Riggs, B. L.; Mann, K. G. *Biochemistry* **1986**, *25*, 1176.

(296) Heiss, A.; DuChesne, A.; Denecke, B.; Grotzinger, J.; Yamamoto, K.; Renne, T.; Jahnen-Dechent, W. *J. Biol. Chem.* **2003**, *278*, 13333.

(297) Kandori, K.; Mukai, M.; Yasukawa, A.; Ishikawa, T. *Langmuir* **2000**, *16*, 2301.

(298) Kandori, K.; Murata, K.; Ishikawa, T. *Langmuir* **2007**, *23*, 2064.

(299) Barralet, J. E.; Tremayne, M.; Lilley, K. J.; Gbureck, U. *Chem. Mater.* **2005**, *17*, 1313.

(300) Nancollas, G. H.; Tang, R. K.; Phipps, R. J.; Henneman, Z.; Gulde, S.; Wu, W. J.; Mangood, A.; Russell, R. G.; Ebetino, F. H. *Bone* **2006**, *38*, 617.

(301) Ngakam, P. A.; Lavalle, P.; Voegel, J. C.; Szyk, L.; Decher, G.; Schaaf, P.; Cuisinier, F. J. G. *J. Am. Chem. Soc.* **2000**, *122*, 8998.

(302) Cappellen, P.; Berner, R. A. *Geochem. Cosmochem. Acta* **1991**, *55*, 1219.

(303) Dallas, E.; Kallitsis, J. K.; Koutsoukos, P. G. *Langmuir* **1991**, *7*, 1822.

(304) Dallas, E.; Ioannou, P. V.; Koutsoukos, P. G. *Langmuir* **1989**, *5*, 157.

(305) Saito, T.; Yamauchi, M.; Crenshaw, M. A. *J. Bone Miner. Res.* **1998**, *13*, 265.

(306) Elhadj, S.; De Yoreo, J. J.; Hoyer, J. R.; Dove, P. M. *Proc. Natl. Acad. Sci.* **2006**, *103*, 19237.

(307) Land, T. A.; De Yoreo, J. J. *J. Cryst. Growth* **1999**, *208*, 623.

(308) De Yoreo, J. J.; Orme, C. A.; Land, T. A. In *Advances in crystal growth research*; Sato, K., Nakajima, K., Furukawa, Y., Eds.; Elsevier: Amsterdam, 2001; p 361.

(309) Tang, R. K.; Orme, C. A.; Nancollas, G. H. *J. Phys. Chem. B* **2003**, *107*, 10653.

(310) Qiu, S. R.; Wierzbicki, A.; Orme, C. A.; Cody, A. M.; Hoyer, J. R.; Nancollas, G. H.; Zepeda, S.; De Yoreo, J. J. *Proc. Natl. Acad. Sci. U.S.A.* **2004**, *101*, 1811.

(311) De Yoreo, J. J.; Qiu, S. R.; Hoyer, J. R. *Am. J. Physiol.* **2006**, *291*, F1123.

(312) Orme, C. A.; Noy, A.; Wierzbicki, A.; McBride, M. Y.; Grantham, M.; Dove, P. M.; DeYoreo, J. J. *Nature* **2001**, *411*, 775.

(313) De Yoreo, J. J.; Dove, P. M. *Science* **2004**, *306*, 1301.

(314) Land, T. A.; Martin, T. L.; Potapenko, S.; Palmore, G. T.; De Yoreo, J. J. *Nature* **1999**, *399*, 442.

(315) Davis, K. J.; Dove, P. M.; De Yoreo, J. J. *Science* **2000**, *290*, 1134.

(316) Elhadj, S.; Salter, A.; Wierzbicki, A.; De Yoreo, J. J.; Han, N.; Dove, P. M. *Cryst. Growth Des.* **2006**, *6*, 197.

(317) Malkin, A. J.; Chernov, A. A. *J. Cryst. Growth* **1989**, *97*, 765.

(318) George, A.; Sabsay, B.; Simonian, P. A.; Veis, A. *J. Biol. Chem.* **1993**, *268*, 12624.

(319) Hunter, G. K.; Haushka, P. V.; Poole, A. R.; Rosenburg, L. C.; Goldberg, H. A. *Biochem. J.* **1996**, *317*, 59.

(320) Begue-Kirn, C.; Ruch, J. V.; Ridall, A. L.; Butler, W. T. *Eur. J. Oral Sci.* **1998**, *106*, 254.

(321) Bronckers, A. L.; Farach-Carson, M. C.; Van Waveren, E.; Butler, W. T. *J. Bone Miner. Res.* **1994**, *9*, 833.

(322) Koutsopoulos, S.; Dalas, E. *Langmuir* **2000**, *16*, 6739.

(323) Koutsopoulos, S.; Dalas, E. *Langmuir* **2001**, *17*, 1074.

(324) Murphy, M. B.; Hartgerink, J. D.; Goepferich, A.; Mikos, A. G. *Biomacromolecules* **2007**, *8*, 2237.

(325) Ball, V.; Michel, M.; Boulmedais, F.; Hemmerle, J.; Haikel, Y.; Schaaf, P.; Voegel, J. C. *Cryst. Growth Des.* **2006**, *6*, 327.

(326) Long, J. R.; Dindot, J. L.; Zebroski, H.; Kiihne, S.; Clark, R. H.; Campbell, A. A.; Stayton, P. S.; Drobny, G. P. *Proc. Natl. Acad. Sci. U.S.A.* **1998**, *95*, 12083.

(327) Shaw, W. J.; Long, J. R.; Dindot, J. L.; Campbell, A. A.; Stayton, P. S.; Drobny, G. P. *J. Am. Chem. Soc.* **2000**, *122*, 1709.

(328) Shaw, W. J.; Long, J. R.; Stayton, P. S.; Drobny, G. P. *J. Am. Chem. Soc.* **2000**, *122*, 7118.

(329) Hauschka, P. V.; Carr, S. A. *Biochemistry* **1982**, *21*, 2538.

(330) DeOliviera, D. B.; Laursen, R. A. *J. Am. Chem. Soc.* **1997**, *119*, 10627.

(331) Gibson, J. M.; Raghunathan, V.; Popham, J. M.; Stayton, P. S.; Drobny, G. P. *J. Am. Chem. Soc.* **2005**, *127*, 9350.

(332) Raghunathan, V.; Gibson, J. M.; Goobes, G.; Popham, J. M.; Louie, E. A.; Stayton, P. S.; Drobny, G. P. *J. Phys. Chem. B* **2006**, *110*, 9324.
(333) Gibson, J. M.; Popham, J. M.; Raghunathan, V.; Stayton, P. S.; Drobny, G. P. *J. Am. Chem. Soc.* **2006**, *128*, 5364.
(334) Goobes, G.; Goobes, R.; Schueler-Furman, O.; Baker, D.; Stayton, P. S.; Drobny, G. P. *Proc. Natl. Aacd. Sci.* **2006**, *103*, 16083.
(335) Goobes, R.; Goobes, G.; Campbell, C. T.; Stayton, P. S. *Biochemistry* **2006**, *45*, 5576.
(336) Goobes, R.; Goobes, G.; Shaw, W. J.; Drobny, G. P.; Campbell, C. T.; Stayton, P. S. *Biochemistry* **2007**, *46*, 4725.
(337) Markrodimitris, K.; Masica, D. L.; Kim, E. T.; Gray, J. J. *J. Am. Chem. Soc.* **2007**, *129*, 13713.
(338) Zhou, S. B.; Zheng, X. T.; Yu, X. J.; Wang, J. X.; Weng, J.; Li, X. H.; Feng, B.; Yin, M. *Chem. Mater.* **2007**, *19*, 247.
(339) Jaeger, C.; Groom, N. S.; Bowe, E. A.; Horner, A. M.; Davies, E.; Murray, R. C.; Duer, M. J. *Chem. Mater.* **2005**, *17*, 3059.
(340) Misra, D. N. *Langmuir* **1991**, *7*, 2422.
(341) Pan, H. H.; Tao, J. H.; Xu, X. R.; Tang, R. K. *Langmuir* **2007**, *23*, 8972.
(342) Filgueiras, M. R. T.; Mkhonto, D.; de Leeuw, N. H. *J. Cryst. Growth* **2006**, *294*, 60.
(343) Mkhonto, D.; Ngoepe, P. E.; Cooper, T. G.; de Leeuw, N. H. *Phys. Chem. Miner.* **2006**, *33*, 314.
(344) Capriotti, L. A.; Beebe, T. P.; Schneider, J. P. *J. Am. Chem. Soc.* **2007**, *129*, 5281.
(345) Elangovan, S.; Margolis, H. C.; Oppenheim, F. G.; Beniash, E. *Langmuir* **2007**, *23*, 11200.
(346) Hoang, Q. Q.; Sicheri, F.; Howard, A. J.; Yang, D. S. C. *Nature* **2003**, *425*, 977.
(347) Liu, X. Y.; Boek, E. S.; Briels, W. J.; Bennema, P. *Nature* **1995**, *374*, 342.
(348) Burton, W. K.; Cabrera, N.; Frank, F. C. *Philos. Trans. R. Soc.* **1951**, *A243*, 299.
(349) Bennema, P. *J. Cryst. Growth* **1984**, *69*, 182.
(350) Pina, C. M.; Becker, U.; Risthaus, P.; Bosbach, D.; Putnis, A. *Nature* **1998**, *395*, 483.
(351) Hannon, J. B.; Shenoy, V. B.; Schwarz, K. W. *Science* **2006**, *313*, 1266.
(352) Voorhees, P. W. *Science* **2006**, *313*, 1247.
(353) Onuma, K.; Ito, A.; Tateishi, T.; Kameyama, T. *J. Cryst. Growth* **1995**, *154*, 118.
(354) Onuma, K.; Ito, A.; Tateishi, T. *J. Cryst. Growth* **1996**, *167*, 773.
(355) Chernov, A. A.; Rashkovich, L. N. *J. Cryst. Growth* **1987**, *84*, 389.
(356) Maiwa, K.; Tsukamoto, K.; Sunagawa, I. *J. Cryst. Growth* **1990**, *102*, 43.
(357) Kuznetsov, Y. G.; Malkin, A. J.; Glantz, W.; McPherson, A. *J. Cryst. Growth* **1996**, *168*, 63.
(358) Land, T. A.; Malkin, A. J.; Kuznetsov, Y. G.; McPherson, A.; DeYoreo, J. J. *Phys. Rev. Lett.* **1995**, *75*, 2774.
(359) Malkin, A. J.; Kuznetsov, Y. G.; Glantz, W.; McPherson, A. *J. Phys. Chem.* **1996**, *100*, 11736.
(360) Kanzaki, N.; Onuma, K.; Ito, A.; Teraoka, K.; Tateishi, T.; Tsutsumi, S. *J. Phys. Chem. B* **1998**, *102*, 6471.
(361) Onuma, K.; Kanzaki, N.; Ito, A.; Tateishi, T. *J. Phys. Chem. B* **1998**, *102*, 7833.
(362) Durbin, S. D.; Feher, G. *J. Cryst. Growth* **1986**, *76*, 583.
(363) Malkin, A. I.; Chernov, A. A.; Alexeev, I. V. *J. Cryst. Growth* **1989**, *97*, 765.
(364) Davis, K. J.; Dove, P. M.; Wasylenki, L. E.; De Yoreo, J. J. *Am. Mineral.* **2004**, *89*, 714.
(365) Wang, L. J.; Qiu, S. R.; Zachowicz, W. Z.; Guan, X.; De Yoreo, J. J.; Nancollas, G. H.; Hoyer, J. R. *Langmuir* **2006**, *22*, 7279.
(366) Cabrera, N.; Vermilyea, D. A. In *Growth and Perfection of Crystals; Proceedings*; Doremus, R. H., Roberts, B. W., Turnbull, D., Eds.; Wiley: New York, 1958; p 393.
(367) Weaver, M.; Qiu, S. R.; Hoyer, J. R.; Casey, W. H.; Nancollas, G. H.; De Yoreo, J. J. *ChemPhysChem* **2006**, *7*, 2081.
(368) Wang, L. J.; De Yoreo, J. J.; Guan, X.; Qiu, S. R.; Hoyer, J. R.; Nancollas, G. H. *Cryst. Growth Des.* **2006**, *6*, 1769.

(369) Potapenko, S. *J. Cryst. Growth* **1993**, *133*, 147.
(370) Thomas, T. N.; Land, T. A.; DeYoreo, J. J.; Casey, W. H. *Langmuir* **2004**, *20*, 7643.
(371) Qiu, S. R.; Wierzbicki, A.; Salter, E. A.; Zepeda, S.; Orme, C. A.; Hoyer, J. R.; Nancollas, G. H.; Cody, A. M.; De Yoreo, J. J. *J. Am. Chem. Soc.* **2005**, *127*, 9036.
(372) Wang, L. J.; Zhang, W.; Qiu, S. R.; Zachowicz, W. J.; Guan, X.; Tang, R.; Hoyer, J. R.; De Yoreo, J. J.; Nancollas, G. H. *J. Cryst. Growth* **2006**, *291*, 160.
(373) Tang, R. K.; Darragh, M.; Orme, C. A.; Guan, X.; Hoyer, J. R.; Nancollas, G. H. *Angew. Chew. Int. Ed.* **2005**, *44*, 3698.
(374) Lasaga, A. C.; Lüttge, A. *J. Phys. Chem. B* **2005**, *109*, 1635.
(375) Lasaga, A. C.; Lüttge, A. *Science* **2001**, *291*, 2400.
(376) Tang, R. K.; Nancollas, G. H.; Orme, C. A. *J. Am. Chem. Soc.* **2001**, *123*, 5437.
(377) Tang, R. K.; Orme, C. A.; Nancollas, G. H. *ChemPhysChem* **2004**, *5*, 688.
(378) Lüttge, A. *J. Electron Spectrosc. Relat. Phenom.* **2006**, *150*, 248.
(379) Lasaga, A. C.; Lüttge, A. *Eur. J. Miner.* **2003**, *15*, 603.
(380) Tang, R. K.; Wang, L. J.; Orme, C. A.; Bonstein, T.; Bush, P. J.; Nancollas, G. H. *Angew. Chem., Int. Ed.* **2004**, *43*, 2697.
(381) Tang, R. K.; Wang, L. J.; Nancollas, G. H. *J. Mater. Chem.* **2004**, *14*, 2341.
(382) Tang, R. K.; Wu, W.; Haas, M.; Nancollas, G. H. *Langmuir* **2001**, *17*, 3480.
(383) Tang, R. K.; Henneman, Z. J.; Nancollas, G. H. *J. Cryst. Growth* **2003**, *249*, 614.
(384) Peytcheva, A.; Antonietti, M. *Angew. Chem., Int. Ed.* **2001**, *40*, 3380.
(385) Wang, L. J.; Tang, R. K.; Bonstein, T.; Orme, C. A.; Bush, P. J.; Nancollas, G. H. *J. Phys. Chem. B* **2005**, *109*, 999.
(386) Wang, L. J.; Tang, R. K.; Bonstein, T.; Bush, P. J.; Nancollas, G. H. *J. Dent. Res.* **2006**, *85*, 359.
(387) Anderson, P.; Elliott, J. C.; Bose, U.; Jones, S. J. *Arch. Oral Biol.* **1996**, *41*, 281.
(388) Dowker, S. E. P.; Elliott, J. C.; Davis, G. R.; Wassif, H. S. *Caries Res.* **2003**, *37*, 237.
(389) Gerard, D. E.; Fried, D.; Featherstone, J. D.; Nancollas, G. N. *Caries Res.* **2005**, *39*, 387.
(390) Wang, L. J.; Nancollas, G. H.; Henneman, Z. J.; Klein, E.; Weiner, S. *Biointerphases* **2006**, *1*, 106.
(391) Weiner, S.; Wagner, H. D. *Annu. Rev. Mater. Sci.* **1998**, *28*, 271.
(392) Landis, W. J. *Bone* **1995**, *16*, 533.
(393) Gao, H.; Ji, B.; Ingomar, L. J.; Arz, E.; Fratzl, P. *Proc. Natl. Acad. Sci. U.S.A.* **2003**, *100*, 5597.
(394) Bolze, J.; Peng, B.; Dingenouts, N.; Panine, P.; Narayanan, T.; Ballauff, M. *Langmuir* **2002**, *18*, 8364.
(395) Pontoni, D.; Bolze, J.; Dingenouts, N.; Narayanan, T.; Ballauff, M. *J. Phys. Chem. B* **2003**, *107*, 5123.
(396) Bolze, J.; Pontoni, D.; Ballauff, M.; Narayanan, T.; Cölfen, H. *J. Colloid Interface Sci.* **2004**, *277*, 84.
(397) DiMasi, E.; Kwak, S. Y.; Amos, F. F.; Olszta, M. J.; Lush, D.; Gower, L. B. *Phys. Rev. Lett.* **2006**, *97*, 045503.
(398) Cölfen, H.; Antonietti, M. *Angew. Chem., Int. Ed.* **2005**, *44*, 5576.
(399) Cölfen, H.; Mann, S. *Angew. Chem., Int. Ed.* **2003**, *42*, 2350.
(400) Margolis, H. C.; Beniash, E.; Fowler, C. E. *J. Dent. Res.* **2006**, *85*, 775.
(401) Dunin-Borkowski, R. E.; McCartney, M. R.; Frankel, R. B.; Bazylinski, D. A.; Pósfai, M.; Buseck, P. R. *Science* **1998**, *282*, 1868.
(402) Alivisatos, A. P. *Science* **2000**, *289*, 736.
(403) Yeadon, M.; Ghaly, M.; Yang, J. C.; Averback, R. S.; Gibson, J. M. *Appl. Phys. Lett.* **1998**, *73*, 3208.
(404) Penn, R. L.; Banfield, J. F. *Science* **1998**, *281*, 969.
(405) Zhu, H. L.; Averback, R. S. *Philos. Mag. Lett.* **1996**, *73*, 27.
(406) McHale, J. M.; Auroux, A.; Perrotta, A. J.; Navrotsky, A. *Science* **1997**, *277*, 788.
(407) Zhang, H.; Banfield, J. F. *J. Mater. Chem.* **1998**, *8*, 2073.

CR0782574